One-step Synthesis of Submicron-sized FeNi and SiO_2-coated FeNi Particles via Spray Pyrolysis Method and Their Magnetic Characteristics

(噴霧熱分解法によるサブミクロンサイズの FeNi および SiO_2 コート FeNi 粒子のワンステップ合成とその磁気特性）

A Thesis submitted to
The Chemical Engineering Program
Graduate School of Advanced Science and Engineering
Hiroshima University

Presented by

EKA LUTFI SEPTIANI

In Partial Fulfillment of the Requirements for the Degree of
Doctor of Engineering

Hiroshima University
July 2023

Approved by
Professor Takashi Ogi
Adviser

Abstract

Advanced soft-magnetic particles are of paramount importance for the development of power converter components, particularly powder core inductors. These components play a crucial role in achieving sustainable development goals in the context of digital devices, electric machines, and renewable power generators. Incorporating advanced soft-magnetic particles as secondary materials offers significant improvements in the magnetic characteristics of powder core inductors, providing advantages for machine design. This dissertation presents a comprehensive investigation into the synthesis of submicron-sized spherical iron nickel (FeNi) and silica-coated iron nickel (FeNi@SiO_2) particles via the aerosol process, with the aim of utilizing them as secondary materials in powder core inductors. The research encompasses the exploration of various experimental parameters and equipment designs to evaluate the effectiveness of FeNi@SiO_2 particles for powder core inductors. Additionally, computational fluid dynamics (CFD) simulations are employed to gain a better understanding of the plausible mechanisms involved in particle formation. Each chapter of this dissertation is briefly described below.

Chapter 1 over-viewed the powder core inductor, fundamental magnetic characterization, recent studies in improving the magnetic characteristic of a powder core inductor, strategies in synthesizing FeNi and FeNi@SiO_2 particles, and a numerical approach based on computational fluid dynamic (CFD). This summary and problem statements lead to the motivation of the research covered within the scope of this dissertation.

Chapter 2 focuses on the synthesis of FeNi particles through spray pyrolysis, specifically addressing the challenge of using alternative reduction agents due to safety concerns associated with using 100% H_2 gas. The effects of different reduction agents, such as ethanol, ethylene glycol, and formic acid, and their concentrations in the precursor solution are investigated. Ethanol and ethylene glycol, at a concentration of 25 vol%, successfully yield spherical and submicron-sized FeNi particles with dense and hollow structures, respectively. Conversely, the use of formic acid results in the formation of segregated particles comprising FeNi and FeO phases. To explain the plausible mechanisms of FeNi particle synthesis using different reduction agents, CFD simulations are performed to examine temperature profiles and the formation of H_2 and H_2O gases in the spray pyrolysis reactor. It is concluded that the FeNi particle's formation occurred in two stages which were droplet evaporation and chemical reaction as well as reduction.

The concentration of H_2 and H_2O gases derived from different reduction agents influences the resulting structure of FeNi particles, with ethanol emerging as the preferred reduction agent.

The use of ethanol in synthesizing FeNi particles presents a challenge in forming some hollow particles, which can limit the performance of inductors due to their low density. **Chapter 3** discusses strategies to control the structure and density of FeNi particles, transforming them from hollow (low density) to dense (high density), by manipulating reactor temperature from 1200 to 1400 ^{o}C and carrier gas flow rate from 5 to 1.3 L/min. It is pointed that the temperatures above 1200 ^{o}C can promote the alteration of structures from hollow to dense, but it leads to the formation of undesired carbon nanoparticles. Therefore, the effect of carrier gas flow rates is investigated at 1200 ^{o}C. Decreasing the carrier gas flow rate prolongs particle residence time in the reactor, facilitating densification and reducing the formation of hollow particles. Consequently, the density of FeNi particles is significantly improved. Furthermore, magnetic characterization reveals that the synthesized FeNi particles exhibit the highest saturated magnetization value among other synthesis methods, which reach the theoretical value. In terms of inductor applications, FeNi particles with denser structures and higher densities offer improved DC bias characteristic of the inductor.

Chapter 4 is focused to the synthesis of FeNi@SiO_2 particles in a one-step process via spray pyrolysis, aiming a powder core with high DC bias characteristic and low energy loss. The strategy involves introducing the silica source to the intermediate product of FeNi aerosol. A preheater system is implemented to transform FeNi precursor droplets into their intermediate product. Hexamethyldisiloxane (HMDSO) is used as the silica source, and three types of developed connectors (T-shaped, Swirler-3, and Swirler-6) are compared. Based on the structure and morphology of particles obtained with different connector types, Swirler-6 is identified as the optimal choice, offering the highest coating ratio and the lowest generation of undesired nanoparticles. A CFD simulation is performed to assess the mixing performance between FeNi droplets and HMDSO vapor in the reactor, providing insight into the favorable distribution of FeNi droplets and HMDSO vapor until the end of the reactor, which promotes heterogeneous nucleation. The synthesized FeNi@SiO_2 particles are then compared with the synthesized FeNi particles in terms of inductor performance. The FeNi@SiO_2 particles not only enhance the DC bias characteristic (high saturation current) of the inductor but also reduce energy losses (core loss) between interparticles within the inductor.

Chapter 5 contains the summary of all chapters and directions for the future work.

Table of Content

List of Tables

List of Figures

Chapter 1
Introduction

Energy plays a critical role in driving long-term economic development and reducing poverty, while also ensuring sustainability. However, the ever-increasing energy demand resulting from population growth, especially in areas such as transportation, electricity, and industrialization, poses a significant global challenge to sustainability due to the gas pollution emitted from the utilization of fossil fuels. Disturbingly, reports indicate that carbon dioxide emissions, a major contributor to gas pollution, have soared over the past 25 years, leading to an estimated 4.2 million premature deaths [1,2]. To address this pressing issue, significant emphasis is being placed on advancing energy utilization through the development of digital devices, electric vehicles, and renewable power generators. Key to achieving this objective is the ability to design devices and machines that are not only highly efficient but also compact, thus minimizing their environmental footprint. This is where passive components such as power inductors come into play, as they contribute significantly to the space and weight considerations within electric circuits [3]. In recent times, numerous researchers have dedicated their efforts to investigating various materials and component designs with the goal of creating the most efficient power inductors. These advancements are crucial for meeting the evolving needs of electronic devices and machinery, which are undergoing rapid evolution and technological progress.

1.1 Power inductor

Inductors is critical in electronic circuits by serving various functions such as voltage stabilization, current management, high-frequency signal control, and noise elimination. When designing electronic devices and machines with a focus on energy efficiency, the inclusion of a power inductor becomes essential. Typically, a power inductor consists of a magnetic core wound with a winding coil. Among the commonly used magnetic cores for power inductors, ferrite cores and powder cores are prevalent. Ferrite core is a core that is made by ceramic structure of mixed iron oxide (Fe_2O_3) with oxide or carbonates of one or more metals such as manganese, zinc, nickel, or magnesium. Whereas the powder core is a core that comprises of small magnetic particles such as Fe, Ni, Co, and its alloy. In recent developments, devices and machines have increasingly operated at higher frequencies, driven by the transition from 4G to 5G mobile networks and the projected advent of 6G. As a result, the size of power inductors can be effectively reduced, allowing for compact designs that support the miniaturization of electronic components.

In the application of the power inductor, the presence of an air gap within the core structure is required to store energy and to prevent the core from saturating under load [4]. For the ferrite core, a concentrated air gap is usually made in a certain space as shown in **Figure 1.1**. This air gap can improve the magnetic saturation of a ferrite core. However, the concentrated air gap produces a fringing flux which causes an energy loss, i.e. eddy current loss, significantly. Although this loss can be suppressed by edging the corner of the magnetic core or by distributing a concentrated air gap into several air gaps, this process increases the production cost [5]. On the other hand, the powder core provides a distributed air gaps owing to the distance of inter particles in the compacted powder. The distributing air gap can eliminate the fringing loss while keeping the eddy current loss at minimum. Therefore, among the power inductor types, powder core inductor is the most suitable for minimizing the devices and machines design owing to its good stability and ability in working at high frequency and saturation.

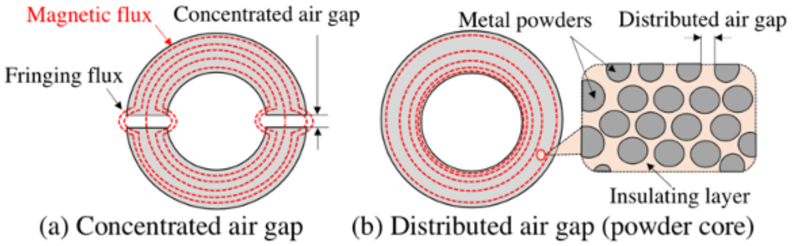

Figure 1.1. Magnetic core with concentrated (typical ferrite core) and distributed air gaps (powder core). Adapted from [4]

1.2 Powder core inductor and its magnetic characteristics

A powder core inductor is a type of inductor that uses a powdered magnetic core material instead of a solid core. This type of inductor offers a number of benefits over traditional inductors that use solid core materials. With a powdered core, the inductor can achieve a higher level of inductance in a smaller physical space, making it useful for a wide range of applications, including power electronics, telecommunications, and so forth. The powdered core material is typically made up of tiny magnetic particles which compressed and molded into the desired shape. It can be a cylindrical shape or a toroidal shape. The inductor coil is then wound around the powdered core, which can be made up of a variety of different magnetic materials, including iron, nickel, cobalt and other alloys. One advantage of using a powdered core material is that it can offer a higher saturation flux density than solid core materials, which means that it can store more energy. Additionally, the powdered core material can offer a lower core loss, which results in greater efficiency and improved performance.

1.2.1 Magnetization

Magnetization is a fundamental process in an inductor, where the generation of a magnetic field occurs due to the flow of current through its coil. When an electric current passes through the inductor's wire, a magnetic field is generated around the coil. Magnetization is a measurable quantity represented by the symbol M, which describes the overall magnetism of an object. It is measured in units of ampere per meter ($A.m^{-1}$). Magnetization signifies the concentration of magnetic dipoles within a given volume of material. Specifically, if we use the symbol n to represent the number N of tiny magnetic dipoles per unit volume of a magnetic substance, measured in reciprocal cubic meters (m^{-3}), the magnetization of the material can be calculated using the following equation:

$$M = Nm/V = n\,m \qquad (1.1)$$

When the material is exposed to a magnetic field denoted as H, the magnetization of the material is directly proportional to the magnitude of the applied magnetic field, as described by the following equation:

$$M = \chi H \qquad (1.2)$$

Where the dimensionless factor χ, also referred to as χ_m or κ, represents the absolute magnetic susceptibility of a material. It is an intrinsic property that plays a crucial role in classifying materials based on their magnetic behavior. Magnetic susceptibility determines how a material responds to a magnetic field. Materials with small and negative susceptibilities (around -10^{-5}) are known as diamagnetic materials or diamagnets. Superconductors with a susceptibility of -1 are considered perfect diamagnets. On the other hand, materials with small and positive susceptibilities ($+10^{-5} < \chi < +10^{-3}$) are called paramagnetic materials or paramagnets. There are also ferromagnetic materials or ferromagnets, which have significantly higher positive susceptibilities, usually ranging from 50 to 10^4. However, it's important to note that the magnetic susceptibility of ferromagnetic materials is not constant and is strongly influenced by the magnetic field. When a specific material is exposed to a magnetic field, denoted as H, its response as overall magnetic induction that can be expressed as follows:

$$B = \mu_0 \mu_r H = \mu_0 H(1+\chi) \qquad (1.3)$$

From Equation (1.3) The clear expression of interdependence may be observed between two dimensionless values, specifically the relative magnetic permeability (μ_r) and the magnetic susceptibility (χ) of the material [6].

The magnetic field induces magnetization within the core material of the inductor, aligning its magnetic domains in a specific direction [7], as shown in **Figure 1.2**. The magnitude of magnetization depends on the current intensity and the inductance of the inductor. As a result, the inductor stores energy in the form of a magnetic field, which can be released when the current flow is interrupted or varied. This magnetization process plays a crucial role in the functioning of inductors, allowing them to store and transfer energy efficiently within electrical circuits.

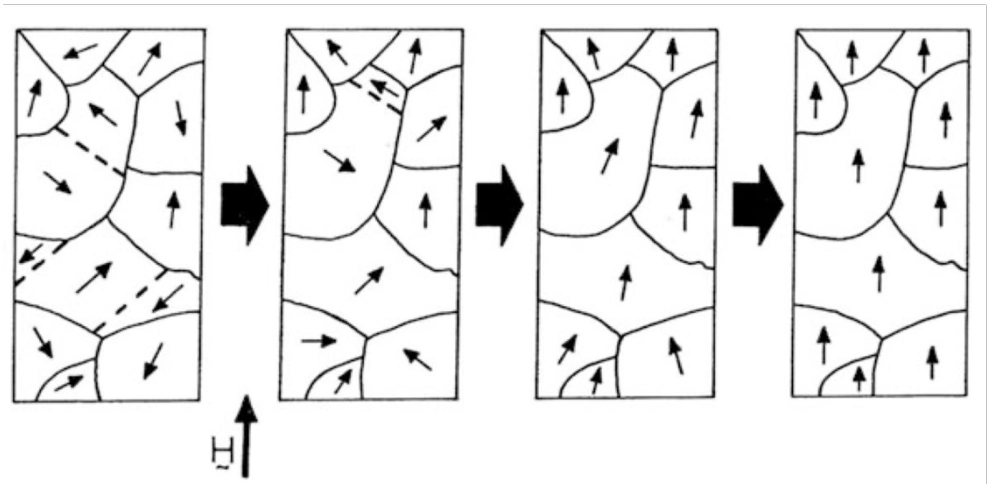

Figure 1.2. Magnetization of polycrystalline ferromagnetic material in a magnetic field, H. Solid line and dashed line represented grain boundaries and magnetic domain, respectively. Arrows indicate magnetization directions of individual crystal grains or magnetic domains. Adapted from [7]

1.2.2 Hysteresis loop

The hysteresis loop is a graphical representation that illustrates the magnetic behavior of a material, particularly its response to an alternating magnetic field. It depicts representation of the magnetic behavior of ferromagnetic materials can be observed through the relationship between magnetic induction (B) and the applied external magnetic field (H) during a magnetization cycle (**Figure 1.3**). The hysteresis loop is named so because it showcases the phenomenon of hysteresis, which refers to the material's ability to retain some magnetization even after the magnetic field has been removed. The hysteresis loop typically consists of two branches: the magnetization curve during increasing magnetic field strength (ascending branch) and the curve during decreasing field strength (descending branch). Initially, when there is no external magnetic field ($B = 0$ and $H = 0$), the magnetic induction starts from zero and gradually increases as the magnetic field is increased. During this stage, Weiss domains are formed within the material. These domains consist of areas where the spontaneous magnetization aligns with the applied magnetic field, while other magnetic domains contain Bloch walls that shift within the material. The linear slope observed in the early stage of the curve is a result of the reversible movement of Bloch walls at significantly low magnetic fields. Nevertheless, after the external magnetic field attains its maximum magnitude, referred to as H_S, the entirety of the material aligns itself into a solitary Weiss domain, leading to the attainment of the maximum net magnetic induction, commonly referred to as the saturation magnetic induction (B_S). The concept of saturation induction refers to a condition in which the magnetic dipoles present in a material become uniformly aligned with the applied magnetic field. The saturation induction value is determined exclusively by the atomic magnetic moments (m) and the atomic density (n) within the material:

$$B_s = \mu_0 \, n \, m \qquad (1.4)$$

Saturation induction is not structure sensitive and is dependent simply on the ferromagnetic atoms present in the materials.

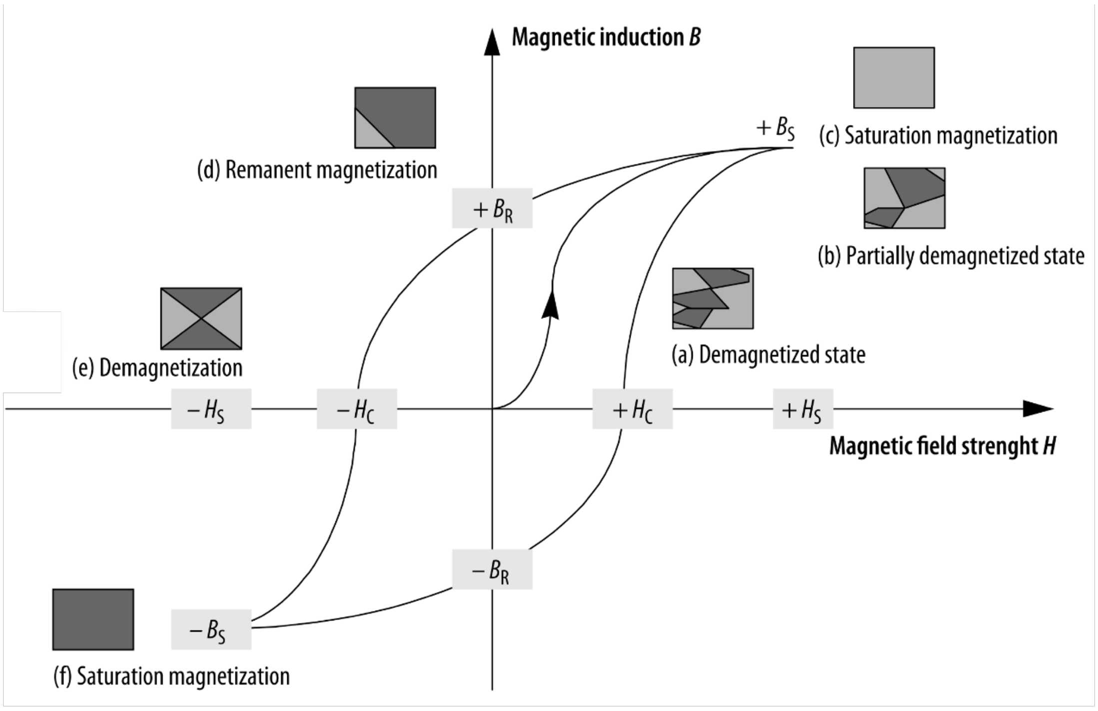

Figure 1.3. B-H Hysteresis loop. Adapted from [6]

Due to the irreversibility of the walls' motion, When the external magnetic field is decreased, the magnetic induction exhibits a curve characterized by greater values compared to the previous curve. At a magnetic field strength of zero ($H = 0$), the reorientation of magnetic domains within a material occurs gradually (slow return), leaving a residual magnetic induction inside the material known as remanence or remanent magnetic induction, B_R. The highest remaining magnetic induction when materials are fully magnetized is referred to as retentivity. This is the most well-known feature of ferromagnets. It is worth noting that in the technical literature, a distinction is made between remanence and remanent induction. The physical quantity known as remanence pertains to the measurement of the remaining induction or magnetization of a magnetic material after the removal of the magnetic field, following its saturation during magnetization. On the other hand, the term remanent induction or magnetization is specifically employed when the magnetic field is removed subsequent to magnetization at an arbitrary level. As a result, the remanence emerges as the constraining element for all remanent inductions.

In order to totally eliminate the retentivity of the materials, it is necessary to apply an opposing magnetic field known as coercivity, coercive force, or coercive magnetic field strength (H_c). The phenomenon of nullifying magnetic induction is commonly referred to as demagnetization. Similar to the concept of remanence, a differentiation can be made between the coercive field, which denotes the magnetic field strength necessary to diminish magnetization to zero from any given level, and the coercivity, which signifies the magnetic field strength required to diminish magnetization to zero from saturation. In this framework, coercivity serves as the maximum threshold for all coercive fields. The induction of a more intense magnetic field elicits the aforementioned reversal phenomenon, leading to the saturation of the material. The B-H curve is completed when the magnetic field is reversed. The hysteresis curve or loop refers to the entire curve. The attainment of zero magnetization at zero field can only be achieved through the process of heating the materials beyond the Curie temperature, which leads to the creation of a new system consisting of randomly oriented magnetic domains. As a result, the four parameters of B_S, B_R, H_C, and H_S completely characterize the magnetic characteristics of ferromagnetic materials. The surface area below the curve, on the other hand, indicates the stored magnetic energy per unit volume of material, represented in $J.m^{-3}$. As a result, the magnetic energy loss per unit volume of material is represented by the specific area bordered by the magnetization and demagnetization curves which is depicted in hysteresis loop.

It is important to acknowledge that the magnetic permeability of ferromagnetic materials is not a constant physical number, but rather varies depending on a specific region of the B-H diagram. Hence, the utilization of magnetic permeability as a means to characterize ferromagnetic materials is deemed inadequate because of the presence of the hysteresis loop. This loop allows for the generation of virtually any permeability value, including infinite permeability at remanence (where magnetic field strength, H, is zero and magnetic flux density, B, equals the remanent flux density, B_R) and zero permeability at coercivity (when H equals the coercive field strength, H_c, and B is zero). The magnetic permeability at the start of the B-H curve is referred to as the initial magnetic permeability (μ_{in}). On the other hand, the maximum magnetic permeability (μmax) obtained from the origin is known as the maximum magnetic permeability (μ_{max}). Lastly, the magnetic permeability measured for an applied alternating magnetic field is termed as the AC magnetic permeability. Differential permeability is a physical property that possesses greater utility, $\mu = \partial B/\partial H$.

A detailed investigation of the hysteresis curves of several ferromagnetic materials allows us to divide them into two separate categories (**Figure 1.4**):

1. substantial coercivities, often exceeding 10 kA.m^{-1} (previously 125.67 Oe), substantial hysteresis core losses, and a wide hysteresis loop characterize retentive or hard ferromagnetic materials. When the magnetic field is turned off, they retain their magnetization and are utilized as permanent magnets.
2. Softferromagnetic materials have high permeabilities, low coercivities (often below 1 kA.m-1 or previously 12.567 Oe), low retentivities, minimal magnetic hysteresis core losses, and short hysteresis loops. Due to their notable permeabilities, these materials exhibit the ability to be magnetized by moderate magnetic fields and maintain a residual magnetic induction upon the cessation of the magnetic field. Moreover, their low coercivity obviates the need for a high reverse magnetic field to nullify the magnetic induction. The extensive utilization of these materials as fundamental components in electromagnets can be attributed to their wide-ranging applicability.

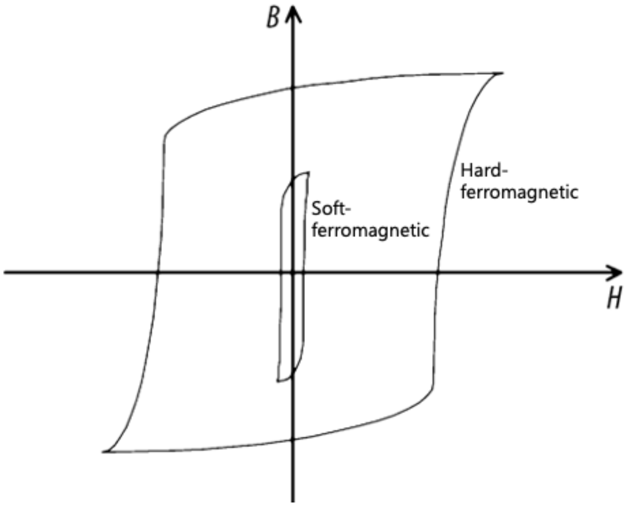

Figure 1.4. B-H hysteresis loop for soft-ferromagnetic and hard-ferromagnetic materials. Adapted from [6]

1.2.3 Permeability

Permeability is a fundamental property of materials that describes their ability to allow the passage of magnetic fields. It quantifies the material's response to the magnetic field by indicating how easily it can be magnetized. Permeability is represented by the symbol μ and is typically measured in units of Henrys per meter (H/m) or Tesla meters per ampere (T·m/A). In the context of electromagnetism, permeability is divided into two main categories: absolute permeability (μ) and relative permeability (μ_r). Absolute permeability (μ) refers to the intrinsic property of a material to conduct magnetic flux and is defined as the ratio of the magnetic flux density or magnetic induction (B) to the magnetic field strength (H) in a vacuum.

Relative permeability (μ_r) measures the magnetic response of a material compared to that of a vacuum or free space. It is calculated as the ratio of the absolute permeability (μ) of the material to the permeability of free space (μ_0), expressed as

$$\mu_r = \mu/\mu_0 \qquad (1.5)$$

Relative permeability provides a way to compare how easily a material can be magnetized compared to a vacuum. Materials with a relative permeability greater than 1 are considered magnetically responsive, while those with a value less than 1 are diamagnetic and have a reduced magnetic response. The value of permeability can vary significantly across different materials. In general, magnetic materials such as iron, nickel, and ferrites exhibit high relative permeability, making them excellent choices for applications requiring strong magnetic fields. On the other hand, non-magnetic materials like copper and aluminum have a relative permeability close to 1, indicating a minimal response to magnetic fields. Permeability is a critical parameter in numerous electromagnetic applications, including transformers, inductors, magnetic sensors, and magnetic shielding. By selecting materials with appropriate permeability characteristics, engineers can optimize the performance and efficiency of these devices. Additionally, the knowledge of permeability helps in analyzing magnetic circuits, calculating magnetic forces, and predicting magnetic field distributions in various systems.

1.2.4 DC bias characteristics

The DC bias characteristics of a powder core inductor refer to its behavior when subjected to a direct current (DC) bias or a steady-state current or saturation current (I_{sat}). This characteristic is of particular importance in applications where the inductor operates in the presence of a constant or fluctuating DC current component, such as in power electronics and energy conversion systems. When a powder core inductor is exposed to a DC bias, several factors come into play that can affect its performance. One such factor is the phenomenon of DC bias saturation. Saturation occurs when the magnetic flux density in the core material reaches its maximum limit, causing a significant reduction in inductance or permeability. The I_{sat} value is determined by the deteriorated inductance or permeability up to 30% from its initial value. In powder core inductors, the design and selection of the core material play a crucial role in determining the level of DC bias saturation. Compared to other core materials such as ferrite, powder cores often exhibit improved DC bias characteristics. **Figure 1.5** exhibited the obvious comparison of DC bias curve between ferrite with concentrated air gap and the powder core (FeSiAl) with distributed air gap. The ferrite can maintain the permeability closer to unbiased value in the increasing of magnetic field or current load, but the permeability plummeted as soon as the ferrite reach the saturation point. In contrast, the FeSiAl powder core shows the slow deterioration of the permeability so that the saturation materials can be maintain even when the magnetic field or the current load increases remarkably.

The combination of high permeability and low coercivity in powder core materials allows them to withstand relatively high levels of DC current without saturating. This characteristic makes powder core inductors suitable for applications that require operation in the presence of substantial DC bias, such as power supplies and motor control circuits. However, it is essential to consider the effects of DC bias on the inductor's performance. Increased DC bias can lead to higher core losses, resulting in increased power dissipation and reduced efficiency.

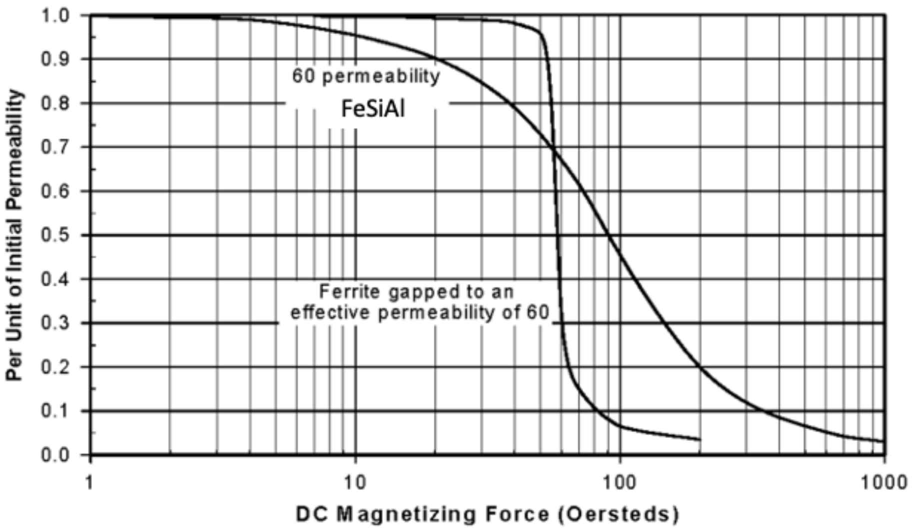

Figure 1.5. DC bias curves for Ferrite and FeSiAl powder core. Adapted from [8]

1.2.5 Powder core loss

The powder core loss of a powder core inductor refers to the energy dissipation that occurs within the powdered magnetic core material when subjected to alternating magnetic fields. This loss is an important consideration in the design and performance of inductive components used in various applications, including power electronics and high-frequency systems. Powder core materials exhibit relatively low core losses compared to other magnetic core materials, such as laminated iron cores or ferrite cores. The unique microstructure of powder cores, composed of small magnetic particles, contributes to their improved performance in terms of core loss. The distributed air gaps between the particles reduce eddy current losses and enhance the overall efficiency of the inductor.

The powder core loss primarily stems from two main mechanisms: hysteresis loss and eddy current loss. Hysteresis loss occurs due to the magnetization and demagnetization of the core material during each AC cycle. As the alternating magnetic field causes the core material to undergo repeated magnetic reversals, energy is dissipated in the form of heat due to the magnetic domain realignment process. The ability of powder cores to exhibit low hysteresis loss is attributed to their unique composition and microstructure. Eddy current loss occurs when an alternating magnetic field induces circulating currents, referred to as eddy currents, within the core material. These eddy currents generate heat through electrical resistance, resulting in energy dissipation. Powder cores address this issue by incorporating distributed air gaps that restrict the formation and flow of eddy currents within the core material. When a ferromagnetic material is exposed to an alternating magnetic field, it triggers an electromotive force (emf) in volts, which in turn generates eddy currents. The power released per unit mass of the magnetic material, known as Joule's heating or eddy current losses, is denoted as P_e and is measured in W/kg. These losses are also referred to as Foucault current losses. At low frequencies (expressed in Hz), the magnetic flux completely penetrates the material, and the depth of penetration is directly proportional to the square root of the reciprocal of the electrical resistivity. In that case, for instance, the eddy-current losses in a ferromagnetic sheet can be calculated by the following equation:

$$P_e = (\pi l f B_m)^2 / 6\rho \qquad (1.6)$$

Where The equation provided represents the relationship between several parameters in the context of eddy-current losses. P_e denotes the eddy-current losses measured in watts per kilogram, l signifies the thickness of the metal sheet in meters, f represents the frequency of the magnetic field (hertz, Hz), B_m represents the magnetic field induction in tesla (T), and ρ is the electrical resistivity measured in ohm-meters. At higher frequencies and with a constant flux amplitude, the eddy-current losses predominantly occur inside a narrow surface layer of the material, known as the skin effect. These losses are directly proportional to $f^{3/2}$.

1.2.6 Powder core materials

Powder core inductors are classified into different types based on the soft-ferromagnetic material used in their core and the application they are designed for. In the consideration of the used material in a powder core, **Figure 1.6** represents the range of permeability, magnetic saturation, coercivity and the price of different materials for powder core.

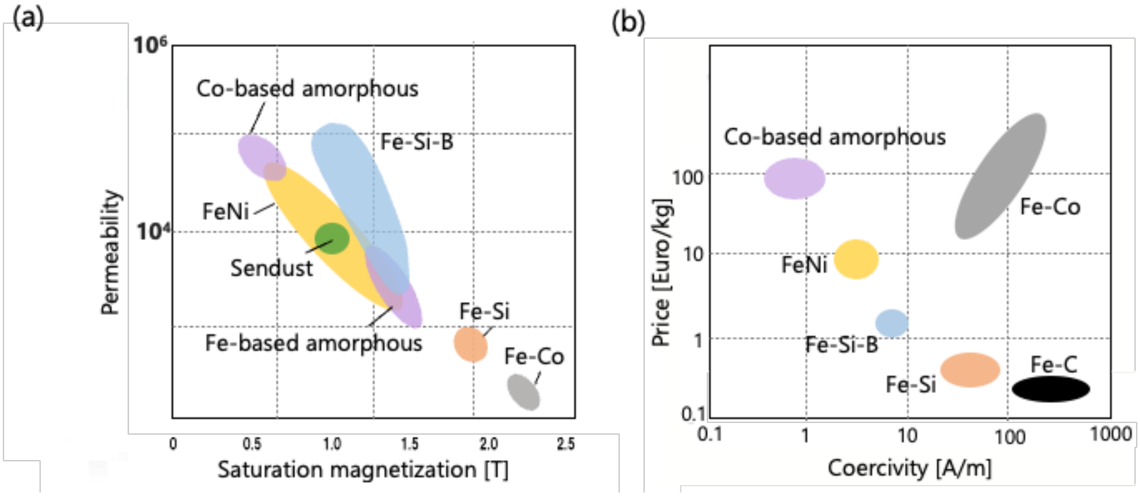

Figure 1.6. (a) Relationship between permeability and saturation magnetization, (b) Relationship between price and coercivity from various soft-magnetic particles. Adapted from [9]

The types of powder core inductors and their development are described as follows:

1. Molybdenum Permalloy Powder cores (MPP) are produced from very fine particles of an 81% Ni, 17% Fe, and 2% Mo alloy [10]. The MPP core was initially introduced in 1940 with the primary purpose of compensating for capacitance in lengthy telephone lines [11]. MPP powder core inductors are best suited for power applications where a high level of energy storage is required in a small size. This is because they have a high saturation flux density, low core loss, and low temperature coefficient of inductance [8]. This makes them ideal for use in power supplies, DC-DC converters, and audio circuits. One of the main advantages of MPP powder core inductors is their excellent inductance stability after high DC magnetization or under high DC bias circumstances. This is crucial in applications where the inductor is subjected to high DC current or where the magnetic field must be

held stable over a wide range of temperatures. MPP powder core inductors also have magnetic saturation of 0.8 T and a relative permeability ranging from 14 to 550, which allows them to handle a wide range of frequencies. Another advantage of MPP powder core inductors is their high resistivity. This means that they are able to resist the flow of electric current, which reduces energy losses and allows for more efficient operation. MPP powder core inductors also have low hysteresis and eddy current losses, which means that they are able to operate at high frequencies without generating excessive heat. However, MPP cores are costly and limited in toroidal shapes compared to other cores. This can make them less practical for certain applications where cost or shape is a factor.

2. High Flux Powder cores (HF) are produced from very fine particles of 50% Ni and 50% Fe, which gives them unique magnetic properties compared to other types of powder core inductors. Similar to MPP cores, HF cores are suitable for applications where high levels of energy storage are required in a small size. In fact, they have a high magnetic saturation up to 1.5 T and permeability ranging from 14 to 160, making them ideal for use in power supplies, DC-DC converters, and audio circuits. One of the main advantages of HF cores is their magnetic characteristics, which allow for the smallest size design with low core loss, the best DC bias characteristics, and lower cost than MPP cores. This makes them ideal for applications where cost, size, and efficiency are important factors. Additionally, HF cores have excellent inductance stability after high DC magnetization or under high DC bias circumstances. This is crucial in applications where the inductor is subjected to high DC current or where the magnetic field must be held stable over a wide range of temperatures. Moreover, HF cores have relatively low hysteresis and eddy current losses, which means that they are able to operate at high frequencies without generating excessive heat. This makes them suitable for high-frequency applications such as switch-mode power supplies and radio frequency circuits. This core is also only available in toroidal shape.
3. Sendust Powder cores are a type of powder core inductor that use an alloy of 85% Fe, 9% Si, and 6% Al as its core. They were first invented in 1936 by researchers in Sendai, Japan, with primary use cases in telephony [11] The name "Sendust" is derived from the combination of Sendai and "dust" core. One of the key advantages of Sendust cores is their affordability compared to other types of cores, making them a cost-effective alternative to MPP and HF cores. They also offer a notable reduction in losses, which is a significant benefit for applications that require high efficiency. Sendust cores have a saturated magnetic value of 1 T and a permeability ranging from 26 to 125, which are comparable

to other types of cores. Their relatively low permeability means they are suitable for use in a wide range of applications, and their high saturation level allows them to handle high currents without saturating, which can distort the output signal. Another advantage of Sendust cores is their ease of handling and manufacturing. The absence of Ni in the alloy makes them relatively cheap to produce, and they are also easy to shape into the desired form.

4. Iron powder cores are are produced using pure Fe or FeC powder [12] and were firstly invented in 1831. They were chosen owing to the magnetic saturation value of Fe which is the highest among soft-magnetic material (2 T). One of the main advantages of iron powder cores is their economic cost compared to other powder core types such as MPP, HF, and Sendust. Additionally, they are highly flexible and can be shaped into many different forms, making them ideal for a wide range of inductor designs. These factors contribute to their popularity and widespread use. Iron powder cores have a saturated magnetization of 1-1.5 T and a permeability ranging from 1-90, which makes them suitable for use in various applications. However, one of the drawbacks of iron powder cores is their relatively high core loss, which can be compensated for by using larger core sizes. Moreover, this core requires a binder, typically epoxy, to isolate the grain particles, which can cause magnetic properties to change over time with extended use.
5. Amorphous and nanocrystalline alloy powder cores were initially reported by Duwez and Lin in 1967. They conducted rapid solidified method in obtaining Fe-P-C system [13]. Further, there is an interest in the use of Fe and Co-based amorphous alloys in the mid 1970. This led to the powder core which has excellent coercivity and saturation magnetic. In 1988, researchers from Hitachi incorporated Nb and Cu additives into the production process of amorphous alloys. Additionally, an annealing step was introduced. These modifications resulted in the creation of small and closely distributed iron or cobalt-based nanocrystals, approximately 10 nm in diameter, within the amorphous matrix. This significant development marked the first generation of nanocrystalline alloys [14]. Furthermore, other nanocrystalline families based on the Fe-Si-B and Fe-Co systems were developed [15,16]. The most common composition of Fe-Si-B system is $Fe_{73.5}Si_{13.5}B_9Nb_3Cu_1$, the first commercialized nanocrystalline alloy [17]. Regarding the Fe-Co system, although it increases the saturation magnetic value from 1 to 1.2 T, and extend the durability of the powder core, the manufacturing of this core is challenging during impregnation and cutting process. Moreover, this core is relatively expensive in comparison to the FeNi alloy.

1.3 The advancement of the powder cores.

To maximize the magnetic characteristics of a powder core such as magnetic saturation, permeability, high DC bias current, and low powder core loss, there are several strategies that have been conducted by several researchers. The remarkable advancement strategies have been reported. First, changing the particle size in a powder core. The magnetic properties of a powder core, including its permeability and saturation level, depend on the shape and size of the core, and the manufacturing process. Second, incorporating secondary material, which has smaller size. The addition of the secondary particle in a certain amount can improve the magnetization. Third, adding insulating material among particles. The coating material can improve the resistivity of the particles, which reduces energy losses and improves efficiency. It can also reduce eddy current losses, which can occur when a magnetic field induces a current in the core material. **Table 1.1** provides a comprehensive analysis of the alterations in magnetic properties of powder cores that result from those strategies.

Table 1.1. Effect of the different enhancement strategies on the powder core magnetic characterization

Strategy	B_s	H_c	μ	I_{sat}	P	remark	Ref.
reducing particle size	⇅	⇅	⇅	↑	⇅	smaller size of particles enhanced the DC bias current	[18–22]
Incorporating secondary particles	↑	⇅	↑	⇅	↓	secondary particles addition improves the magnetic saturation and permeability	[22–26]
coating particles	↓	⇅	⇅	⇅	↓	coated particles effectively reduce the core loss	[27–31]

*B_s: Magnetic saturation; H_c: coercivity, μ: permeability, I_{sat}: DC bias current, P: core loss

1.3.1 Reducing the particle size of the powder core

In the latest two decades, some researchers have reported the effect of the reducing particle size on the magnetic characteristic of a powder core. A study conducted by Otsuka et al. showed that the powder core made by different size of Fe-Si-B based particles using cold pressing and sintering method holds different magnetic characteristics. The reducing size range (<150 μm and <45 μm) and average diameter of the particles (d_{av} 27 μm and d_{av} 22 μm) successfully enhanced the magnetic characteristic of the powder core, which was pointed by the increasing of DC bias current characteristic (I_{sat}) and the decreasing of coercivity and core loss [18]. Similar result had been reported by Yabu et al., Fe-Si-B based powder was prepared by annealing at 400 and 300°C resulted in particles size about 12.8 and 2.4 µm. The changing of the particles size from 12.8 to 2.4 µm exhibited the increasing of the saturated magnetic and DC bias current values. It is pointed that although the coercivity increased in the decreasing particles size due to thinner oxide layer from the lower annealing temperature, the core loss analysis showed a remarkable alleviation, indicating an overall enhancement on the powder core properties [22].

Although it was reported that decreasing the particles' size in the powder core showed a significant improvement on the DC bias and core loss performance, the use of different method in preparing the particles such as milling provided in increase on the core loss. Woo et al. investigated different size of Fe particles with Fe above 98% containing ~0.01% Cu, 0.002% Pb, 0.005% Zn and some oxides. The particles' size was reduced by milling for 0, 20 and 40 h to result the particles with the size of 150, 50 and 30 mm, respectively. The study represented the increase of DC bias current in the decreasing the particles size, the core loss elevated due to the arising plastic and elastic deformation within individual particles during long time milling [19]. It is also supported by other study that the decreasing of the particles size yielded a constant magnetic saturation value, yet the increasing of coercivity. It also be caused by the high stress and defect of the surface oxide owing to the milling time [21]. On the other hand, a study using gas atomization method showed that the decreasing of Fe-Si-B based particles with different size ranging from 81 to 20 µm resulted in the decrease coercivity and core loss [20]. These recent studies revealed that different particles' preparation method can change the magnetic characteristic of the powder core with respect to the magnetic saturation, coercivity, permeability, and core loss. However, it is notable that the decreasing of the particles size in a powder core led to the increasing of its DC bias current characteristic.

1.3.2 Incorporating secondary material

In the latest decade, the incorporating secondary particles (fine particles) into primary particles (larger particles) in a powder core has been studied by some researchers. In general, this strategy can improve the magnetic properties of the powder core by increasing the number of magnetic domains within the core and reducing the demagnetization zone. This can lead to higher magnetic saturation, permeability and lower losses, resulting in a more efficient core, as summarized in **Table 1.1**. In 2012, Kim et al. incorporating 3 μm Fe particles into Fe-Si-B particles ranging from 25 to 53 μm. The result indicated that the presence of the smaller particles increased the permeability and decreased the core loss of the powder core [26]. The incorporation of secondary particles into primary particles can increase the density and packing factor of the powder core, which leads to a reduction in core losses. The smaller particles fill in the gaps between the larger particles, resulting in a more uniform distribution of magnetic domains and a higher permeability. Furthermore, another investigation was carried out by Li et al. to combine 50 μm Fe-Si-B based particles and 15 μm FeNi particles. The use of FeNi powder with particles smaller than 15 μm results in an increase in saturation magnetization from 157 to 165 emu/g, indicating favorable characteristics in terms of soft magnetic properties. The addition of 15 wt% FeNi to the cores results in a 41% improvement in permeability, accompanied by a decrease in core loss from 65 to 58 W/kg. The reduction in non-magnetic gaps and improvement in permeability is achieved by the introduction of tiny particles of ferromagnetic powder into the interstices of larger amorphous particles composed of Fe-Si-B [23]. Moreover, Yabu et al. attempted to incorporate an appropriate amount of the secondary particles (Fe-Si-B powder 2.4 μm) into primary particles (Fe-Si-B 12.8 μm), resulting an improvement the magnetic characteristics of a powder core.

Recently, the utilization of the small particles of Carbon Iron Powder (CIP) as the secondary particles as shown in **Figure 1.7.(a)** has been examined by some researchers, Xia et al. and Liu et al [24,25]. suggested that an appropriate amount of CIP is necessary to increase the permeability and decrease the core loss. Xia et al. conducted an investigation on the impact of the supplementary quantity of CIP on the microstructural characteristics, densities, and magnetic properties of FeSiCr powder. When the concentration of CIP was varied from 0 wt% to 50 wt%, notable changes were seen in the relative density and magnetic permeability of the sample. Specifically, the relative density increased from 75.9% to 84.9%, while the magnetic permeability experienced a significant rise of 92.7%. As the quantity of CIP increases, the rate of density growth for FeSiCr powder gradually diminishes. Therefore, when the CIP content was added from 0 to 30 wt%, the core loss had reached lowest point. However, the further increase of CIP resulted in the increasing of core loss because the density of FeSiCr powder had become low, expanding the demagnetization zone.

Meanwhile, the study from Liu et al. revealed that the decreasing of the DC bias current is caused by the high permeability. The effects of CIP content on soft magnetic properties of the Fe-Si-B powder were investigated. The core losses exhibited a decrease with the rise in CIP content within the range of 0 to 20 wt%. This phenomenon can be attributed to the reduction in average particle size resulting from the increased CIP content (see **Figure 1.7.(b)**). In contrast, The core losses exhibited a quick increase when the CIP content ranged from 20 to 70wt%. This can be attributed to the persistent reduction in resistance and the concurrent rise in coercivity. Overall, incorporating secondary particles into primary particles with appropriate amount in a powder core can improve its magnetic properties and make it a more efficient and effective component in electronic devices. When only using the large particles, the magnetic poles between particles induced demagnetization field, while the incorporating of small particles can cancel the magnetic poles to prevent the demagnetization field, as shown in **Figure 1.7.(c)** [22].

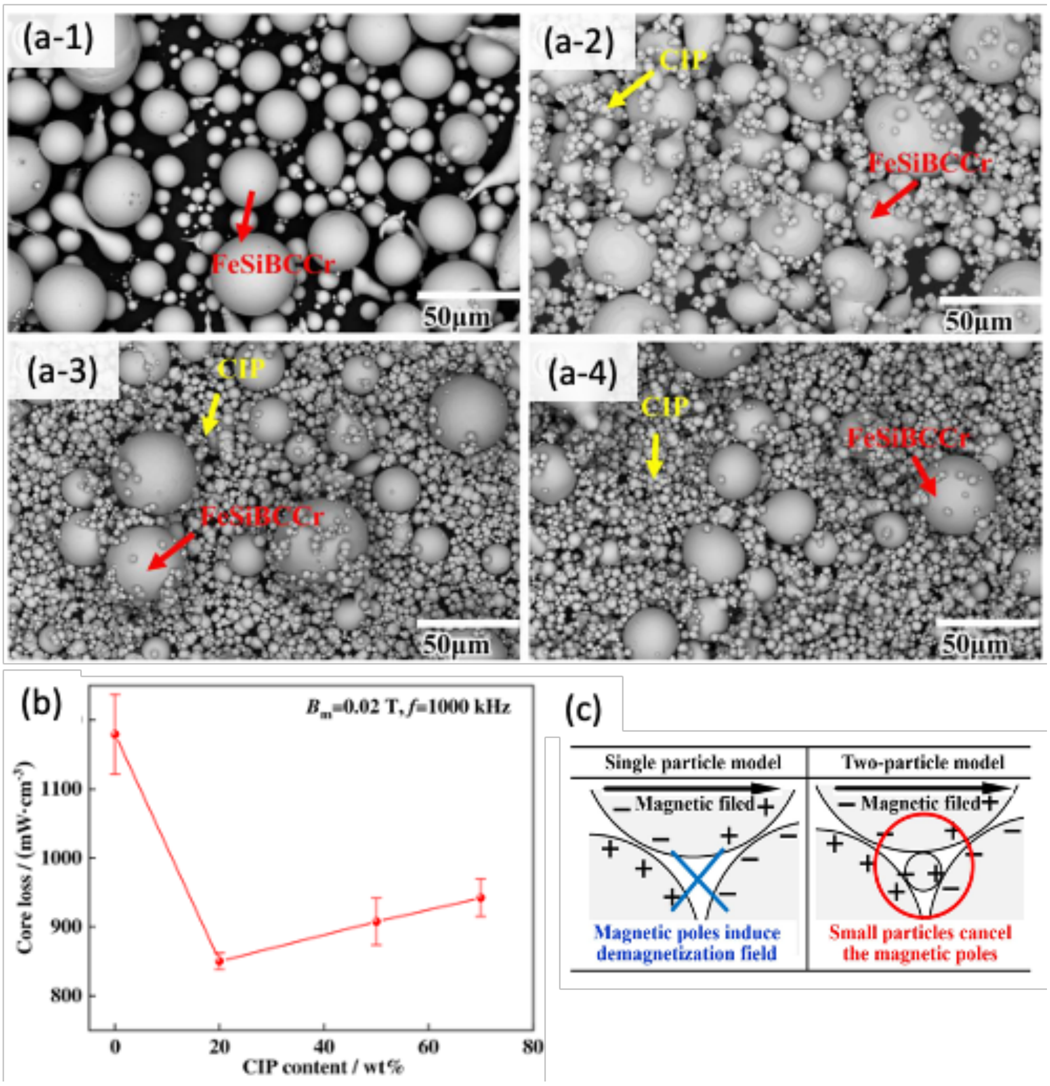

Figure 1.7. Incorporating secondary particles in a powder core: (a) SEM image of powder core comprises of FeSiCr as primary particles and carbonyl iron powder (CIP) as secondary particles with various concentration; 1) 0wt%, 2) 5wt%, 3) 10wt%, 4) 20wt%, 5) 30wt%, 6) 50wt%. (b) Effect of incorporating various concentration of CIP on the core loss of the powder core. (c) schematic image of the cancellation of the demagnetization field caused by the secondary particles. Adapted from [22,32]

1.3.3 Adding insulating materials between particles

In the recent years, a strategy with regards to the coating the particles of a powder core have been investigated by using various coating materials. Coating the particles in a powder core can have both positive and negative effects on the magnetic characteristics of the core. The coating material can improve the resistivity of the particles, which reduces energy losses and improves efficiency. It can also reduce eddy current losses, which can occur when a magnetic field induces a current in the core material. Zhao et al. proposed 55 μm FeNi coated FeSi (FeSi@FeNi) particles to be a powder core. The result indicated that the utilization of FeNi nanoparticles in the pressing process is shown to be highly successful in bridging the voids between the larger FeSi powder particles, resulting in a notable enhancement in the density of the magnetic powder core. When the FeNi nanoparticle concentration reaches 15 wt%, a significant enhancement of approximately 44% in permeability is seen, accompanied by a reduction in core loss of around 22.1%. However, it is observed that the DC bias characteristic decreased due to increasing the permeability [27]. Other coating material such as TiO_2 and MgO were also investigated by Zhou and Wu et al. The particles coated by TiO_2 with concentration of 0.15 ml/g or MgO with the concentration of 0.5 wt% showed exhibited significantly better stabilities at high frequencies, the more prominent DC-bias performances, and the lower core loss compared to those of the uncoated cores [29,31].

Some researchers have also reported that SiO_2 is a good insulating material due to its stability. Lai et al. and Sun et al. studied the effect of the shell thickness on the magnetic characteristics of a powder core [28,30]. The increasing the SiO_2 shell thickness in FeNiMo particles decreased the magnetic saturation value and increase the coercivity due to the thicker shell that playing as air gap to serve demagnetizing field. Nevertheless, the coating particles can improve the permeability and DC bias current and decrease the core loss. Similarly, applying SiO_2 as a coating material to FeSiB particles also exhibited high DC bias current and low core loss, although the coercivity increases. Overall, the effect of coating on the magnetic characteristics of a powder core is dependent on the specific coating material and the manufacturing process used. It is important to carefully consider the potential impact of coating on the core's performance before implementing it in electronic devices. Among the coating materials, SiO_2 hold the most prominent property in the particle performance.

1.4 Synthesis of FeNi and FeNi@SiO_2 particles

According to the previous description, a powder core that primary made by FeSiB particles are frequently used. An incorporating of a secondary particles is critical to increase the powder core performance. Among the soft-magnetic materials, FeNi is a prominent candidate owing to its magnetic characteristic which has both high permeability and magnetic saturation values. In general, the FeNi particles can be produced by several methods, including solid phase, liquid phase, and gas phase. The synthesis method can be determined by the raw materials which are used. In the case of the pure metal of Fe and Ni as a raw material, the solid phase method is highly recommended owing to its simplicity. When the raw material is the metal salt or the metal hydroxide of Fe and Ni, the most common method that has been used is the liquid phase method. In order to get a certain size and individual spherical shape of FeNi particles, the gas phase method is an alternative way due to its versatility in keeping the space of each particle. Pure metal and metal salt can be used as the raw material in the gas phase method. There are some different in the resulted particles characteristics as well as the process advantage and disadvantage from the use of those three kind methods, which can be summarized in **Table 1.2**.

Table 1.2. Features of three kind methods for synthesizing FeNi particles

method	raw material	reduction agent	particle characteristic	pros	cons	ref
Solid phase: Ball mill	Pure metal (Fe, Ni)	N/A	Flakky, lamellar, or spherical particles (micron size)	-easy in controlling the composition of FeNi -simple process -less hazardous	-need long time -need pure metal -limited particles application due to size and shape	[33–37]
Liquid phase: -chemical presipitation -polyol -hydrothermal reaction	metal salt ($FeCl_2$, $NiCl_2$, etc.)	-hydrazine -ethylene glycol	agglomerated and irregular particles (nano – micron size)	-simple process -versatile for large production	-need multiple steps -remained liquid byproduct -limited particles application due to size and shape	[38–44]
Gas phase: -gas atomization -vapor deposition -spray pyrolysis	-Pure metal -metal salt	-H_2 gas -methoxyethanol	spherical and individual particles (nano – micron size)	-easy in controlling the composition of FeNi -spherical & individual particle -direct synthesis	-need high temperature -wide range of particles in some cases -need substrate in some cases -safety issue	[45–51]

1.4.1 Solid phase method for synthesizing FeNi particles

Solid phase method for synthesizing FeNi particles refers to the reaction that proceed in the solid state inside a grinder, i.e., ball mill. In general, the ball milling process involves placing the pure iron and nickel powders into the ball mill along with a grinding medium, such as steel or ZrO balls, as depicted in **Figure 1.8(a)**. The ball mill is then rotated, causing the grinding medium to collide with the powders and break them down into smaller particles. As the powders are ground, they react with each other to form FeNi particles. This method of synthesizing FeNi particles has several advantages. First, it easy to control the final product with different composition of Fe and Ni in FeNi particles. Some researchers have successfully produced FeNi with nearly same composition [33–35]. Moreover, even the higher composition of Fe can be achieved according to some previous investigations [36,37]. Second, it is a simple and cost-effective way to produce FeNi particles in large quantities. Third, the solid phase method is less hazardous than methods that involve liquid or gas phases. However, there are also some drawbacks in the use of this method. In terms of getting FeNi particles with specific shape, i.e., spherical, and individual particles, the ball mill must be operated in a long time and high rotation speed. The operation time is varying depend on the rotation speed, raw material size, and the final composition of the product. For example, Gheisari et al. controlled the shape of the final product from flaky to spherical shape with the diameter above 100 μm by increasing the rotational speed of ball mill from 200 to 500 rpm for 24 h, as shown in **Figure 1.8(b-c)**. However, the higher speed could not assure the spherical particles formation. Djekoun et al. had only obtained the particles with lamellar shape even though high rotational speed and longer time up to 200 h had been applied (refer to **Figure 1.8(d)**). Furthermore, the necessity of the pure metal of Fe and Ni become a concern as well due to its availability which is less abundance in comparison to the metal salt. In addition, this method typically produces the FeNi particles with limited size and shape which make the particles application is limited.

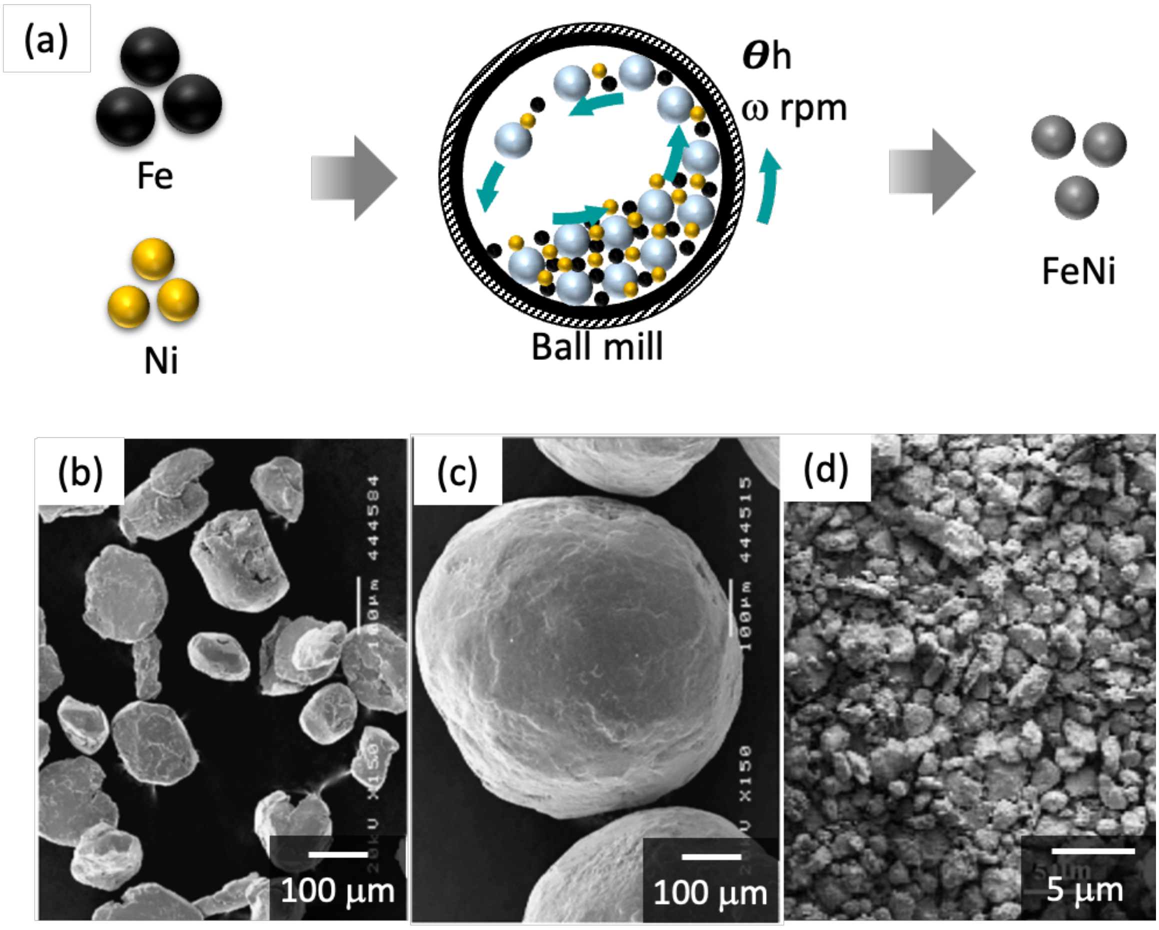

Figure 1.8. (a) Schematic image of FeNi particles prepared by using solid phase method. SEM images of the FeNi particles with different shape: (b) flakes, (b) sphere, (c) lamellar. Adapted from [33,35]

1.4.2 Liquid phase method for synthesizing FeNi particles

Liquid phase method in synthesizing FeNi particles can be referred to the common methods such as chemical precipitation, polyol, and hydrothermal reaction. The chemical precipitation method is a multiple step process that involves the formation of a precursor solution followed by the precipitation of FeNi particles [38]. In the first step, water-soluble salts of Fe and Ni are dissolved in a solvent such as water, forming a precursor solution. Furthermore, a reducing agent is added to the precursor solution, usually hydrazine, which causes the reduction of the metal ions to their respective metals. The reducing agent reacts with the metal ions, causing them to form a solid precipitate of FeNi particles. The second step is filtration of the formed particles from the bulk liquid. The annealing process is generally used as the final step of this method.

Similarly, the polyol method involves using a polyol, such as ethylene glycol, as the solvent and reducing agent for the reaction [44]. The FeNi particles are formed through a multi-step process that involves nucleation, growth, and aging. On the other hand, the hydrothermal reaction method involves using high pressure and temperature conditions, often above 200 °C, to initiate the reaction. **Figure 1.9(a)** represents the schematic process to prepare FeNi particles from metal salt by using hydrothermal reactor which is heated for 2-5 h. This high temperature and pressure cause the formation of FeNi particles through a chemical reaction between the Fe and Ni ions in the solution [41,43]. One of the advantages of the liquid phase method is that it can produce FeNi particles with a narrow size distribution. Contrarily, the liquid phase method often results agglomerated small particles and irregular shape that limits the application of FeNi, as depicted in **Figure 1.9(b-d)**. Another advantage is that the method is scalable and can be used to produce large quantities of FeNi particles. However, it should be noted that the re by-product The chemical composition of the FeNi particles can be tailored by adjusting the concentration of the metal salts in the precursor solution and the type of reducing agent used.

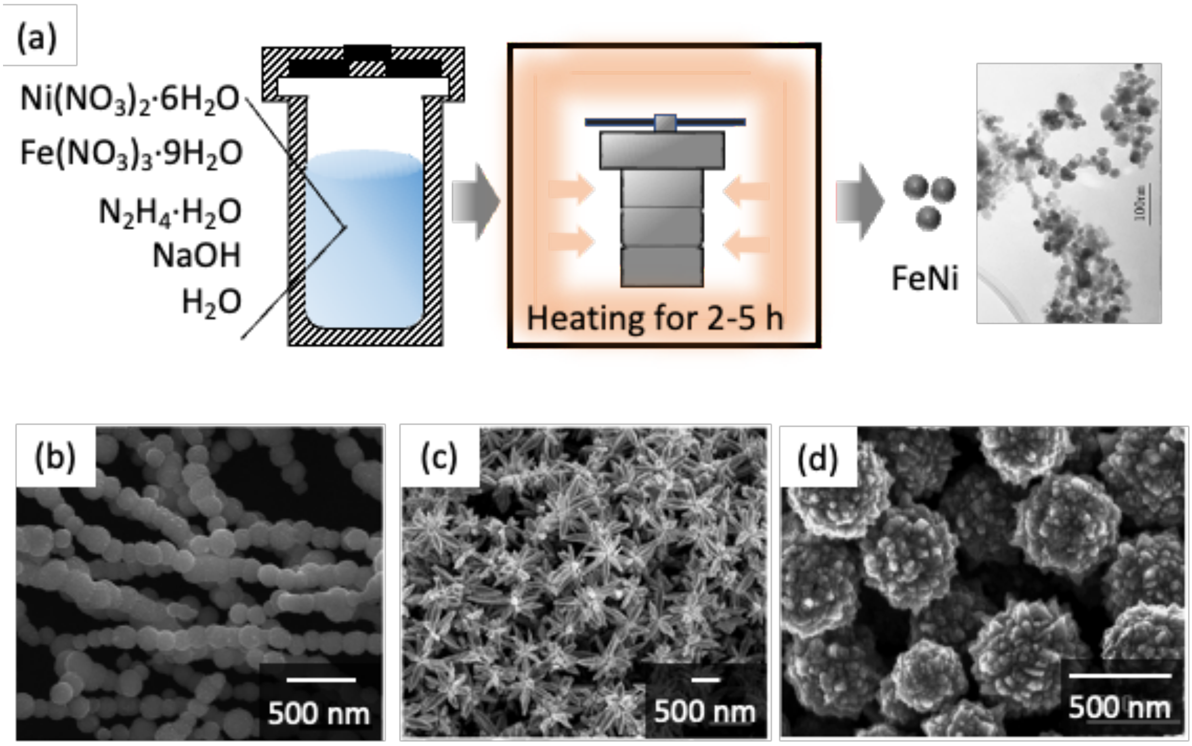

Figure 1.9. (a) Schematic image of FeNi particles prepared by using liquid phase method. SEM images of the FeNi particles with different shape: (b) agglomeration, (b) flower-like, (c) irregular. Adapted from [41–43]

1.4.3 Gas phase method for synthesizing FeNi particles

Gas phase method for synthesizing FeNi particles is conducted by using gas atomization, electrolyte deposition, and spray pyrolysis. The gas atomization method can be applied when the precursor is pure metal of Fe and Ni. Typically, the pure metal is melted using heat induction followed by atomization using high-speed stream gas from nozzle to form small droplets. The droplets are solidified when they are carried by gas stream to the collecting column. The process can be done by flowing an inert gas in a hot wall reactor at high temperature, or flowing 50%H_2-Ar gas in a tube at lower temperature [45]. On the other hand, **Figure 1.10(a)** shows the process of synthesizing FeNi particles via electrolyte deposition method involving several steps. First, a substrate material is chosen, usually made of copper or silica wafer coated by gold, and cleaned to remove any impurities. The cleaned substrate is then immersed into an electrolyte solution containing Fe and Ni ions. An electric current is then passed through the solution, causing the metal ions to be deposited onto the substrate. The amount of metal deposited can be controlled by adjusting the current and deposition time [46].

Among the gas phase method, the spray pyrolysis method is a popular technique for synthesizing nanoparticles due to its simplicity, scalability, and ability to produce particles with controlled size, composition, and morphology [49,50]. The method involves spraying a liquid precursor containing metal salts into high temperature reactor, causing the solvent to evaporate and the metal salts to decompose, forming solid particles, as described in **Figure 1.10(b)**. In the case of FeNi particles, a solution containing Fe and Ni salts is used as the precursor. The high-temperature furnace used in the spray pyrolysis method provides an ideal environment for the decomposition of the metal salts, allowing for the formation of homogenous FeNi particles. The particles produced using this method typically have a narrow size distribution and can be easily tailored by adjusting the precursor concentration, heating temperature, and other parameters. Spray pyrolysis was used to synthesize FeNi particles from an iron-nickel chloride solution in a 100% H_2 environment, yielding smooth and spherical submicron particles (average diameter 400–500 nm). However, there is a drawback in utilizing a 100% H_2 gas environment as the reduction agent, which is dangerous. Another researcher has used methoxyethanol as reduction agent. It has been shown to be a safer method for producing FeNi particles. In this case, nickelocene and ferrocene are employed as raw materials in a 100% N_2 environment. Nevertheless, this technique had some limitations such as a wide particle size distribution, certain relic structures with rough surfaces.

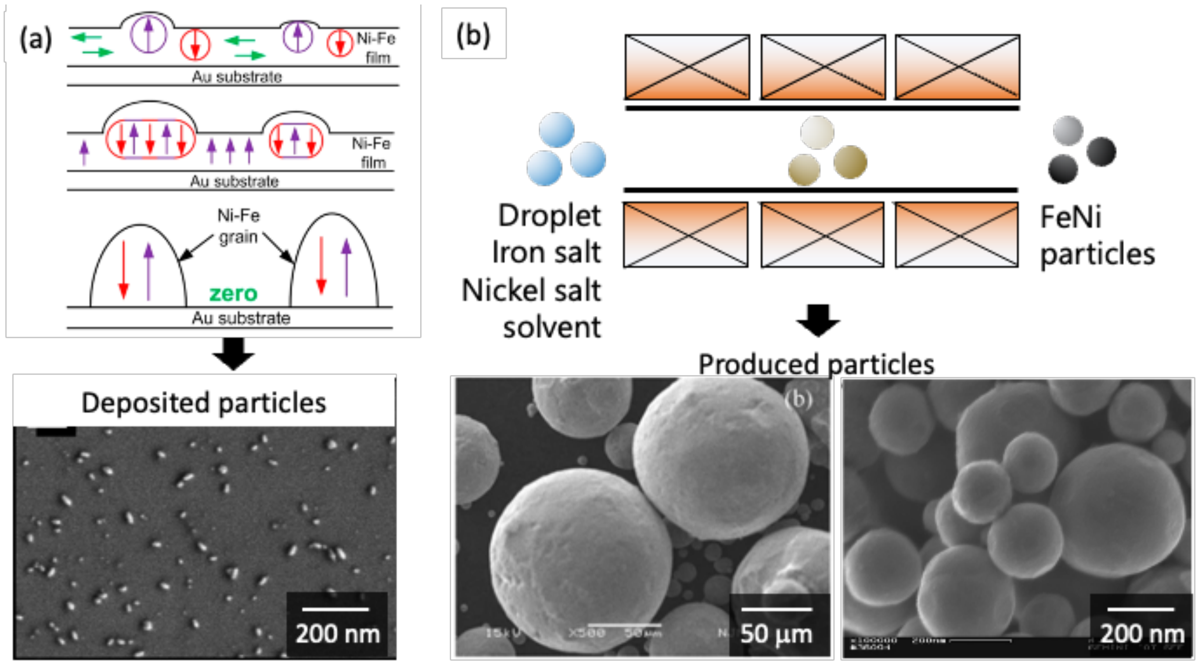

Figure 1.10. Schematic image and SEM of FeNi particles prepared by using gas phase method: (a) electrolyte deposition method, (b) spray pyrolysis method. Adapted from [46,49,52]

1.4.4 Synthesizing FeNi@SiO$_2$ particles

The synthesis of silica coated FeNi particles (FeNi@SiO$_2$) is typically achieved through a sol-gel method, in which the FeNi particles are synthesized at the first and followed by the silica coating. Zhao et al. has reported that the as prepared nano-sized FeNi particles were successfully coated by adding Tetraethylorthosilicate (TEOS) as the silica source following Stober method. The shell thickness could be controlled between 3 and 9 nm. The addition of the shell thickness affected to the decreasing of magnetic saturation value, but the permeability was notably stable as the applied frequency increase. A similar trend has also been reported by some researchers in the study of shell thickness effect of the nano-sized FeNi@SiO$_2$ particles on the magnetic characteristic and stability [53–55]. The Stober method also can be applied for coating the submicron- and micron-sized FeNi particles. Regarding sub-micron size, Yan et al. coated the submicron-sized FeNi particles with the silica shell about 25 nm. In the application of the microwave absorption, the FeNi@SiO$_2$ particles showed a higher permittivity than uncoated FeNi particles [56]. For micron-sized FeNi@SiO$_2$ particles, Zhang et al. has made the particles with nano-sized shell thickness to be applied for powder core inductor. It is pointed that the addition of SiO$_2$ coating on the FeNi particles significantly reduced the powder core loss [57]. Other strategy has been conducted by Jiang et al. and Tang et al. which involves the use of a silica precursor and a precipitating agent to result silica coated particles. This step resulted precipitated or xerogel that contains oxidated Fe and Ni. Thus, the annealing under hydrogen atmosphere is necessary to be conducted at least 600 °C for 5 h [58,59]. Overall, the silica coating via Stober method exhibits some advantages in controlling the shell thickness and its simple process. However, an observable disadvantage from this method is the formation of agglomerated particles, as shown in **Figure 1.11**.

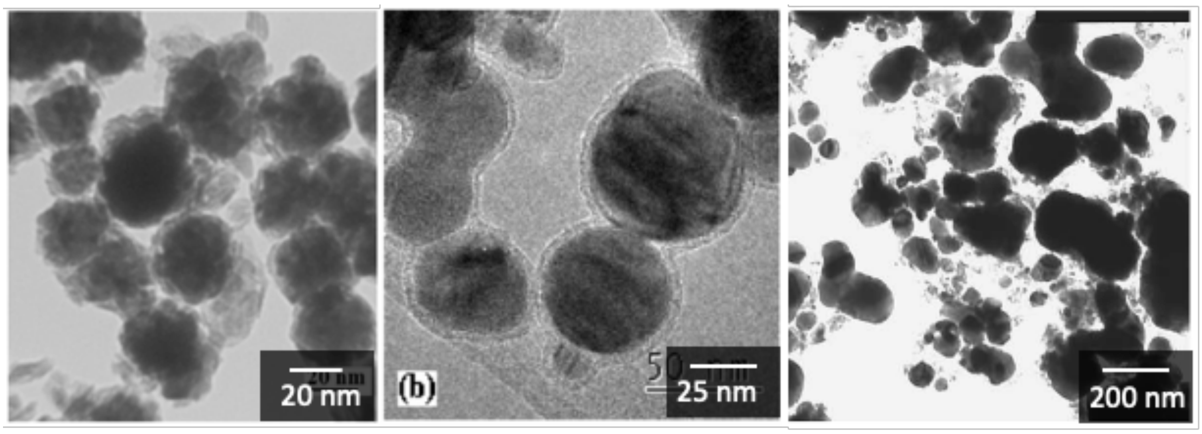

Figure 1.11. Typical TEM images of the agglomerated FeNi@SiO_2 particles prepared by Stober method. Adapted from [53,55,58]

1.5 Study of silica coated particles in gas phase method.

Since the synthesis of FeNi@SiO_2 particles via liquid phase is less favorable owing to the agglomerated particles and its multi-steps, there is a keen in producing FeNi@SiO_2 particles via gas phase method. However, synthesizing FeNi@SiO_2 particles via gas phase route in one-step process has not been done yet so far. Therefore, it is important to understand the silica-coated particles formation in a single step through gas phase route from the other investigations. Principally, the silica coated particles in one step process adapted the chemical vapor deposition (CVD) phenomenon. it is important to change the core precursor in a solid phase before the silica monomer from the gas phase silica precursor is generated. Once the core particles are formed, the silica monomer can attach on the core particles surface due to chemical vapor decomposition and/or scavenging. Otherwise, when the silica solid is generated at first, the silica will become the core materials instead of the shell materials. To realize the CVD process of the coating material onto the core material, the several assisting equipment have been used such as hot wall, photoinduction, plasma irradiation, flame, and electrical beam. These methods application is summarized in the **Table 1.3**.

Table 1.3. Synthesis of the silica-coated particles in gas phase route according to the previous researches.

Particles characteristic	Equipment	core – shell sources	Atmos-phere	Finding	remark	ref.
$TiO_2@SiO_2$ d_{av}: 800 nm t_s: 5-100 nm	Hot wall tubular reactor (T: 1300 - 1500 °C)	$TiCl_4$ - $SiCl_4$	$N_2 + O_2$	Increasing temperature and number of core particles as well as adding water vapor in the reactor are important to obtain denser and smoother coated particles	The process is simple and flexible	[60,61]
$Fe_2O_3@SiO_2$ d_{av}: 50 nm t_s: 5 nm	Hot wall tubular reactor (T: 400 - 1400 °C), premix precursor	IPC - TMDS	N_2	the core-shell structure can be obtained due to the higher reaction rate from the gas phase to the solid phase of the core material than the shell material.	The two precursors must have near vapor pressure	
$Ag@SiO_2$ d_{av}: 50 nm t_s: 0.5 - 11 nm	Hot wall tubular reactor (T : 300-400, 600 °C) with photoinduction	Ag - TEOS	$N_2 + O_2$	-Controlling temperature (400 °C) and number of core particles are important to prevent homogeneous nucleation and particles agglomeration. -Increasing TEOS feed flow rate and additional gas can increase the shell thickness	This process allows a low temperature	[62]
$Si@SiO_2$ d_{av}: 58 nm t_s: 4-6 nm	Tubular reactor with plasma microwave irradiation	SiH_4 - TEOS, HMDSO, OMCTS	Ar carry SiH_4, Ar+O_2 carry coating material	-TEOS is favored to prevent homogeneous nucleation & impurities. -homogeneous nucleation can be confirmed by measuring SSA, the higher SSA means that the higher amount of free silica. -O_2 is important to proceed oxidation reaction to SiO_2	Technology plasma demands higher energy	[63]
$Au@SiO_2$ d_{av}: 20 nm t_s: 4 nm (TEOS), 20 nm (HMDSO)	Hot tubular reactor (200 - 250 °C) with plasma	Au - TEOS HMDSO	Air + N_2	-TEOS gives symmetric coating with less unwanted material. -By employing plasma, the coating particles can be done at 24 °C by using TEOS, while using HMDSO only succeed in a high temperature		[64]
$Fe_2O_3@SiO_2$ d_{av}: 22.4 nm t_s: 2-4 nm $TiO_2@SiO_2$ d_{av}: 40 nm t_s: 2-4 nm	Tubular reactor with flame	$Fe(acac)_3$ – HMDSO TTIP - HMDSO	CH_4, O_2, N_2	-The number of inlet holes in the geometry of the silica precursor introduction is important to facilitate the homogeneous coating. -additional gas rate of the silica precursor should be high to prevent the decomposition delay which lead to the inhomogeneous coating.	This method must involve O_2 as the flame oxidizer	[65,66]
$Cu@SiO_2$ d_{av}: 109 nm t_s: 10 nm $Ag@SiO_2$ d_{av}: 11 nm t_s: very thin	Tubular reactor with electron beam evaporator	ingot pure Cu, Ag - SiO_2	Argon	-coating of Cu is controlled by the different surface tension of Cu and SiO_2 (change to liquid phase). It is important to SiO_2 can solidify before Cu. -Coating of silver is mostly controlled by SiO_2 concentration	This method must use the pure raw material which is less abundance	[67]

1.5.1 Synthesis of silica-coated particles by using hot wall reactor

1.4.1.1 Non-premixed precursors

The first synthesizing of silica-coated particles was conducted by Jain et. al. (1996), to best of my knowledge [60]. Principally, this method attempts to produce silica-coated particles by introducing the silica precursor (gas phase) onto the core particles (solid phase) in a continuous flow inside the hot wall reactor. According to this definition, the spray pyrolysis is included to the chemical vapor deposition. Here, the $SiCl_4$ was used as the silica precursor for coating TiO_2 particles in synthesizing silica-coated TiO_2 particles. Due to favored smooth coating, some parameters were controlled, particularly: 1) high temperature (1700 – 1800 K); 2) large core particles surface area by increasing the particle number concentration ($1x10^5$ – $1x10^7$ #/cm^3); 3) low silica precursor concentration ($2x10^{-7}$ – $2x10^{-10}$ mol/cm^3).

Table 1.4. Coating possibilities in terms of reaction rate and typical scavenging sintering times.

Coating mode	Monomer formation	Scavenging	Sintering	Coating quality
Instantaneous reaction ($\tau_{rxn} << \tau_{res}$)	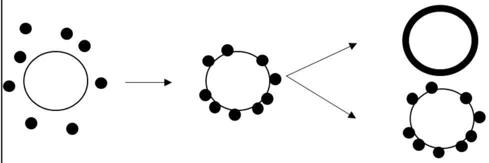			Smooth ($\tau >> \tau_{scav}$) Rough ($\tau << \tau_{scav}$)
Constant reaction rate ($\tau_{rxn} \geq \tau_{res}$) Collision-limited ($\tau >> \tau_{scav}$)	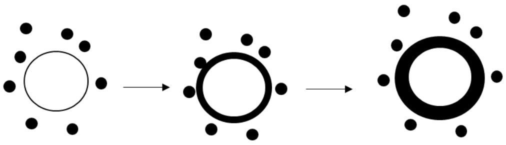			smooth
Constant reaction rate ($\tau_{rxn} \geq \tau_{res}$) Sintering-limited ($\tau << \tau_{scav}$)	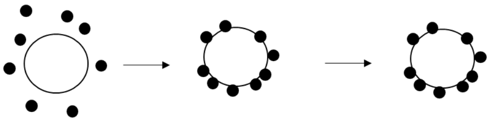			Rough

τ_{res} ⟶

To understand the temperature effect, the characteristic times is important to be considered. Since the aerosol process is complex, the characteristic times determine the different particle growth mechanism. There are 4 different characteristic times: 1) gas-phase reaction time of the shell precursor (τ_{rxn}); 2) scavenging time (τ_{scav}); 3) sintering time (τ); 4) residence time (τ_{res}). The coating mechanism can be classified into two modes, which are instantaneous reaction and constant rate reaction as described in **Table 1.4**. The sintering time and scavenging time are the contributing the coating quality the most, the much higher sintering time resulted in the smoother coating while the much higher scavenging time resulted in the rougher surface. In the low temperature of 1700 K, the constant reaction mode has taken place. Silica monomer particles are continuously generated and increasing their number concentration. Thus, it led to a higher scavenging rate of silica particles which affected the rougher coating. The increasing of temperature to 1800 K can enhance the reaction rate resulted in a collision between silica particles. Hence, the silica particles size was increasing, whereas the silica concentration was decreasing. As a result, the scavenging rate occurred in early stages. However, the large silica is less effective in scavenging which led to the thinner coating.

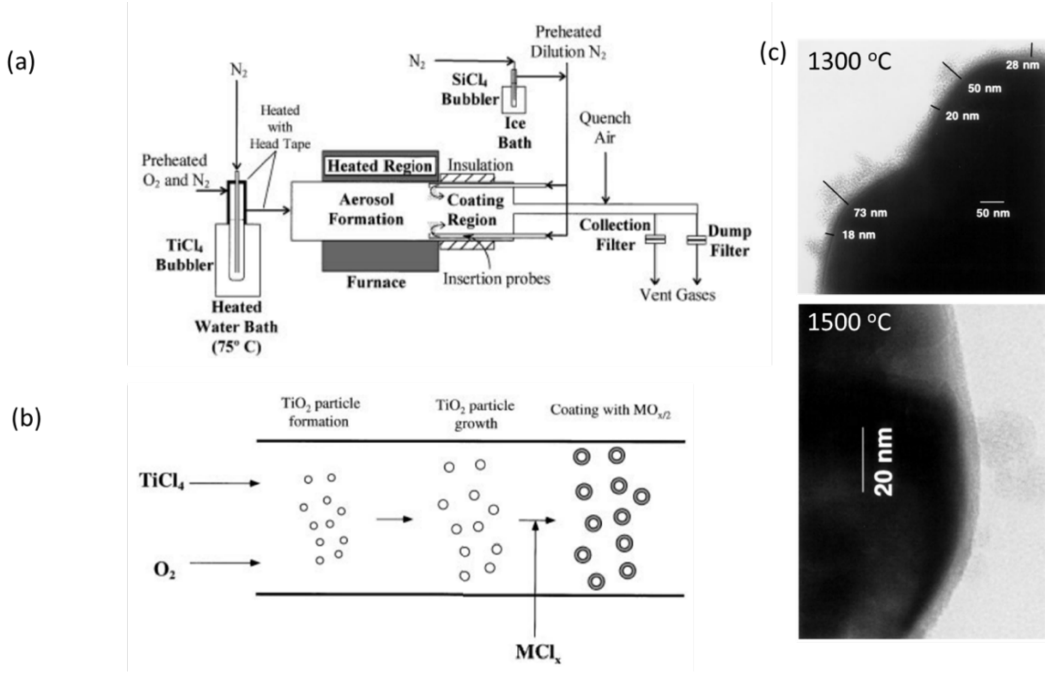

Figure 1.12. Synthesis of silica-coated particles by using hot wall reactor.(a) Experimental apparatus employed in gas-phase coating of TiO_2 particles with SiO_2. (b) Schematic illustration of the in situ gas-phase process for producing silica-coated titania powders. (c) TEM images of the silica-coated titania at 1300 and 1500 °C. adapted from [60,61]

Regarding the effect of the surface area of the core particles, the higher number concentration of the TiO_2 particles (N_A : 10^7 #/cm^3), representing higher surface area, resulted in more effective scavenging of silica particles. The net effect of the enhanced scavenging of silica particles by the TiO_2 particles was counteracted by the dispersion of the total silica volume across a greater surface area. Consequently, a rise in the numerical concentration of titania particles, while holding all other variables equal, resulted in a reduction in coating thickness. In contrast, it was observed that the thickness of the coating exhibited an upward trend when the initial concentration of titania particles dropped. An analogous phenomenon was noted when the initial concentration of titania particles remained fixed but the average particle size was altered. Conversely, an elevation in the initial concentration of the reactant led to a corresponding augmentation in the thickness of the coating. The observed phenomenon can be related to the accelerated creation rate of silica particles through the gas-phase interaction, resulting to a greater concentration of silica particles. Consequently, this rise in concentration has resulted in an elevated scavenging rate. The coating thickness experienced a twentyfold rise when the inflow reactant concentration was increased by a hundredfold to $2x10^{-7}$ mol/cm^3 particles at a temperature of 1800 K. Furthermore, when the intake concentration was reduced by a factor of ten, there was a corresponding tenfold decrease in the coating thickness.

A further discussion of the particle's mechanism was clarified by means of the study of silica-coated TiO_2 using the temperature of 1300 and 1500 ^oC from Powell et. al. (1997). The experimental set-up and the schematic of silica coating is depicted in **Figure 1.12(a-b)**. The result shows that the temperature of 1300 ^oC case resulted in rough coating while that the temperature of 1500 ^oC case resulted in smoother and denser coating surface (see **Figure 1.12(c)**). It can be explained that the coatings were acquired using particle scavenging and/or chemical vapor deposition (CVD) processes at a temperature of 1300 ^oC. However, due to the insufficient temperature, the sintering rates were low, leading to the formation of rough coatings. At an elevated SiO_2/TiO_2 ratio, there was an increased occurrence of particle scavenging and/or CVD, leading to the formation of thicker coatings that exhibited a rough surface texture. At a temperature of 1500 ^oC, the coatings exhibited enhanced densification due to the accelerated rates of sintering. These cases can be illustrated in **Figure 1.13**.

Nevertheless, the augmentation of the mass loading of $SiCl_4$ did not result in a corresponding increase in the thickness of the coating. In contrast, a greater amount of $SiCl_4$ underwent gas-to-particle conversion, leading to the creation of particles that exceeded the size threshold for scavenging and/or sintering into the coating. Hence, by manipulating the rates of particle growth and scavenging/chemical vapor deposition (CVD) of silica, it is possible to achieve thicker coatings at a temperature of 1500 ^oC. This can be accomplished, for example, by augmenting the concentration of titania particles. The enhanced smoothness of silica surfaces seen with increased dilution gas quantities can be attributed to improved mixing resulting from higher gas velocities at the injection probe input, as well as reduced $SiCl_4$ concentrations in the reactor. A reduction in the concentration of $SiCl_4$ would lead to the generation of SiO_2 particles of smaller size through the process of gas-to-particle conversion. The smaller silica particles exhibit increased mobilities and sintering rates. Consequently, the TiO_2 particles exhibit enhanced scavenging capabilities, resulting in more efficient removal of impurities. Furthermore, during the sintering process, these particles facilitate the formation of smoother coatings.

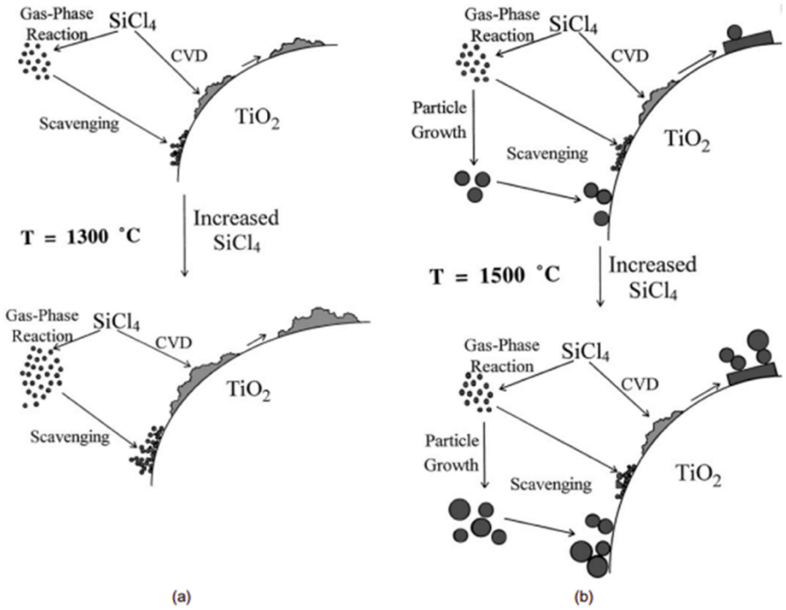

Figure 1.13. Proposed coating mechanism for the silica-coated TiO_2 system and for reactor temperatures (a) 1300 and (b) 1500 °C. Adapted from [61]

1.4.1.2 Premixed precursor

Basak et. al. (2010) demonstrated the synthesis of silica-coated Fe_2O_3 using premixed CVD. **Figure 1.14** described the experimental set-up of the premixed CVD. In this study, Pure Iron pentacarbonyl (IPC) and pure 1,1,3,3-tetramethyldisiloxane (TMDS) were employed as reactants. A mixture of IPC and TMDS in a 1:1 volume-to-volume ratio, prepared in advance, was introduced into the furnace reactor using N_2 gas as a carrier. The decomposition of the reactants took place within a temperature range of 400 to 1400 °C.

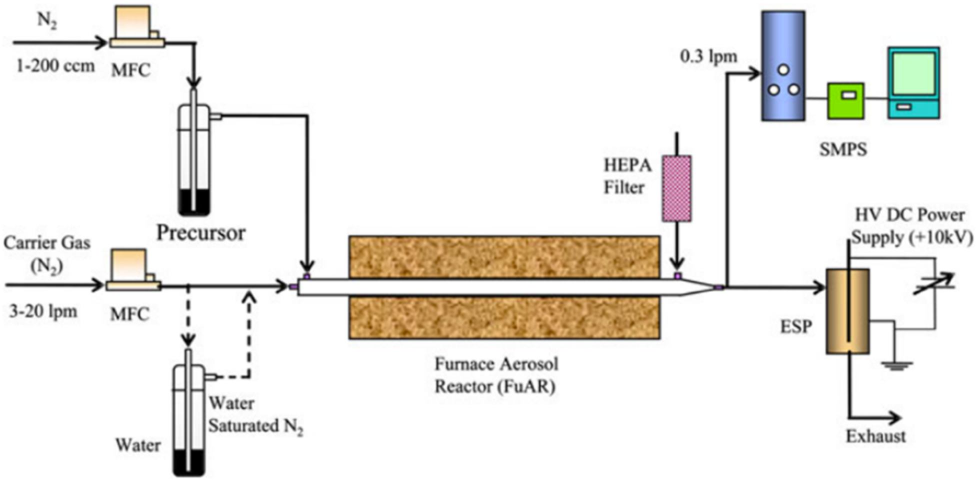

Figure 1.14. Experimental setup to synthesize nanocomposite materials in a single step by furnace aerosol reactor. Adapted from [68]

The study suggests the production of a core-shell type nanocomposite, specifically for a binary system of premixed precursors. This nanocomposite is characterized by the presence of chemically similar cores and shells, with the core composed of oxide A_xO_y and the shell composed of oxide B_pO_q. The precursors used in this system have significantly different decomposition rates, with one precursor (A) having a much higher rate (k_A) compared to the other precursor (B) ($k_A \gg k_B$) or vice versa ($k_A \ll k_B$). When k_A is significantly larger than k_B, the nanocomposite consists of a core composed of A_xO_y and a shell composed of B_pO_q, as illustrated in Path-I of **Figure 1.15**. The production of A_xO_y particles occurs prior to the formation of B_pO_q due to the comparatively elevated rates of oxidation exhibited by precursor P_1. Upon its formation, the A_xO_y vapor undergoes fast nucleation, which is subsequently followed by an increase in particle size by collisions and sintering processes. The subsequent creation of B_pO_q occurs as a result of chemical breakdown following the rise of A_xO_y. Heterogeneous nucleation of B_pO_q may occur on the surface of pre-existing A_xO_y nanoparticles. Ultimately, in the downstream regions of the furnace, the nanocomposite undergoes a sintering process, resulting in the formation of a homogeneous core-shell shape. Similarly, it is possible to produce chemically equivalent B_pO_q covered with A_xO_y by carefully selecting appropriate precursors, as illustrated in Path-III of **Figure 1.15**, where the ratio $k_A \gg k_B$. A chemically different mixed morphology is hypothesized for the degradation of premixed precursors with comparable decomposition rate constants ($k_A = k_B$), as illustrated in Path-II of **Figure 1.15**. The simultaneous synthesis of both A_xO_y and B_pO_q occurs due to their comparable relative decomposition kinetics, subsequently leading to the creation of a nanomaterial consisting of a mixture of oxides.

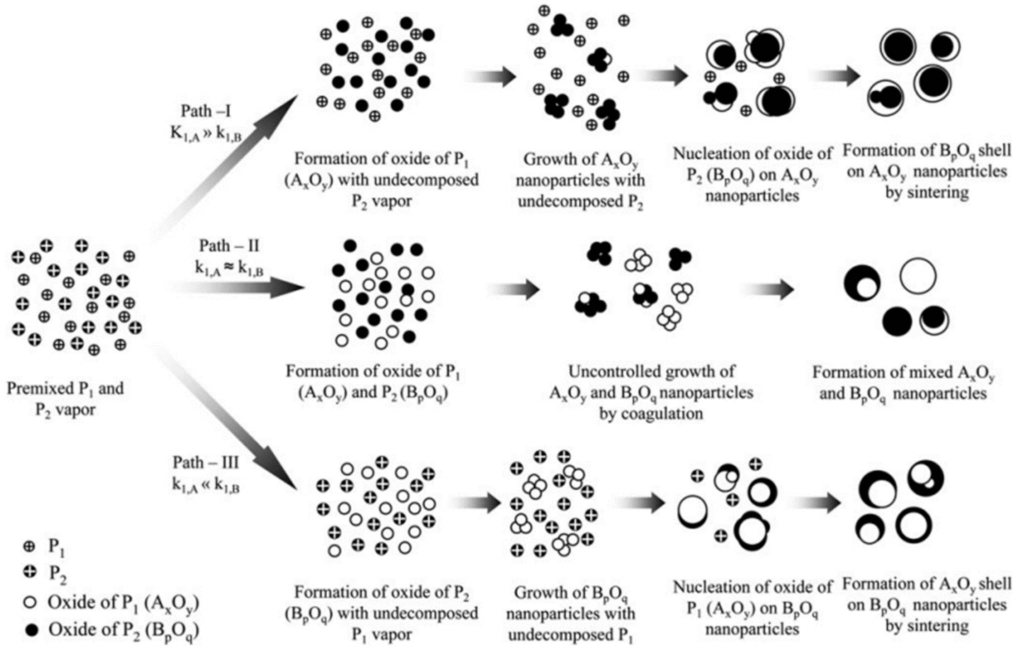

Figure 1.15. Reaction kinetics-based A_xO_y/B_pO_q nanocomposites synthesis mechanism from premixed precursors P_1 and P_2. This work uses IPC and TMDS as P_1 and P_2, Fe_2O_3 and SiO_2 as A_xO_y and B_pO_q. Adapted from [68]

1.5.2 Synthesis of silica-coated particles by using photoinduced assisted hot wall reactor

Boies et. al. (2009) studied the synthesis of silica-coated silver particles via photo-CVD as shown in **Figure 1.16**. The process of photoinduced chemical vapor deposition (photo-CVD) was employed to coat gas-phase silver nanoparticles with silicon dioxide (SiO_2). The study involved subjecting silver nanoparticles, synthesized by inert gas condensation, and a precursor of SiO_2 labeled tetraethylorthosilicate (TEOS), to vacuum ultraviolet (VUV) radiation under atmospheric pressure conditions, while manipulating the temperatures. The vacuum ultraviolet (VUV) photons induce the dissociation of the tetraethyl orthosilicate (TEOS) precursor, thereby commencing a chemical reaction that leads to the formation of silicon dioxide (SiO_2) coatings on the surfaces of the particles. The resulted particles have diameter of 40 nm with the coating thickness of 0.5-11 nm.

By controlling several parameters such as temperature, silica precursor feed rate, and N_2 gas rate for diluting the silica precursor, the difference on the coating behavior is obtained. In the case of the temperature, individual spherical particles can be obtained by employing temperature of 300 - 400 ^oC. When the temperature exceeds 600 ^oC, the homogeneous nucleation has taken place, resulted in separated silica particles generation. In the increasing of the TEOS feed rate, the shell thickness increased proportionally. Compared to the elevating N_2 gas rate, the silica thickness increased considerably. Regarding the number of silver particles, adding the number of particles from 10^6 to 10^7 caused the coating performance was more uniform.

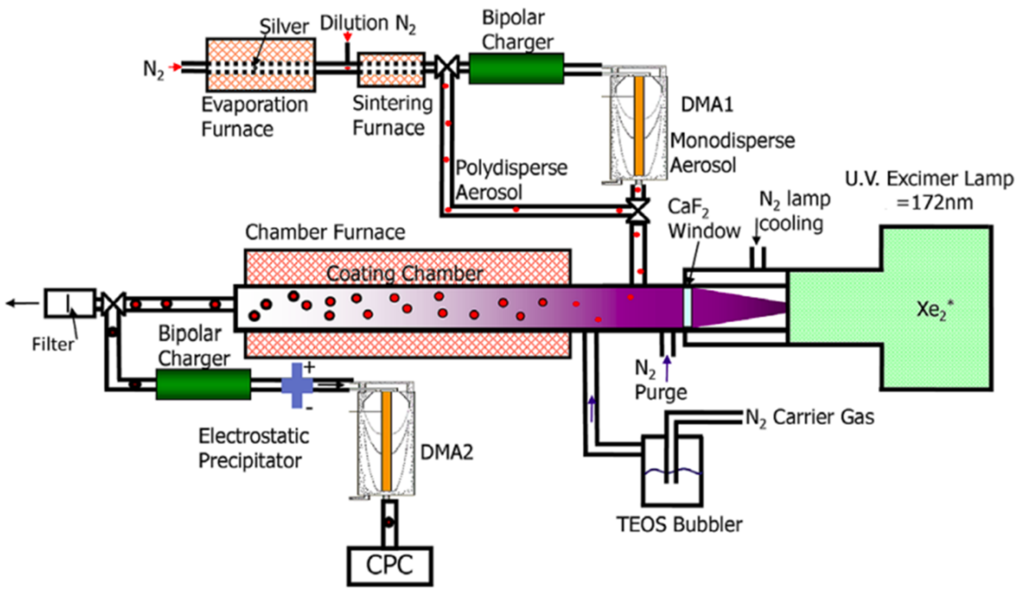

Figure 1.16. Schematic of the photo-CVD coating reactor. Adapted from [62]

1.5.3 Synthesis of silica-coated particles by using plasma microwave irradiation

Dasgupta et. al. (2020) tried to make silica-coated silicone particles. Here, they used three type of silica precursors, i.e. tetraethyl orthosilicate (TEOS), hexamethyldisiloxane (HMDSO) and octamethylcyclotetrasiloxane (OMCTS), while the SiH_4 was used as the silicone core precursor. As can be seen in **Figure 1.17**, the principal mechanism is similar to the furnace reactor. The solid core particles of silicone were produced at first by using plasma microwave irradiation before it was introduced by silica precursor. The resulted particles was around 58 nm in diameter with the coating thickness ranging from 4 to 6 nm. It was found that tetraethyl orthosilicate is favored for thin layers consisting of almost pure silica while hexamethyldisiloxane and octamethylcyclotetrasiloxane (OMCTS) coatings contained reasonable amounts of hydrocarbons. Moreover, OMCTS showed a pronounced tendency towards homogeneous nucleation, thus leading to the additional formation of silica NPs due to homogeneous nucleation. In this report, the specific surface area (SSA) of the synthesized particles were measured. It revealed that the higher SSA might indicate the homogeneous nucleation which resulted in the fine particles formation of the silica since the dense silica-coated Si particles possessed a low SSA. The investigation of the chemical composition of the silica layer revealed that the TEOS-based coating was almost free from carbon while HMDSO- and OMCTS-based coatings contained up to 21% of carbon, which could be identified by means of FTIR spectroscopy and XPS. Experiments with higher concentrations of HMDSO indicated that its tendency towards homogeneous nucleation is slightly reduced compared to OMCTS. Thus, it was possible to achieve coating thicknesses of more than 10 nm. The experiments clearly showed that the in-line coating of pristine NPs within the plasma afterglow works well.

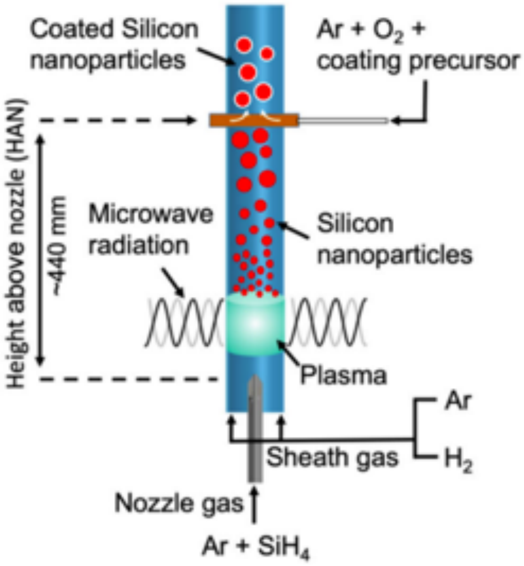

Figure 1.17. Reactor setup used for experiments consisting of quartz tube, plasma nozzle, microwave plasma zone, and coating nozzle located at a distance of 440 mm above the plasma nozzle. Adapted from [63]

Another plasma assisted CVD method was done by Post et. al. (2018), as described in **Figure 1.18(a-b)**. A plasma-enhanced CVD coating process with air was used to produce core-shell particles. Two different coating precursors, TEOS and HMDSO, were used at different temperatures during coating. Differences in the coating morphologies were visible in TEM micrographs for the different combinations of core material, precursor and temperature. While TEOS on Pt or Au resulted in mostly homogeneous coatings, HMDSO formed eccentric coatings on these particles as shown in **Figure 1.18(c)**. For titania particles coated with TEOS at 24 ºC, much of the coating material was collected in the inner parts of the aggregates. The particles average diameter around 20 nm for Au particles. In the case of TEOS, the increasing of furnace temperature in the silica coating zone made the coating thickness is thicker at 200 ºC than that of 24 ºC.

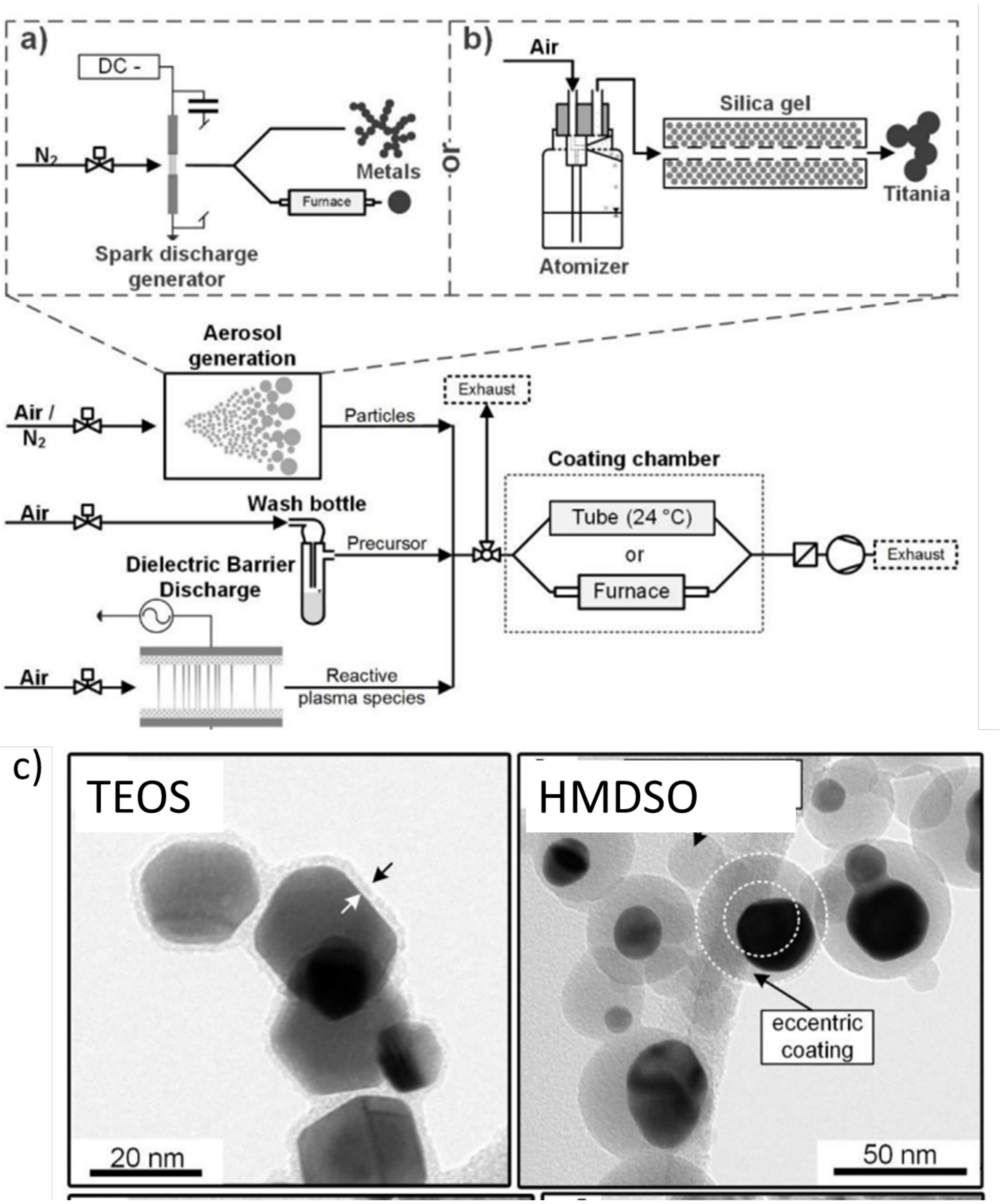

Figure 1.18. Silica coating after plasma-assisted coating. (a) Experimental apparatus. For the core particles, two distinct aerosol generation techniques were used: a spark discharge generator for metals (Pt or Au) (a) and an atomizer for titania (b). The precursors for the coating were TEOS and HMDSO. (c) Gold coated with TEOS and HMDSO. Adapted from [64]

1.5.4 Synthesis of silica-coated particles by using flame reactor

Teleki *et al.* (2008, 2009) used hexamethyldisiloxane (HMDSO) as the SiO_2 precursor in the flame spray pyrolysis technique to exhibit hermetically coating of $Fe_2O_3@SiO_2$ and $TiO_2@SiO_2$ with silica as the shell [65,66]. This gas phase method resulted in a mostly homogeneous coating thickness of approximately 2-4 nm, which has good stability through the isopropanol chemisorption and the photooxidation of isopropanol to acetone analysis. The effect of mixing intensity on product particle morphology was investigated by varying the exit velocity or the number of jet outlets for HMDSO-laden N_2 gas. At high mixing intensity between the TiO_2 aerosol and the HMDSO-laden jet streams, the particles were encapsulated by smooth and homogeneous coatings, 2-4 nm thick. Poor mixing between HMDSO vapor and TiO_2 aerosol along with higher temperatures that accelerated SiO_2 formation in the gas phase resulted in separate SiO_2 and poorly coated TiO_2 particles.

Buesser et. al (2010)[69] Smooth coatings were formed primarily by deposition of freshly formed SiO_2 monomers and sintering of small SiO_2 clusters and to a lesser extent by surface oxidation of HMDSO on the TiO_2 core particles. The concentrations of core aerosol and coating precursor vapor (here HMDSO) had the strongest influence on coating efficiency and shell texture in agreement with the literature. Bigger core particles, at constant production rate, lead to lower coating efficiency. Increasing the coating weight fraction hardly influences the coating efficiency and leads to proportionally higher total coating thickness, but also to rougher coating shells. Low concentrations of coating precursor vapor and high concentrations of core particles lead to high fractions of smooth shells and high coating efficiency. The thickness of these smooth shells could be increased by multiple injections of coating precursor vapor at low concentrations in series, building up smooth coating shells layer-by-layer.

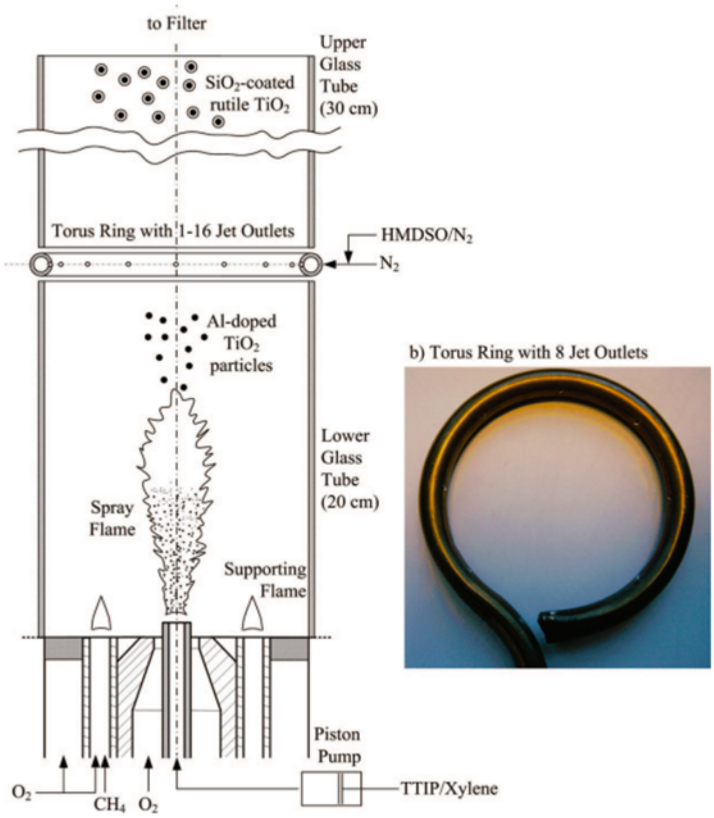

Figure 1.18. Flame assisted reactor of synthesizing silica-coated particles by using torus ring with 8 jet outlets for introducing HMDSO as the silica source. Adapted from [70]

1.6 Challenges in synthesizing FeNi and FeNi@SiO$_2$ particles via gas phase method for powder core inductor

1.6.1 One-step synthesis of submicron-sized FeNi and FeNi@SiO$_2$ particles

The gas phase method of synthesizing submicron-sized FeNi and FeNi@SiO$_2$ particles is a complex process that involves several challenges. Among gas phase methods, spray pyrolysis has provided an excellent reduction atmosphere. Typically, to get a pure FeNi alloy from its metal salt using this method needs reduction gas such as H_2 gas. Therefore, an alternative reduction agent which is safe and cost effective is required. Some researchers have employed ethanol, ethylene glycol, or formic acid to produce a pure metal particle such as Ni, Ag and Cu. Regarding the synthesis of pure Fe particles, it requires high reduction atmosphere. However, when the high concentration of ethanol is applied to replace the use of 100% H_2 gas, the formation of FeC and carbon nanoparticles are occurred owing to the catalytic performance of Fe particles in resulting carbon [71]. So far, there is no study that successfully produce FeNi particles by applying some alternative reduction agents. In addition, to obtain FeNi@SiO$_2$ particles in a direct process via gas phase method, the FeNi source and the SiO$_2$ source must be introduced in appropriate condition. It is required that the FeNi source is in a solid state and the SiO_2 source in a vapor state and an intense mixing between both sources. Thus, some development in setting up the spray pyrolysis equipment is necessary such as adding the heating system for providing a solid core particle as well as determining a tool for introducing the vapor of SiO_2 source. The coating process can be proceeded by heterogeneous nucleation and the scavenging of the SiO_2 clusters on the FeNi particles which is dependent on the temperature, the precursor concentration, and the mixing performance between precursors.

1.6.2 Computational Fluid Dynamic for silica-coated particles synthesized via the aerosol route

Computational fluid dynamics (CFD) plays a crucial role in understanding the behavior of silica-coated particles synthesized via the aerosol route. The aerosol route involves the production of fine particles suspended in a gas medium, making it essential to analyze the fluid dynamics governing their deposition and coating processes. By utilizing CFD models, the complex interactions between the aerosol particles and the surrounding gas phase can be accurately captured. The CFD simulations help in understanding the transport phenomena, such as particle dispersion, diffusion, and advection, which influence the particle deposition and coating [69,72]. The fluid flow patterns, including velocity profiles, turbulence, and pressure gradients, are analyzed to identify regions of particle aggregation and deposition. Moreover, CFD simulations aid in predicting the particle trajectory and residence time within the aerosol reactor. This information is vital for determining the optimal conditions for achieving uniform coating thickness and preventing nanoparticle generation. Additionally, CFD models assist in studying the heat and mass transfer phenomena during the coating process. By considering the thermal and chemical properties of the gas phase and the particles, researchers can evaluate the temperature distribution, reaction rates, and species concentration profiles. These insights contribute to controlling the growth kinetics and the quality of the silica coating.

To perform the momentum transport in the CFD simulation, there are several models that can be applied depend on the specific class of problem, level of accuracy, the amount of time available for the simulation. There are two common approximations which provides reasonable prediction for the fluid mechanics calculation. First, The Reynolds-averaged Navier-Stokes (RANS) equations govern the transport of the averaged flow quantities, with the whole range of the scales of turbulence being modeled. The RANS-based modeling approach therefore greatly reduces the required computational effort and resources. An entire hierarchy of closure models are available in ANSYS FLUENT software including Spalart-Allmaras, k-ε and its variants, k-ω and its variants, and the Reynold Stress Model. The RANS equations are often used to compute time-dependent flows, whose unsteadiness may be externally imposed (e.g., time-dependent boundary conditions or sources) or self-sustained (e.g., vortex-shedding, flow instabilities). Second, Large Eddy Simulation (LES) provides an alternative approach in which large eddies are explicitly computed (resolved) in a time-dependent simulation using the "filtered" Navier-Stokes equations. The rationale behind LES is that by modeling less of turbulence (and resolving more), the error introduced by turbulence modeling can be reduced. Although the LES has specialty to give a good prediction in unsteady calculation, it must be noted that this model requires more expensive calculation. Regarding the energy equation in CFD, it is estimated by following Eq. (1.7).

$$\frac{\partial}{\partial t}(\rho E) + \nabla.(\vec{v}(\rho E + p)) = \nabla.(k_{eff}\nabla T - \sum_j h_j\vec{J}_j + (\bar{\bar{\tau}}_{eff}.\vec{v})) + S_h \qquad (1.7)$$

where k_{eff} is the effective conductivity (k+kt, where kt is the turbulent thermal conductivity, defined according to the turbulence model being used), and $\vec{J}_j$ is the diffusion flux of species j. The first three terms on the right-hand side of Eq. (1.7) represent energy transfer due to conduction, species diffusion, and viscous dissipation, respectively. S_h includes the heat of chemical reaction, and any other volumetric heat sources you have defined. For the determination of the particle's simulation, there are two approaches for the numerical calculation of multiphase flows: the Euler-Lagrange approach and the Euler-Euler approach. Since the system for synthesizing FeNi and FeNi@SiO_2 particles involves the particles that is highly dispersed to a fluid volume of the primary phase, the Euler-Lagrange approach can be chosen. In this model, the fluid phase is treated as a continuum by solving the Navier-Stokes equations, while the dispersed phase is solved by tracking a large number of particles, bubbles, or droplets through the calculated flow field. The dispersed phase can exchange momentum, mass, and energy with the fluid phase [73].

1.7 Objective and Outline of the dissertation

Keeping in mind the urgency of the sustainability, we aimed to synthesis particles for the advancement of powder core inductor by dealing with the following considerations:

1. A one-step and harmless process
2. Particles with high packing density
3. Particles with high magnetic characteristic
4. Particles with high DC bias characteristic

5. Particles with low core loss

Therefore, in this dissertation, we prepared spherical and submicron-sized FeNi and FeNi@SiO$_2$ particles via spray pyrolysis method. Firstly, the spherical and submicron-sized FeNi particles by applying alternative reduction agents to achieve the first objectivity. Secondly, the optimization of the experimental condition to obtain the particles with high density and magnetic characteristic. Finally, synthesizing the FeNi@SiO$_2$ particles with high coating performance to reduce the core loss of a powder core. This dissertation is divided into five chapters, the content of which is briefly described below.

Chapter 1 elaborated the motivation and background of the development of soft-magnetic particles for the inductor, including the recent trends, basic theoretical explanation, several synthetic strategies to synthesize silica-coated particles with the desired structure, and the numerical approach in synthesizing silica-coated particles.

Chapter 2 focused on the selection of a reduction agent to synthesis FeNi particle via spray pyrolysis method. The morphology, structure, and the crystal structure of the FeNi particles from the use of ethanol, ethylene glycol, and formic acid as a reduction agent with various concentration were compared. The most prominent reduction agent is determined by the most effective reduction agent in yielding the spherical and submicron-sized FeNi particles with dense structure.

Since a powder core inductor needs submicron-sized FeNi particles with high density, **Chapter 3** aimed to control the structure and density of the FeNi particles from hollow (low density) to dense (high density) by manipulating the reactor temperature and the carrier gas flow rate. The increasing the reactor temperature and decreasing carrier gas flow rate resulted in the FeNi particles with dense structure and high density. To prevent the formation of unfavored carbon impurity, the performance analysis of the FeNi particles in a powder core application was focused on the temperature of 1200°C and the carrier gas flow rate between 5 and 1.3 L/min. This investigation revealed that the suppression of the hollow structured FeNi particles could enhanced the DC bias characteristic of a powder core inductor with improvement on the saturation current value.

Chapter 4 attempted a direct synthesis of the FeNi@SiO$_2$ particles via spray pyrolysis in various equipment design, i.e. T-shaped and swirler types, to introduce the Hexamethyldisiloxane (HMDSO) as a silica source onto the FeNi aerosol. The CFD simulation was conducted to perform a mixing performance between the HMDSO and FeNi aerosol. The coating ratio and the level of formation of undesired nanoparticles attributed to the free silica were calculated through TEM analysis images by comparing the connector types. Furthermore, the performance of $FeNi@SiO_2$ particles was compared to that of FeNi particles. It is projected that the use of $FeNi@SiO_2$ particles in an inductor result in significantly higher saturation current values and lower current loss than the use of FeNi particles.

Chapter 5 summarizes the general conclusions of all chapters and the future development of this research.

Chapter 2

Direct synthesis of submicron FeNi particles via spray pyrolysis using various reduction agents

Abstract

Preparing spherical and submicron FeNi particles in a simple, rapid, and harmless process is highly desirable for various applications yet severely challenging. Herein, we successfully synthesized the FeNi particles from their metal salts in a relatively low reduction atmosphere using three types of reduction agent, i.e., ethanol, ethylene glycol, and formic acid, via spray pyrolysis. The reduction agents were tested over a concentration range of 0–30 vol%. The type and concentration of reduction agents show a crucial role in the formation of FeNi particles. At higher concentrations (25 vol%), ethanol and ethylene glycol produced smooth and spherical FeNi particles of submicron size, 284 ± 1.6 and 399 ± 1.5 nm respectively, whereas formic acid produced particles with an irregular and Janus shape comprising FeNi and FeO, with a size of 396 ± 1.5 nm. A plausible metal salt reduction mechanism was proposed for the different reduction agents. The reduction agent type not only influences the reduction degree but also particle morphology during synthesis. This finding opens new opportunities to adjust the FeNi particles with respect to varied purposes by manipulating reduction agents.

Published in part in Advanced powder technology 32, 11, 4263 – 427

2.1 Introduction

Permalloy particle is an iron and nickel alloy (FeNi) particle that is used extensively in the production of inductors, transformers, catalysts, and biomedical applications because of its high magnetic density and low coercivity properties [74–76]. Magnetic properties are generally influenced by particle morphology[77], size, crystallinity, and purity [78]. In terms of particle morphology, spherical shape provides superior packing density in comparison to irregular shape. Moreover, since this shape does not have sharp edges, it is less prone to damage other materials [79–81]. Regarding the particle size, it is also important because it has strong influence on their magnetic behavior in external magnetic fields [82]. So far, the advantage of magnetic nanoparticles (below 100 nm) has begun to be considered by a few commercial manufacturers, but in fact, there are still practical problems in handling processes [83] and maintenance costs [84]. Based on this background, recently, size controllable spherical particle in hundreds nanometer (submicron-sized) is more desirable from an industrial perspective than irregular and micro/nano-meter size.

FeNi particles have been produced by liquid phase methods (e.g., chemical solution [38], hydrothermal [42]), solid phase methods (*e.g.*, mechanical milling [33][33]), and gas phase methods (*e.g.*, vapor deposition [46], gas condensation technique [47], hydrogen plasma-metal reaction [85], spray pyrolysis [49,52]). Spray pyrolysis is one such method, recognized as an effective strategy for producing submicron sized particles with a smooth surface and spherical shape in a one-step process at large scales [86–88]. The method comprises droplet generation, solvent evaporation, and reaction to product. It allows for easy control of particle size and morphology, e.g., making spherical, dense, hairy, porous, or hollow particles in nanometer to micrometer sizes [81,89,90]. To date, spray pyrolysis has been successfully used to synthesize CuS [91], Ni [92], Cu [93,94], Ag [88], and AgCu [95] metal submicron particles that are spherical. However, its application to the synthesis of the FeNi particles has been limited.

FeNi particles have been fabricated using an iron-nickel chloride solution in a 100% H_2 atmosphere via spray pyrolysis, which yielded smooth and spherical submicron particles (having an average diameter between 400 and 500 nm) [52]. However, using an atmosphere of 100% H_2 gas as the reduction agent is a safety issue. Methoxyethanol has been demonstrated as a safer route for the synthesis of FeNi particles [18]. Here, nickelocene and ferrocene are used as raw materials in a 100% N_2 atmosphere. The drawbacks of this process included (i) wide particle size distribution, (ii) some relic structures with rough surfaces, and (iii) relatively expensive precursor materials. Therefore, the synthesis of FeNi particles via this route should be adjusted to improve its effectiveness, potentially by considering the other solvents as the reduction agent.

Ethanol, ethylene glycol, and formic acid are economical reduction agents that have not been investigated with respect to FeNi particle production via spray pyrolysis. Therefore, this paper investigates the effect of those reduction agents and their concentration on FeNi particle morphology and composition. This is the first investigation that focuses on the role of reduction agents in the production of submicron FeNi particles using spray pyrolysis.

2.2 Material and methods

Figure 2.1 shows the experimental setup of the spray pyrolysis system used for synthesizing FeNi particles. The precursor solution was prepared by mixing $Fe(NO_3)_3.9H_2O$ and $Ni(NO_3)_2.6H_2O$ (FUJIFILM Wako Pure Chemical Corporation, Osaka, Japan), so that the total concentration was 0.1 mol/L with a molar ratio of 1:1 in ultrapure water both with and without the reduction agent. The reduction agent sources were 98% formic acid (Kanto Chemical Co., Inc., Tokyo, Japan), 99.8% ethanol (Japan Alcohol Corporation, Tokyo, Japan), and 99% ethylene glycol (Sigma-Aldrich, Tokyo, Japan). The solution droplets were generated using an ultrasonic nebulizer at 40°C (1.7 MHz, NE-U17, Omron Healthcare Co., Ltd., Kyoto, Japan) and were transferred by a carrier gas (5%-H_2/Ar) into a horizontal tubular reactor with a length of 1280 mm and inner diameter of 20 mm. The reactor was maintained at a constant temperature of 1200°C by five electrical tubular furnaces. The temperature distribution in the reactor was measured and is illustrated in **Figure A.S1** (Supporting Information).

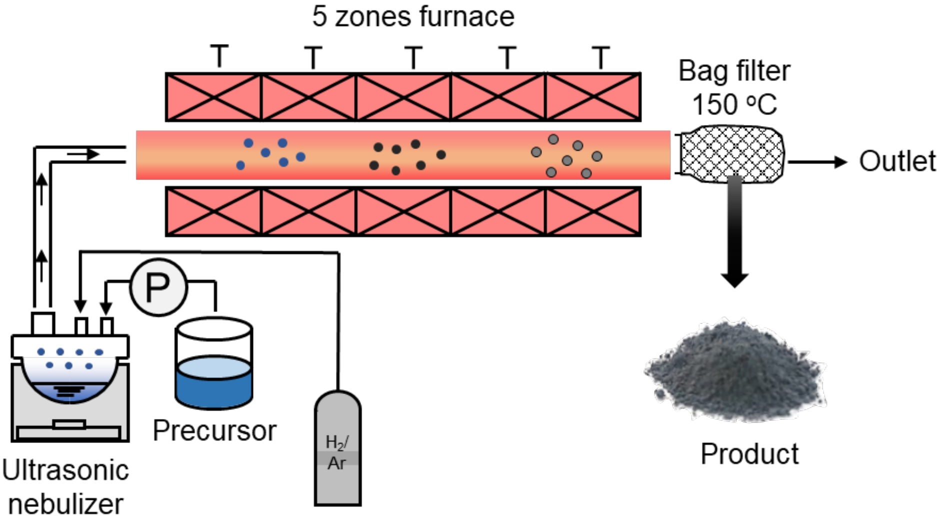

Figure 2.1. Experimental setup of spray pyrolysis system used to synthesize FeNi particles.

The carrier gas flow rate was 5 L/min. The residence time of the precursor droplets in the reactor was 4.9 s; assuming the droplets and carrier gas have the same velocity. The product was collected in a bag filter that was kept at 150°C to prevent water condensation. Pre-treatment and post-treatment steps in the reactor were performed by flowing N_2 gas at 5 L/min for 20 min to remove oxygen from the reactor. The solvent-reduction agent conditions used to produce the FeNi particles are given in **Table 2.1**. The impact of temperature changes on FeNi particle synthesis was investigated to determine the optimum operating temperature; the experimental conditions and the results are summarized in **Table A.S1** and **Figure A.S2** (Supporting Information), respectively.

Table 2.1. Experimental conditions used to synthesize FeNi particles by different reducing agents**.**

Sample name	Solvent-Reduction agent	Reduction agent concentration (vol%)
ET10	Water-Ethanol (ET)	10
ET15		15
ET25		25
ET30		30
FA10	Water-Formic Acid (FA)	10
FA15		15
FA25		25
FA30		30
EG10	Water-Ethylene Glycol (EG)	10
EG15		15
EG25		25
EG30		30

The morphology and structure of the particles were observed using field emission scanning electron microscopy (FE-SEM; S-5200, 20 kV, Hitachi High-Tech. Corp., Tokyo, Japan) and transmission electron microscopy (TEM; JEM-2010, 200 kV, JEOL Ltd., Tokyo, Japan). The crystal structure was determined using X-ray diffraction (XRD; D2 PHASER, Bruker Corp., Billerica, MA, USA). Quantitative analysis for measuring the mass fraction of the crystalline phases was performed by Rietveld analysis using TOPAS software [96]. The atomic distribution of the particles was examined using energy dispersive X-ray spectroscopy

(EDS) equipped with FE-SEM. Thermogravimetric analysis (TGA) was conducted using a TGA instrument (TGA-50/51 Shimadzu Corp., Kyoto, Japan) by applying a 50 mL/min flow of 5% H_2-N_2 at a heating rate of 10°C/min. To support the proposed mechanism of FeNi particle formation, the reduction agent decomposition simulation based on fluid dynamics was performed using Ansys Fluent software embedded in workbench 2021 R1. The simulation details are given in the Supporting Information.

2.3 Results and Discussion

2.3.1 Effect of reduction agent types on the FeNi particle synthesis

Figure 2.2(a) shows the crystal structure of FeNi particles synthesized by the three different reduction agents, i.e., ethanol, ethylene glycol, formic acid, at a concentration of 25 vol%. Three main diffraction peaks centered at 2θ values of approximately 43.9°, 50.9°, 74.8° appear in the patterns of all particles, which are attributed to diffraction from the crystal planes of face centered cubic (*fcc*) FeNi (JCPDS No. 47-1405). However, when using formic acid, FeO ($Fe_{1-x}O$ and Fe_3O_4) phases were also seen in the XRD patterns. This is explained by the different reduction agents having different H_2 conversions as follows.

Ethanol with steam [97]:

$$C_2H_5OH + 3\ H_2O \rightarrow 2\ CO_2 + 6\ H_2 \qquad (2.1)$$

Ethylene glycol with steam [98]:

$$C_2H_4(OH)_2 + 2\ H_2O \rightarrow 2\ CO_2 + 5\ H_2 \qquad (2.2)$$

Formic acid thermal decomposition [99]:

$$HCOOH \rightarrow H_2 + CO_2 \qquad (2.3)$$

Stoichiometrically, ethanol and ethylene glycol have more hydrogen than formic acid. Assuming that the reactions shown in equation (2.1), (2.2), and (2.3) were completed, the theoretical volume concentration of hydrogen gas (based on the total hydrogen gas/carrier gas vol/vol) with 25 vol% of ethanol, ethylene glycol, and formic acid were 10.7, 10.0, and 6.5 vol%, respectively.

The influence of reduction agent concentration on the crystal structure of FeNi particles is described by the XRD patterns in **Figure A.S3** (Supporting Information). Rietveld analysis on the XRD patterns is used to determine the mass fraction of components in the synthesized FeNi product, the results are summarized in **Figure 2.2(b)**. The generated particles were less than 10 wt% FeNi in the absence of a reduction agent. This mass fraction increased significantly with the addition of reduction agents. An ethanol concentration of 10 vol%

increased the mass fraction of FeNi to approximately 90 wt%, which is much higher than ethylene glycol (64 wt%) and formic acid (56 wt%) at the same concentration. When the reduction agent concentration was increased to 15 vol%, the mass fraction of FeNi in the presence of ethanol and ethylene glycol increased, but there was little change with the increase in formic acid. Above a reduction agent concentration of 15 vol%, the metal salt precursor is completely reduced to FeNi in the presence of ethanol and ethylene glycol. Conversely, the conversion of FeNi particles is still low for formic acid at approximately 60 wt%.

The conversion of FeNi is related to the H_2 gas generated by the reduction agents, and this is shown in **Figure 2.2(c)**. The slope of the ethanol and ethylene glycol curves indicates the generated H_2 gas increases sharply with reduction agent concentration. Inversely, a shallow slope of H_2 gas production is observed when formic acid concentration increases. Consequently, FeNi formation does not proceed significantly, which results in iron oxide (Fe_3O_4 and $Fe_{1-x}O$) formation. A similar result was also obtained for the synthesis of Ni particles from Ni salt reduction via spray pyrolysis [100]. That study found increasing the formic acid from 2 mol/L to 10 mol/L (proportionally more than 30 vol% in this current study) could not reduce the Ni metal without the formation of NiO from the $Ni(NO_3)_2.6H_2O$ precursor. Additionally, the presence of 10 vol% ethylene glycol specifically showed similar conversion of FeNi to that of the formic acid cases. It could be explained that a particular concentration of the generated H_2 as a minimum concentration was required for completing the metal salt reduction via spray pyrolysis. The generated H_2 gas was 7.0 vol% in the presence of 10 vol% ethylene glycol, while the generated H_2 gas was 5.6 up to 6.8 vol% in the presence of formic acid (10 – 30 vol%). These concentrations were found to be insufficient for converting the metal salt into FeNi metal effectively.

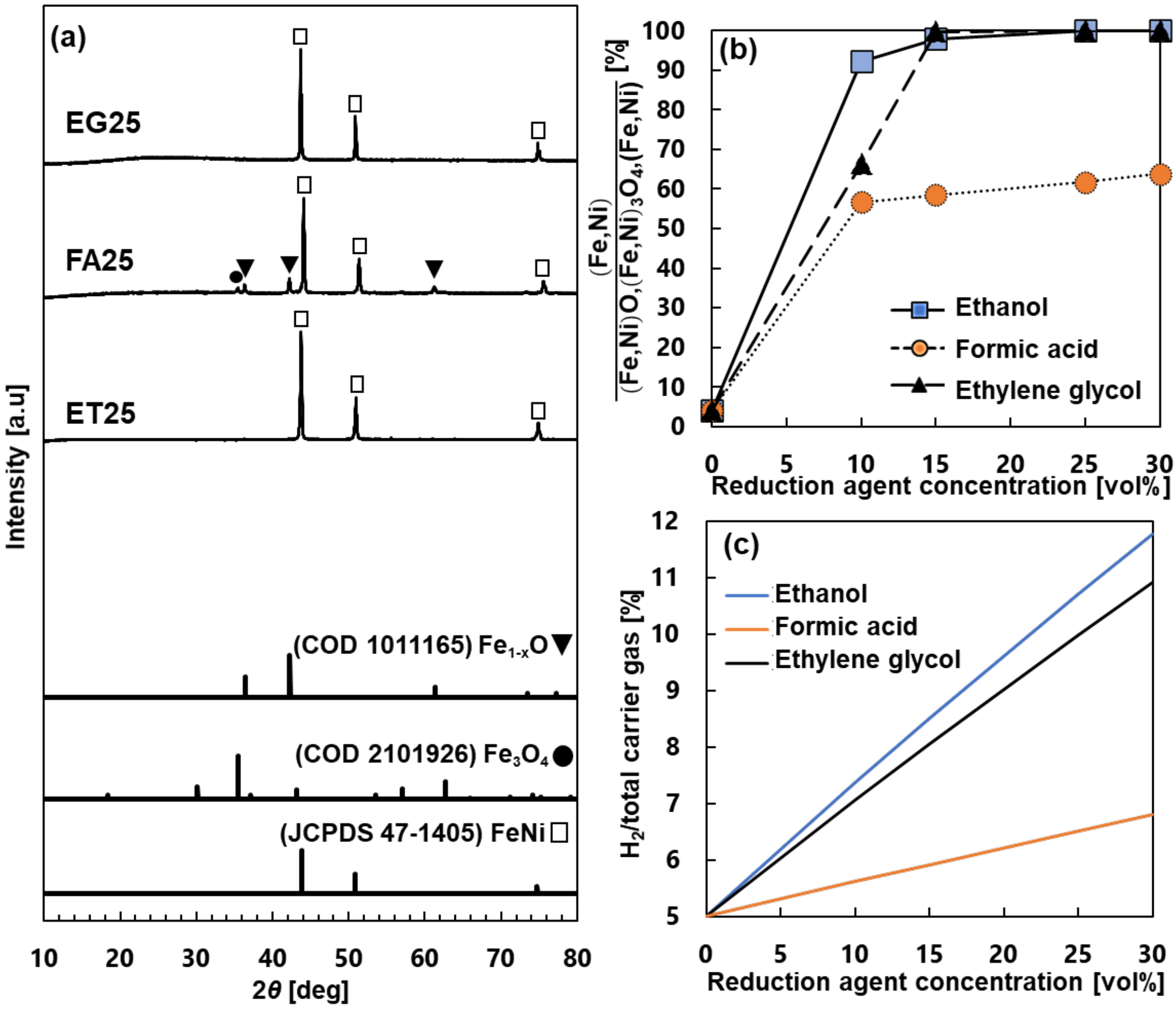

Figure 2.2. (a) XRD patterns of FeNi particles, (b) weight percentage of FeNi particles at different reduction agent concentration derived from Rietveld analysis, and (c) calculated H_2 gas concentration.

Figure 2.3 describes the effect of the different reduction agents and their concentration on particle morphology and size using SEM. **Figure 2.3(a-1), (a-2), (b-1), (b-2), (c-1),** and **(c-2)** shows that non-spherical particles with a heterostructure were generated when 10 vol% of the reduction agent was used (ET10, EG10, FA10). This result is supported by the experiment performed in the absence of any reduction agent, shown in **Figure A.S4(d)** (Supporting Information). When the concentration is increased to 15 vol%, smoother and more spherical particles with a few heterostructures were obtained when using ethanol (ET15) and ethylene glycol (EG15), illustrated in **Figure 2.3(a-3), (a-4), (c-3), and (c-4)**. Further increases of ethanol and ethylene glycol concentration (ET25 and EG25) continued this trend with smoother and more spherical particles without the heterostructure, see **Figure 2.3(a-5), (a-6), (c-5), and (c-6)**. However, 30 vol% of ethanol resulted in fine particle formation, which may be attributed to carbon formation (pointed to with yellow arrows) shown in **Figure 2.3(a-7) and (a-8)**.

Excess ethanol concentration (30 vol%) could be converted to carbon because of the FeNi particles acting as a catalyst at the high temperature [101].

For ethylene glycol, smooth and spherical particles could be obtained at a concentration of 25 and 30 vol% (**Figure 2.3(c-5)–(c-8)**), but the synthesis process at higher ethylene glycol concentrations has a lower production rate because of its high boiling point (197°C) compared with that of ethanol (78°C). Particularly, in the 25 vol% of reduction agent, the production rate of the ethanol case was 0.26 gram/h, while the ethylene glycol case was 0.11 gram/h. The production rate is defined by the synthesized FeNi particle over synthesizing time in one-time production. Contrarily, even at increasing the formic acid concentration until 30 vol% (FA15 to FA30) in **Figure 2.3(b-3)–(b-8)**, the produced particles were still irregularly shaped with a heterostructure, though the particle surface was smoother. This might be caused by the adsorption of formic acid onto metal surface before it decomposed [102].

The reduction effect on the particle size distribution which was shown quantitively in **Figure A.S5** (Supporting Information) revealed that the geometric mean diameter of the FeNi particles in the presence of ethanol, formic acid, ethylene glycol and only water were 284 ± 1.6 nm, 396 ± 1.5 nm, 399 ± 1.5 nm, 444 ± 2.1 nm, respectively. It is believed that the surface tension property of the precursor mentioned in **Table A.S2** (Supporting Information) had a significant impact [103].

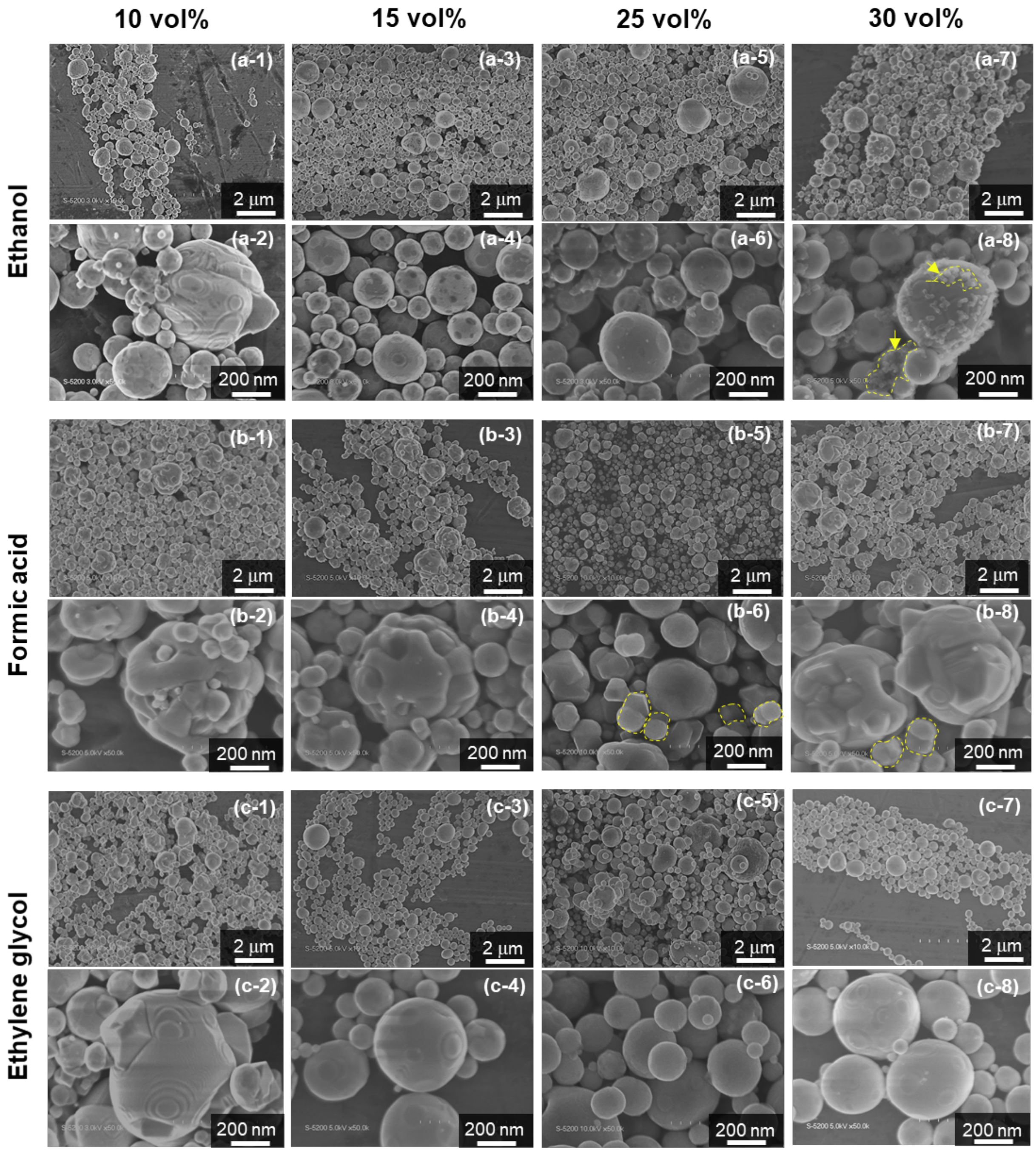

Figure 2.3. SEM images of the FeNi particles produced at various concentration of the reduction agents (a) ethanol, (b) formic acid, and (c) ethylene glycol.

The heterostructure formation is attributed to the segregation phase in the particles. According to elemental mapping of particles formed in 25 vol% formic acid (**Figure 2.4(a)**), the distribution of the Fe atoms can be seen on the whole surface of the particles homogeneously whereas the Ni and O atoms are distributed separately. This is evidence of segregation between FeO and FeNi phases in the particles, which is also confirmed by the XRD pattern in **Figure 2.2(a)**. Moreover, element mapping for the FeNi particles prepared in 25 vol% ethanol also reveals homogeneous Fe and Ni atoms on the surface of the particles with inconsiderable amount of oxygen (**Figure 2.4(b)**). This indicates that FeNi particles were successfully produced.

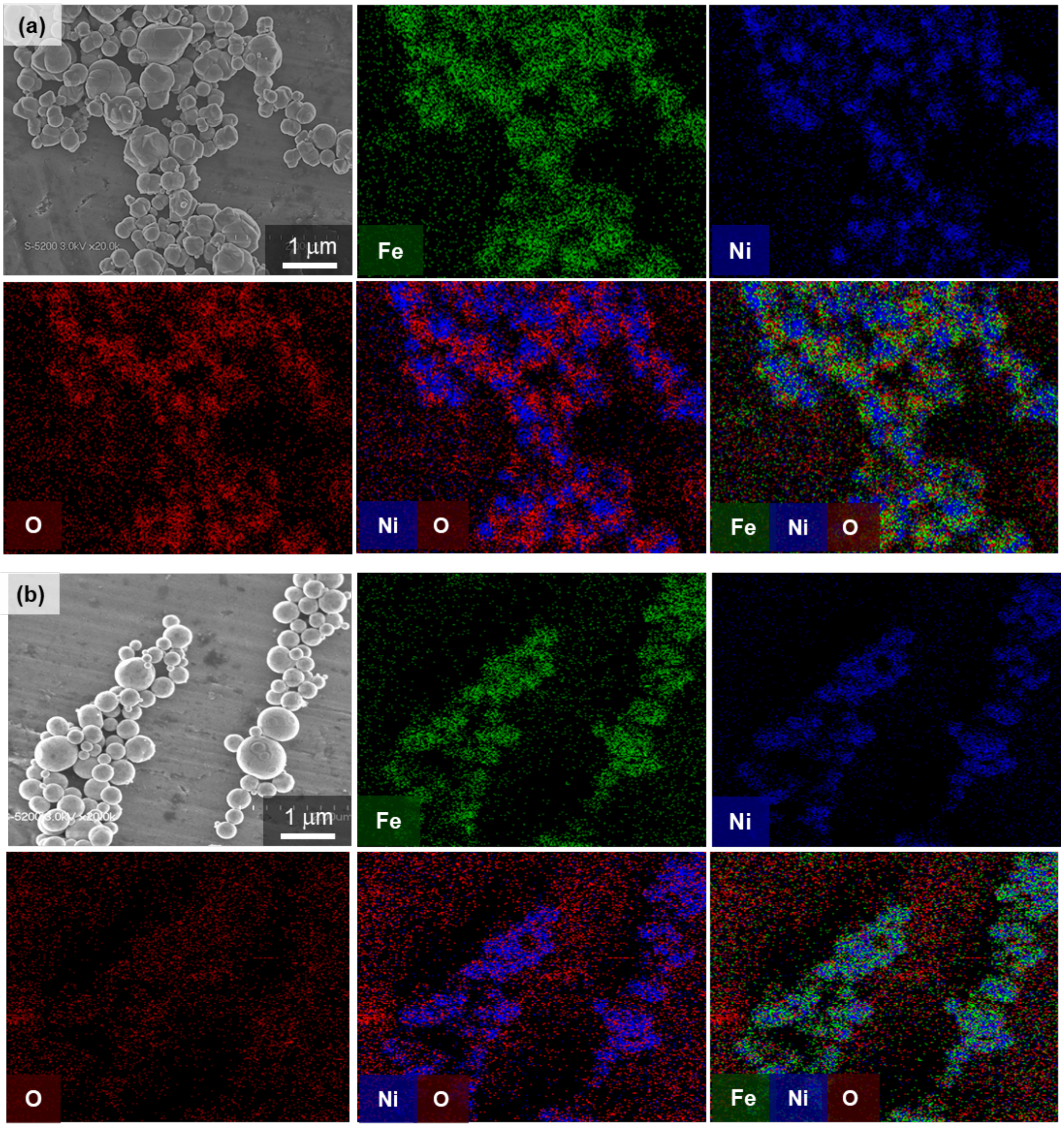

Figure 2.4. Elemental mapping of the particles produced in (a) formic acid (FA25), and (b) ethanol (ET25).

Figure 2.5 displays the TEM images of the particles produced in 25 vol% of the reduction agents. The using of ethanol and ethylene glycol in **Figure 2.5(a)** and **(c)** show spherical particles of submicron size. However, particles produced in ethylene glycol exhibit a substantial amount of hollow structure. Comparatively, the irregular shape and Janus particles are obtained when using formic acid (**Figure 2.5(b)**). To determine the metal phases in the interior of the particles, EDS analysis was used and the results are shown in **Figure A.S6**. Based on the Janus particles when using of formic acid, the FeO phase is indicated at position (1) in the grey area, while the FeNi phase is indicated at the position (2) in the black area.

Conversely, position (3) in the particles generated in ethanol show Fe and Ni elements only. The EDS analysis of particles produced in 25 vol% of formic acid supports the elemental mapping shown in **Figure 2.4**.

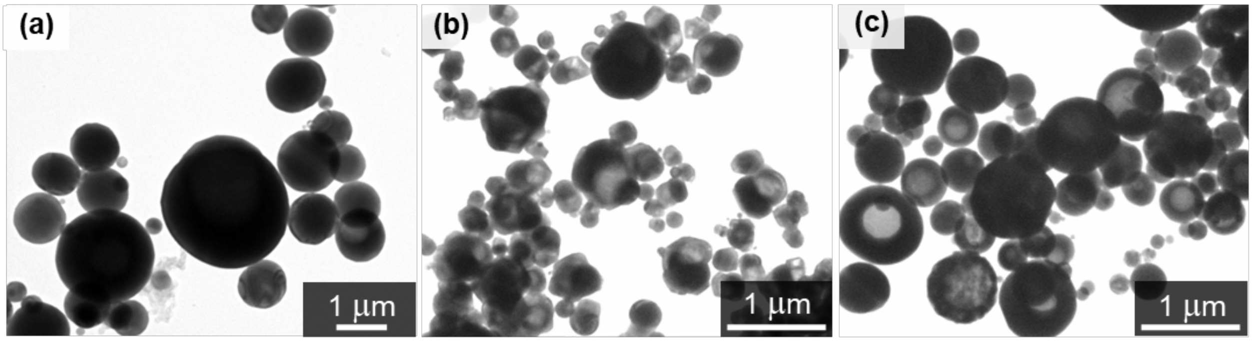

Figure 2.5. TEM images of FeNi particles synthesized using 25 vol% reduction agents: (a) Ethanol (ET25), (b) Formic acid (FA25), (c) Ethylene glycol (EG25).

Based on crystal structure and morphology analysis, the concentration and type of reduction agent greatly affects metal alloy particle production. When using 25 vol% ethanol (ET25) and ethylene glycol (EG25), smooth, spherical, and submicron sized FeNi particles have been successfully fabricated via spray pyrolysis for the first time, to our best knowledge. Smooth and spherical particles are preferable because they provide greater packing density. These results are compared with previous work regarding FeNi particle synthesis in **Table 2.2(a), (b),** and **(d)**.

Our proposed method not only produces FeNi particles with the preferred surface, but also overcomes problems of FeNi particle synthesis with respect to the harmful and costly 100% H_2 gas process and its accompanying safety concerns. Moreover, this method shows the superiority in the synthesis of FeNi particles by conducting lower H_2 gas content. Using a lower concentration of H_2 gas (10 vol%) at a high temperature (1400°C) in **Table 2.2(e)**, resulted in $FeNi_3$ particles being formed [104]. However, this condition should yield FeNi particles thermodynamically [105]. This previous study implied that the presence of iron salt in the precursor impedes the reduction mechanism. This is supported by previous results when using ethanol (**Table 2.2(f)** and **(j)**). Numerous successful studies on nickel rather than iron generated from metal salts indicates that the nickel particle synthesis is more straightforward than iron particle synthesis. Overall, our results are in general agreement with the particle characteristics in previous studies of metal synthesis from iron and nickel salt reduction by spray pyrolysis using ethanol and formic acid (**Table 2.2 (a)–(i)**).

Table 2.2. Comparison between present work and previous work regarding the synthesis of FeNi, Ni, Fe based particles from metal salt precursors via spray pyrolysis.

	Precursors	Product	Reduction agent type and concentration	Carrier gas flow rate	Temperature (°C)	Particle characteristics	Ref.
a.	0.1 mol/L $Fe(NO_3)_3.9H_2O$ $Ni(NO_3)_2.6H_2O$	FeNi	Ethanol 25 vol%	5 L/min 5%H_2-Ar	1200	Smooth surface, hollow, spherical and submicron alloy particle	This work
b.	0.1 mol/L $Fe(NO_3)_3.9H_2O$ $Ni(NO_3)_2.6H_2O$	FeNi	Ethylene glycol 25-30 vol%	5 L/min 5%H_2-Ar	1200	Smooth surface, hollow, spherical and submicron alloy particle	This work
c.	0.1 mol/L $Fe(NO_3)_3.9H_2O$ $Ni(NO_3)_2.6H_2O$	FeNi FeO	Formic acid 30 vol%	5 L/min 5%H_2-Ar	1200	Rough surface and submicron heterostructure particle	This work
d.	0.05 – 0.4 mol/L $FeCl_2.4H_2O$ $NiCl_2.6H_2O$	FeNi	H_2 100 vol%	1 L/min H_2	900	Spherical, dense, and submicron particle with smooth and rough surface	[52]
e.	0.02 – 1 mol/L $Fe(NO_3)_3.9H_2O$ $Ni(NO_3)_2.6H_2O$	$FeNi_3$	H_2 10 vol%	20 L/min H_2-N_2	1400	Smooth surface, dense, spherical and submicron particle	[104]
f.	0.1 mol/L $Ni(NO_3)_2.6H_2O$	Ni	Ethanol 3.4 mol/L (20 vol%)	10 L/min Ar	700	Rough surface, hollow, and submicron particle	[106]
g.	0.75 mol/L $Ni(NO_3)_2.6H_2O$	Ni NiO	Formic acid 10 mol/L (37.5 vol%)	2 L/min 10% H_2-N_2	1100	Nanoparticles of metal and metal oxide	[100]
h.	0.11 mol/L $Ni(CH_3COO)_2.4H_2O$	Ni	Formic acid 6 mol/L (23 vol%)	20 L/min N_2	1000	Smooth surface, dense, spherical and submicron particle	[107]
i.	1 mol/L $Ni(NO_3)_2.6H_2O$	Ni	Formic acid 15 mol/L (56 vol%)	20 L/min N_2	1000	Smooth surface, hollow, spherical and submicron particle	[107]
j.	0.05 – 0.4 mol/L $Fe(NO_3)_3.9H_2O$	FeO@FeC	Ethanol 72 vol%	7 L/min N_2	820	Core shell, spherical, dense, and submicron particle with smooth surface	[71]

2.3.2 Proposed mechanism of FeNi particles.

The mechanism of FeNi particle formation via spray pyrolysis is proposed in this section based on crystallite structure and morphology. **Figure 2.6** illustrates the formation of the metal salt droplet into a solid FeNi particle in 25 vol% of the three reduction agents at the temperature of 1200°C. According to the TGA and ethanol decomposition fluid dynamics simulation results (see **Figure A.S7** and **Figure A.S9** in the Supporting Information), the mechanism takes place in two stages: (i) solvent evaporation and precursor chemical reaction following equation (2.4) and (2.5) [108,109]; and (ii) reduction of the iron nickel oxide (FeNiO) to FeNi particles (equations (2.6) to (2.8)) [110].

$$Fe(NO_3)_3.9H_2O \rightarrow Fe(OH)_2.NO3 + H_2O + HNO_3 \rightarrow Fe_2O_3 + NO_2 + O_2 + H_2O \quad (2.4)$$

$$Ni(NO_3)_2.6H_2O \rightarrow Ni(OH).NO_3 + H_2O + HNO_3 \rightarrow NiO + NO_2 + O_2 + H_2O \quad (2.5)$$

$$Fe_2O_3 + NiO \rightarrow Ni_xFe_{3-x}O_4 \quad (2.6)$$

$$Fe_2O_3 \rightarrow Fe_3O_4 \quad (2.7)$$

$$Ni_xFe_{3-x}O_4 \rightarrow NiO + Fe_3O_4 \rightarrow Ni + Fe_3O_4 \rightarrow Fe_{1-x}O + FeNi \quad (2.8)$$

In the addition of 25 vol% ethanol (**Figure 2.6(a)**), spherical particles with a dense structure are formed. Because the droplet size ranges between 1 to 10 μm [37], this structure formation might result from the smaller droplet size and the densification of hollow particles formed from larger droplets resulted during the first stage. At this stage, the solvent evaporates rapidly because of the higher vapor pressure of ethanol (43 mmHg, at 20°C, CAS No. 64-17-5) compared with that of water (18 mmHg, at 20°C, CAS No. 7732-18-5), and the substantial difference of solvent boiling point. The solute from the smaller droplet can be diffused to the center, while the solute of the larger droplet concentrates near the surface without enough time to diffuse to the center during precipitation of FeNiO [111]. Subsequently, it is theorized that FeNiO solid can be reduced into FeNi at 1200°C because of the high reducing atmosphere. This temperature also causes the densification of the hollow structure particles [112].

Meanwhile, the hollow structure produced when using ethylene glycol as the reduction agent (**Figure 2.6(b)**) is caused by the vapor pressure of the ethylene glycol (0.06 mmHg at 20°C, CAS No. 107-21-1) being much lower than water and its boiling temperature (197°C) is significantly above water's. This results in a solute concentration gradient in the ethylene glycol when the water evaporates. Moreover, due to the solvent properties of relatively high surface tension resulted in larger droplet size than that of ethanol case affected to the obstacle of the densification. In particular comparison to the densification in the ethanol case, the solvent evaporation in the ethanol case was much faster than in the ethylene glycol case. As a result, the precursor's solid state was created very instantly in the ethanol case, giving it significantly more time to be reduced and densified in the spray pyrolysis reactor. The ethylene glycol case, on the other hand, the particles did not have enough time to densify completely. Additionally, the low vapor pressure of ethylene glycol may cause precursor decomposition in the liquid phase, like the polyol process during the first stage [[96]. Ethylene glycol is decomposed from the metal nitrate into metal hydroxide ($Fe(OH)_2.NO_3$ and $Ni(OH).NO_3$) during the evaporation of ethylene glycol from the droplet. This is supported by the difference in solid color during solvent evaporation at 200°C (**Figure A.S8**, Supporting Information). Following this, the reactions described in equations (4) to (8) occur at increased temperatures to generate FeNi particles.

The Janus and irregularly shaped particles produced with formic acid (**Figure 2.6(c)**) are the same as those produced by ethanol and ethylene glycol at low concentrations (10 vol%). This is explained by the hydrogen production at those concentrations being similar, i.e., 6.5% H_2/total carrier gas when using 25 vol% formic acid and approximately 7.0% H_2/total carrier gas when using 10 vol% ethanol or ethylene glycol. This shape is caused by the slow rate of reduction, which is similar to that seen in the absence of a reduction agent (explained in the Supporting Information). During the first stage, water and formic acid evaporate simultaneously followed by precipitation of FeNiO. Then FeNiO is reduced into FeNi and FeO (Fe_3O_4 and $Fe_{1-x}O$) as described by equations (6) to (8). The Janus and irregularly shaped particles are formed because of the lattice mismatch between FeNi and FeO [113]. This is likely caused by stabilized iron and oxide sites in the FeO due to oxygen vacancy. This vacancy can be filled by iron and nickel to form an FeNi alloy before it is urged to the FeO surface and incorporated by Ostwald ripening [114]. In the appearance of the oxygen vacancy, the crystal lattice among the phases can be expanded or contracted [115], which results the immiscibility between FeNi and FeO. Additionally, an exsolution might occur in the irregularly shaped particles according to the previous study of spinel-type oxides (e.g., $CuFe_2O_4$, $NiMn_2O_4$) in a reductive environment [115].

According to the simulation result, **Figure 2.7(a)** also confirms that the H_2 gas generation from the ethanol case was higher and faster than the other cases. This supports that the reduction and densification of the final product in the reactor can be performed in the ethanol case. Furthermore, **Figure 2.7(b)** shows that the water mol fraction in the formic acid case was greater than the other cases. This high water content might contribute to the obstacle of reducing process [116].

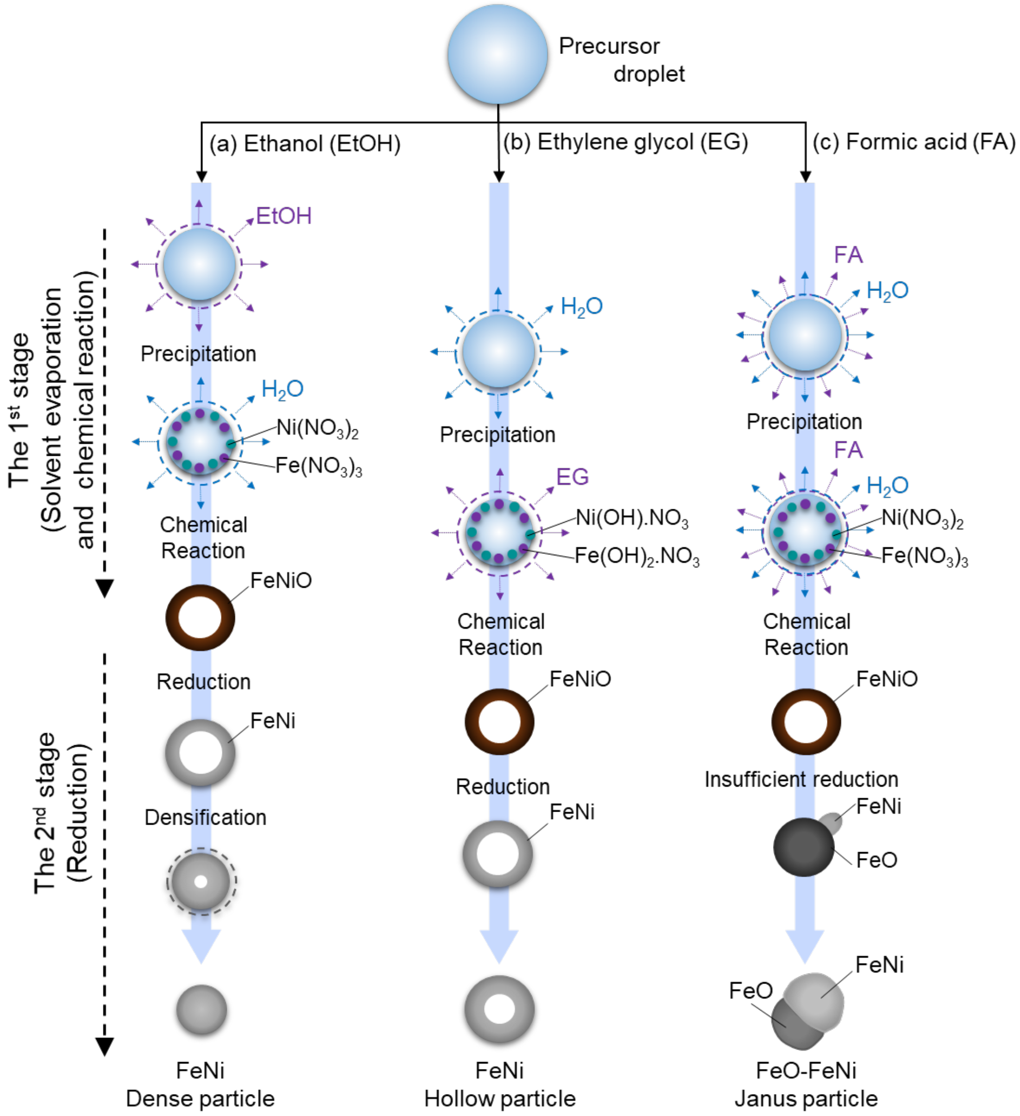

Figure 2.6. FeNi particle formation mechanism by 25 vol% of (a) ethanol, (b) ethylene glycol, and (c) formic acid at 1200°C.

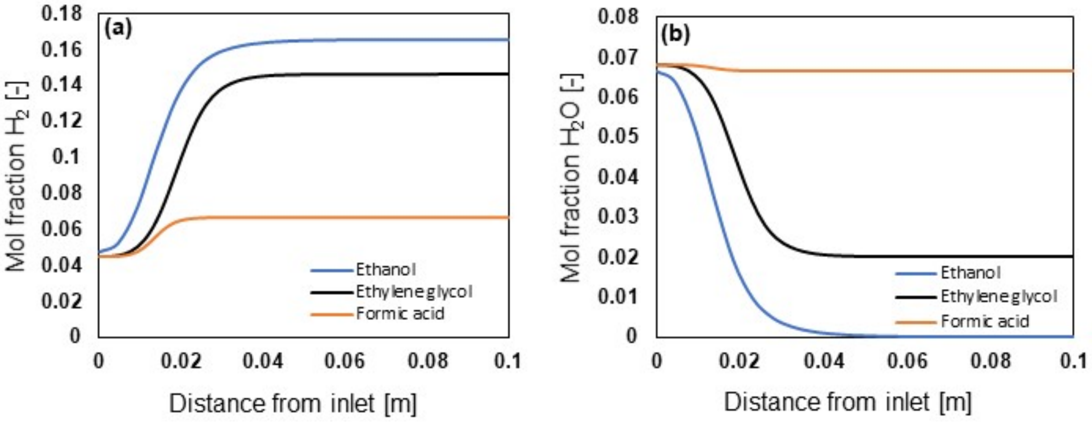

Figure 2.7. The simulation result of (a) hydrogen and (b) water composition in the spray pyrolysis reactor.

2.4 Conclusion

The manufacturing of permalloy particles in a benign and cost-effective process using spray pyrolysis was successfully demonstrated. Harmless and low-cost reduction agents, i.e., ethanol, ethylene glycol, formic acid, are employed to produce submicron particles with a FeNi crystal structure. The results show the concentration and type of reduction agent are critical parameters for reducing iron and nickel metallic salts to produce FeNi particles. The different reduction agents lead to different H_2 gas generation rates, which is required for metal salt reduction. According to the crystal structure, morphology, and the elemental analysis, ethanol and ethylene glycol promote smooth surfaced, spherical, and submicron-sized particles of FeNi. Conversely, formic acid resulted particles with segregated phases between FeNi and FeO. Generally, the higher the concentration of the reduction agent, the more benefit there is for the resulting the FeNi particles. However, at ethanol and ethylene glycol concentrations of 30 vol%, there was carbon formation and droplet production difficulty, respectively. Furthermore, a possible particle formation mechanism was proposed to better understand the metallic salt reduction of iron and nickel. The mechanism occurs in two stages: (i) evaporation and chemical reaction, (ii) reduction stages. Overall, this finding opens new possibilities for the application of FeNi particles by changing the type and concentration of the reduction agents used in their synthesis.

Acknowledgement

This work was supported by JSPS KAKENHI Grant Number 19H02500. This work is partly supported by the Center for Functional Nano Oxide at Hiroshima University, International Network on Polyoxometalate Science, JSPS Core-to-Core Program, The Information Center of Particle Technology, Japan, and Hosokawa Powder Technology Foundation. We would like to thank the Ministry of Education, Culture, Sports, Science and Technology (MEXT) of Japan for providing a doctoral scholarship to E. L. S. We thank Dr. Makoto Maeda of the Natural Science Center for Basic Research and Development (N-BARD) at Hiroshima University for TEM observations and discussion. We also thank Shaun Galbraith, PhD, from Edanz (https://jp.edanz.com/ac) for editing a draft of this manuscript.

Chapter 3

DC bias characteristic enhancement of the powder core by using densified submicron sized FeNi particles through spray pyrolysis

Abstract

The powder core type of inductor has become a promising component of a high-power DC–DC converter. The inductor consists of a powder core, a packing of primary (coarse) and secondary (fine) particles, and a winding coil. The characteristic of the secondary particles in the powder core is crucial to the inductor performance, i.e., DC bias characteristic. Here, we successfully produce high-density spherical and submicron sized FeNi particles (300 – 400 nm), which were investigated as the secondary particles for the first time. By precisely controlling the temperature and residence time of the spray pyrolysis process, the size and structure of the FeNi particles were altered owing to densification. The structural change from hollow to dense provides a stable magnetic characteristic of the FeNi particles at 1.5 T with an enhancement of the particle density from 7.38 to 8.33 g/cm^3. As a result, the as-prepared FeNi particles exhibit an excellent DC bias characteristic that is proportional to the escalating particle density. A suppression of the formation of hollow particles from 34% to 10% reveals an improvement in the saturation current (Isat) by approximately 20% from 10.2 A to 12.1 A. The densification not only enlarges the magnetic field path but also increases the adjacent non-magnetic region. The use of the dense and submicron sized spherical FeNi particles is proposed to lead to a wide application for the advancement of renewable energy generators, electric transportations, and electronic devices in industrial sectors.

Published in part in J. Mater. Chem. C, 2022,10, 8288-8295

3.1 Introduction

The inductor is a key component in the rapid evolution of electronic devices, such as electric vehicles, cell phones, and renewable power generators, to actualize sustainable development goals for smart and green technology. An inductor is widely applied to maintain the high efficiency and compact design of the devices by controlling the electric power through the components of the devices. A more minimalist design will result in a lower energy and environmental burden [117]. Therefore, improving inductor performance is important for current conversion and energy storage in electromagnetic form for those devices. From an industrial perspective, the critical points on the inductor development are focused on its high performance, low-cost productivity, and suitability for mass production. Regarding the high performance, the direct current (DC) bias characteristic is an important factor, which is affected by the magnetization characteristic and the permeability of the material [118]. The DC bias characteristic determines the capability of the inductor over the electrical current load.

In determining the inductor type which provides a compact design and excellent performance, the powder core has been frequently used because it has a well-distributed adjacent non-magnetic region in its packed structure. The distributed non-magnetic region allows the inductor to work with high inductance and saturation values [119]. The inductor consists of a powder core, a packing of primary (coarse particles) and secondary (fine particles) soft-magnetic particles, and a winding coilv[10]. The ratio between the primary and secondary soft-magnetic particles as well as the characteristic of the secondary particles are important to maximize the value of the DC bias current. These factors could be attributed to the packing behavior of the particles according to previous research. Zhang et al. noted that the addition of a percentage of micron-sized spherical Fe-Co (d_p = 14 µm) from 0% to 100% as the secondary particles into an amorphous powder enhanced the DC bias characteristic owing to the improvement of the packing density [120]. Kim et al. also reported that applying 20 wt% of the spherical carbonyl iron powder (CIP) (d_p = 3.74 µm) into an Fe-based amorphous powder has benefits in increasing the DC bias property due to the higher packing density compared with the specimen with the CIP below 20%[118]. Based on these studies, it can be concluded that the spherical particles might contribute to a good packing density[79]. Moreover, although the nanometer size of the secondary particles presents a higher magnetic saturation value [121], decreasing the size to below 100 nm results in difficulty from a handling point of view. Accordingly, spherical and submicron sized particles (100 nm – 1 μm) are highly favored as the secondary particles.

Furthermore, selecting the material of the secondary particles is also necessary to provide an excellent performance of the powder core because it determines the inductance performance of an inductor to generate an electric potential. For the powder core material, permalloy (FeNi) is considered because it exhibits relatively high magnetic saturation, high permeability, and low coercivity[45]. Imaoka et al. have evaluated the powder core made from various materials (e.g., ferrosilicon, permalloy, supermalloy, sendust, amorphous powder). This study revealed that the permalloy provides a high efficiency to the powder core performance [4]. Until now, only a few researchers have successfully produced spherical and submicron sized FeNi alloy powder [49,52,122]. Recently, our group was the first synthesizing spherical FeNi particles (dp = 300 nm) through the spray pyrolysis method by using ethanol as the reduction agent benignly and effectively. Nevertheless, the obtained FeNi particles had a hollow structure and a low particle density. These characteristics might result in a decrease of the magnetic characteristic value. Thus, improving the density of spherical FeNi particles remains a challenge.

In this research, as depicted in **Scheme 3.1**, we are investigating the production and utilization of high-density submicron sized FeNi particles as the secondary particles of a powder core for the first time via spray pyrolysis method. The alteration in the structure of the FeNi particles is expressed quantitively by the percentage of hollow particles generated and the particle density value. Furthermore, by applying the resulting FeNi particles having different particle densities, the influence of the structure of the FeNi particles on the powder core performance is evaluated. Moreover, it is demonstrated that employing a higher density of the FeNi particles enhances the saturation current (I_{sat}) value of the powder core, which indicates a higher inductor performance (DC bias characteristic). This novel approach on the application of a high density of the spherical and submicron sized FeNi particles reveals the effective performance enhancement of the powder core type inductor.

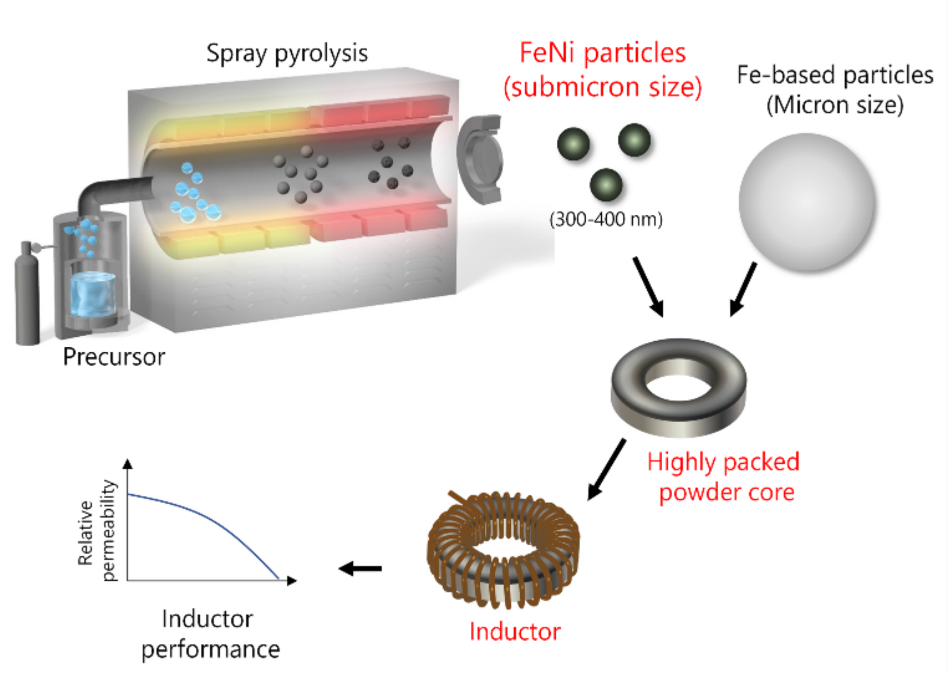

Scheme 3.1. Synthesis and investigation of submicron sized FeNi particles to the powder core performance.

3.2 Experimental

3.2.1 Materials and method

Spherical and submicron sized FeNi particles were synthesized by the spray pyrolysis method as described previously [122]. A precursor solution containing $Fe(NO_3)_3.9H_2O$ and $Ni(NO_3)_2.6H_2O$ (FUJIFILM Wako Pure Chemical Corporation, Osaka, Japan) with a concentration of 0.2 mol/L in 25 vol% ethanol (99.8% in purity, Japan Alcohol Corporation, Tokyo, Japan) and ultrapure water was prepared. This concentration was chosen by preliminary experiment, as shown in **Figures B.S1** and **B.S2**. The precursor solution was altered into droplets by an ultrasonic nebulizer at 40 °C (1.7 MHz, NE-U17, Omron Healthcare Co., Ltd., Kyoto, Japan) before being transferred into the reactor using 5% H2-Ar as the carrier gas. To control the particle structure, the applied temperature was adjusted at 1200, 1300, and 1400 °C, while the residence time was varied by changing the carrier gas flow rates (Q_c) to 5, 2.5, and 1.3 L/min, as described in **Table 3.1**. To collect the FeNi particles, a bag filter, which was maintained at 150 °C, was implemented. For making the powder core, the primary particles were Fe-Si-B type amorphous alloy powder with a magnetic saturation flux density (B_s) of 1.2 T. A press molding procedure was used to make the powder core, which had a ratio of 4:1 for the primary to secondary particles.

Table 3.1. Experimental conditions of synthesizing $Fe(NO_3)_3 \cdot 9H_2O$ and $Ni(NO_3)_2 \cdot 6H_2O$ solution in 25 vol% ethanol at various temperature and carrier gas flow rates

Sample	Precursor concentration (C_t) [mol/L]	Reactor temperature (T) [°C]	Carrier gas flow rate (Q_c) [L/min]
S12-5.0	0.2	1200	5
S12-2.5			2.5
S12-1.3			1.3
S12-1.0			1.0
S12-0.5			0.5
S13-5.0		1300	5
S13-2.5			2.5
S13-1.3			1.3
S14-5.0		1400	5
S14-2.5			2.5
S14-1.3			1.3

3.2.2 Characterization

The collected FeNi particles were characterized and continuously processed to be packed in a toroidal powder core as the secondary particles. The morphology of the FeNi particles was observed using field emission scanning electron microscopy (FE-SEM; S-5200, 20 kV, Hitachi High-Tech. Corp., Tokyo, Japan) and transmission electron microscopy (TEM; JEM-2010, 200 kV, JEOL Ltd., Tokyo, Japan). The hollow particles percentage (HP) was determined by calculating the percentage from the number of hollow particles over the total number of particles based on the TEM images as shown in **Figure B.S3**. The crystal structure was identified using X-ray diffraction (XRD; D2 PHASER, Bruker Corp., Billerica, MA, USA). Rietveld analysis by TOPAS software was implemented to measure the crystallite size of the particles. The density of FeNi particles was assessed by the helium gas replacement method using a true density measuring apparatus (BELSORP-max, MicrotracBEL Corp., Osaka, Japan), which was controlled by a computer. By filling the cavity between the particles using helium gas, the volume of the FeNi particles was measured. The true density was determined by dividing the mass of FeNi particles by the effective volumetric capacity.

The magnetic properties of the FeNi particles and the powder core were evaluated using vibrating sample magnetometry (VSM) across a field ±20 kOe using a High Sensitivity VSM System TM-VSM311483-HGC (Tamakawa Co., Ltd). The DC-bias performance for all powder core specimens in a wire wounded toroidal shape were examined with the maximum applied field of 20 A and maximum magnetic field of 230 Oe using a Precision LCR Meter 4284A (Keysight Technologies, Inc.). In addition, by embedding the powder core in epoxy resin and curing it, a cross-sectional SEM image of the distributed particles in the powder core was taken. After cutting the resin, sandpaper and buffing were used to polish it. The polished surface was examined using SEM after ion milling.

3.3 Result and discussion

3.3.1 Characteristics of the FeNi particles

The particles morphology of all samples identified by TEM images is given in **Figure 3.1**. As can be seen in **Figure 3.1(d)**, decreasing the carrier gas flow rate and increasing the temperature led to fewer hollow particles. In the case of 1200 °C (**Figure 3.1(c1-5)**), decreasing the carrier gas flow rate from 5 L/min (S12-5.0) to 2.5 L/min (S12-2.5) reduced the number of hollow particles by a few percent according to the dense and hollow particles count in **Figure B.S4**. A further decrease of the carrier gas rate to 1.3 L/min (S12-1.3) and 0.5 L/min (S12-0.5) reduced the hollow particle percentage (HP) by 10% and 5%, respectively. However, by increasing the temperature to 1300 °C, as shown in **Figure 3.1(b1-3)**, the sample of S13-5.0 had a similar percentage of hollow particles as S12-5.0 whereas the samples of S13-2.5 and S13-1.3 showed a significant reduction in the percentage that was proportional to the carrier gas flow rate. Further increasing the temperature to 1400 °C, as shown in **Figure 3.1(a1-3)**, the S14-5.0 sample provided a hollow particle percentage of approximately one-third that of the S12-5.0 and S13-5.0 samples. Moreover, the alteration of the carrier gas flow rate for S14-2.5 and S14-1.3 reduced the percentage of hollow particles to below 5%. Although the percentage can be suppressed by raising the temperature and reducing carrier gas flow rate, carbon formation, as indicated by the blue arrow in TEM images, occurred with the inversely amount to the hollow particles. The carbon might be generated by ethanol decomposition in the system [123], which may result in CO gas (**Figure B.S5**) and then reacts with H_2 gas on the surface of FeNi particles to form carbon nanoparticles, as shown by equation (3.1)[124].

$$CO + H_2 \rightarrow C + H_2O \qquad (3.1)$$

Based on these TEM images, lower carrier gas flow rates and higher temperatures resulted in larger amounts of carbon nanoparticles formation. Thus, we focused on a temperature of 1200 °C and a carrier gas flow rate between 1.3 and 5.0 L/min for further investigation.

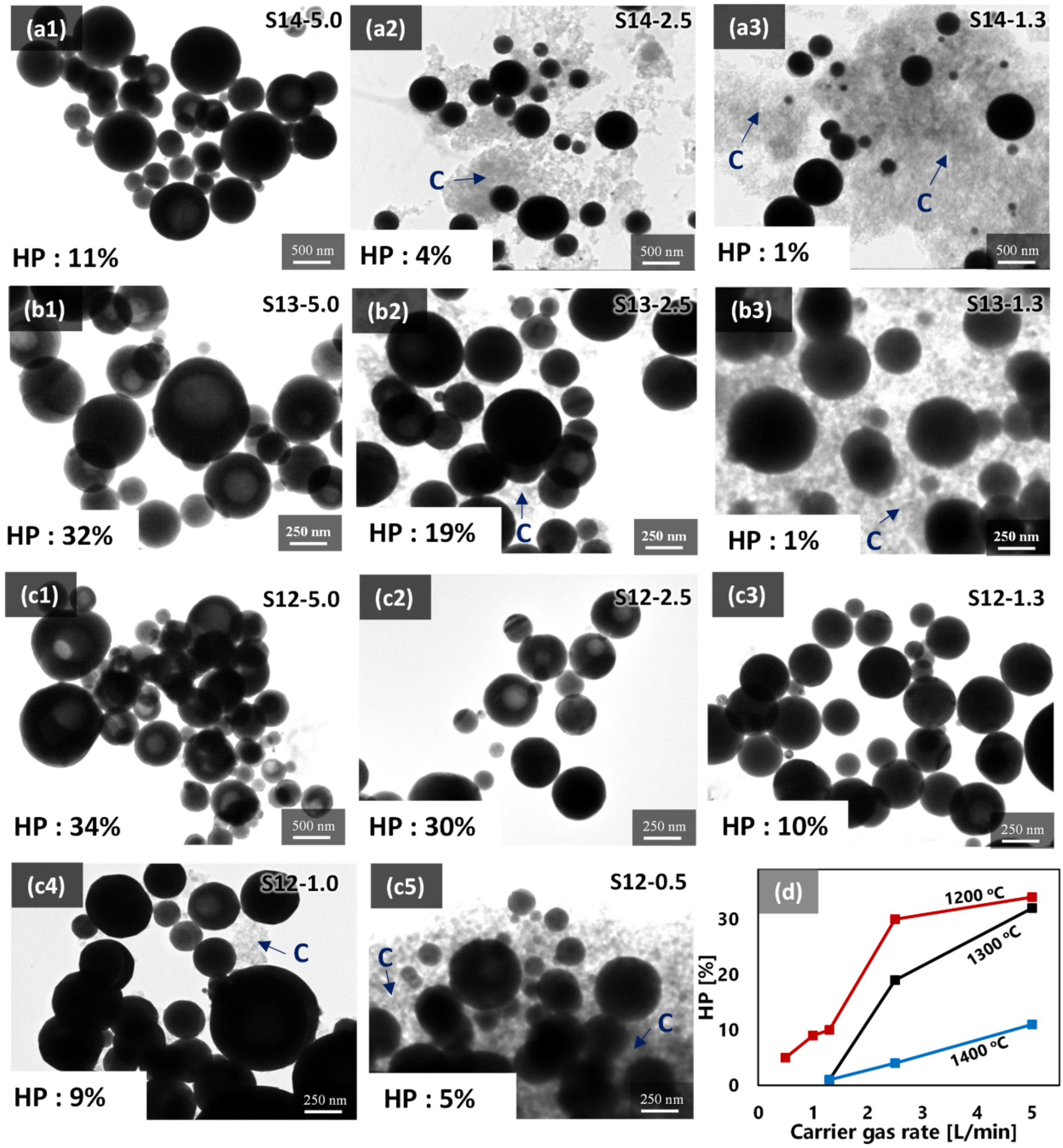

Figure 3.1. TEM images of FeNi particles in various carrier gas flow rates with different temperatures: (a1-3) 1400 °C; (b1-3) 1300 °C; (c1-5) 1200 °C. HP is the percentage of the number of hollow particles. (d) The correlation of the carrier gas flow rate and temperature to the HP.

The morphological change from densification could be confirmed by SEM images, as shown in **Figure 3.2(a)** and **3.2(b)**. The smaller particles size might indicate the formation of dense particles and vice versa [107]. The sample of S12-5.0 had a broad particle size distribution with the geometric average diameter of 402 ± 2 nm. A longer residence time from the decreasing of the carrier gas flow rate caused narrowing of the particle size distribution and lessening of the geometric average diameter to 385 ± 2 nm and 371 ± 2 nm for the samples S12-2.5 and S12-1.3, respectively. The densification was also proven by the increased density of FeNi particles in accordance with the increased percentage of dense particles in the lower carrier gas flow rates, as presented in **Figure 3.2(c)**. The density value of the FeNi particles increased proportionally with the reducing carrier gas flow rates, which were 7.38, 7.85, and 8.33 g/cm^3 from the carrier gas flow rates of 5, 2.5, and 1.3 L/min, respectively.

To confirm the crystal structure of the FeNi particles, **Figure 3.2(d)** exhibits a typical XRD pattern of face centered cubic (fcc) FeNi without the presence of the oxidated state of Fe and Ni. The sharp peaks represented the highly crystalline nature of the FeNi particles [78]. The slight broad hump peak at approximately 26° was attributed to the formation of carbon nanoparticles during the spray pyrolysis process[125][81]. Additionally, decreasing carrier gas flow rates led the gradual increase of the crystal size of the FeNi particles due to the increasing phase formation in a longer residence time[126]. An extensive investigation was also carried out using an XRD pattern at a low angle to confirm the $L1_0$ phase of FeNi particles, which must be avoided. **Figure B.S6** shows a devoid of the $L1_0$ FeNi phase peak. This means that our FeNi particles do not have the hard magnetic properties of FeNi-based alloys.

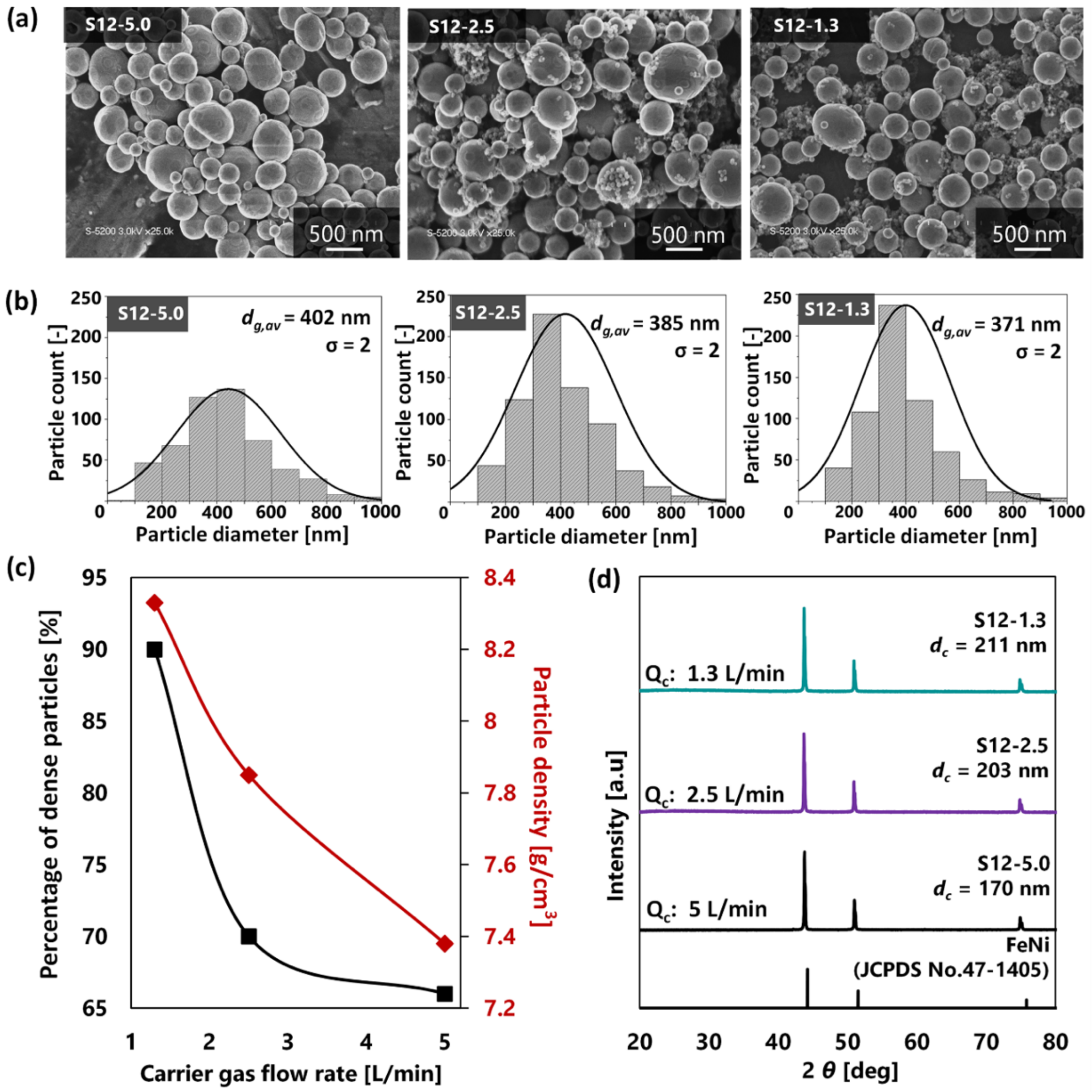

Figure 3.2. FeNi particles in different carrier gas flow rates: (a) SEM images and (b) particle size distribution, where dg,av is the geometric mean diameter and σ is the geometric standard deviation. (c) Effects of carrier gas flow rate on the percentage of dense particles and density of FeNi particles. (d) XRD pattern of FeNi particles in different carrier gas flow rates. These samples are obtained at 1200 °C.

The magnetic characteristic of the FeNi particles was evaluated by the hysteresis curve (*B*-*H* loop) as depicted in **Figure B.S7**. All the samples revealed ferromagnetic characteristics and had similar saturation magnetic flux density (B_s) values of 1.5 T. This B_s value was close to the theoretical B_s value for FeNi materials (1.5 T) [127], which proved that the FeNi particles generated by spray pyrolysis route exhibit high purity and crystallinity [88,128]. Furthermore, the coercivity of S12-5.0, S12-2.5, and S12-1.3 was 0.01, 0.009, and 0.01 kOe (0.8, 0.7, and 0.8 kA/m), which is much lower than that of the FeNi powder with no $L1_0$ phase reported before (14.5 kA/m) [129]. Because the hysteresis loss of the core is related to the coercivity value, this low result implies that the FeNi particles are unlikely to affect it [130]. Moreover, the particles from this method exhibited the best saturation magnetic characteristic among the nano- and submicron sized particles from the other methods summarized in **Figure 3.3**. In the range of submicron sized particles and high magnetic saturation value (> 1.4 T), thermal decomposition, sol gel, and spray pyrolysis methods have the potential for large-scale production. However, based on these previous works, the thermal decomposition and sol gel methods were unable to produce the perfect spherical particles and required several steps in fabricating the FeNi particles [131,132].

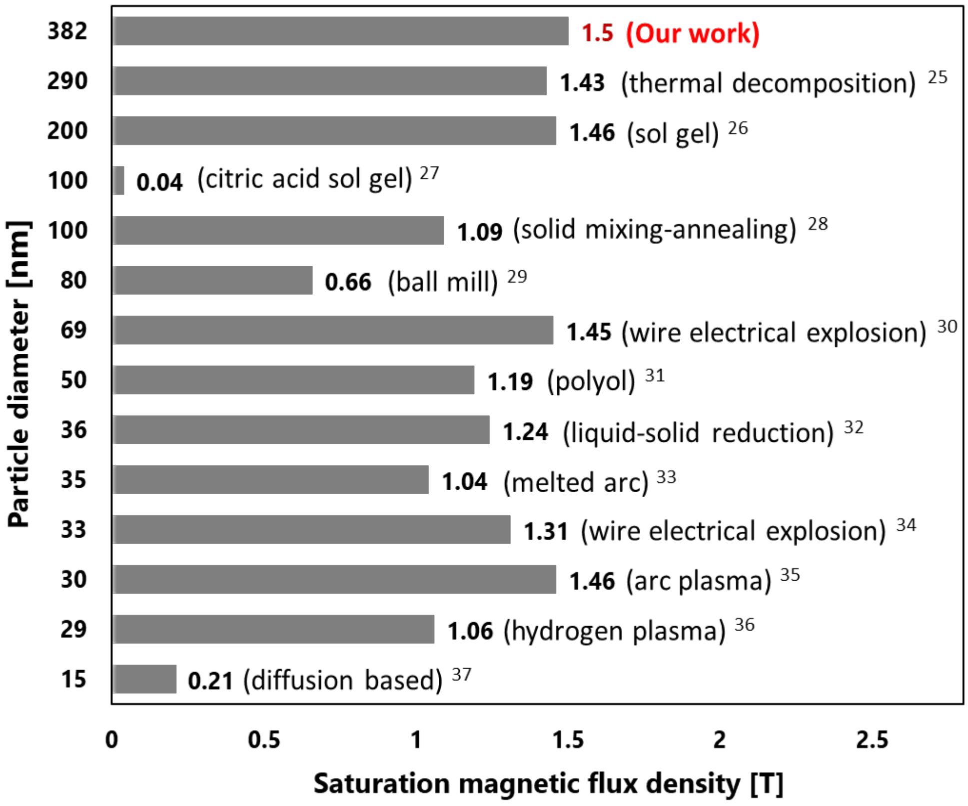

Figure 3.3. Comparison of the magnetic saturation value of FeNi particles in the range of nano- and sub-micrometer size to the other methods. [48,74,85,131–139]

3.3.2 Application of FeNi particles in the powder core

The synthesized FeNi particles were applied as the secondary particles in the powder core. **Figure 3.4** depicts the cross-sectional SEM image of the powder core. The spherical and submicron sized FeNi particles were reasonably compacted and well distributed among the micron-sized primary particles.

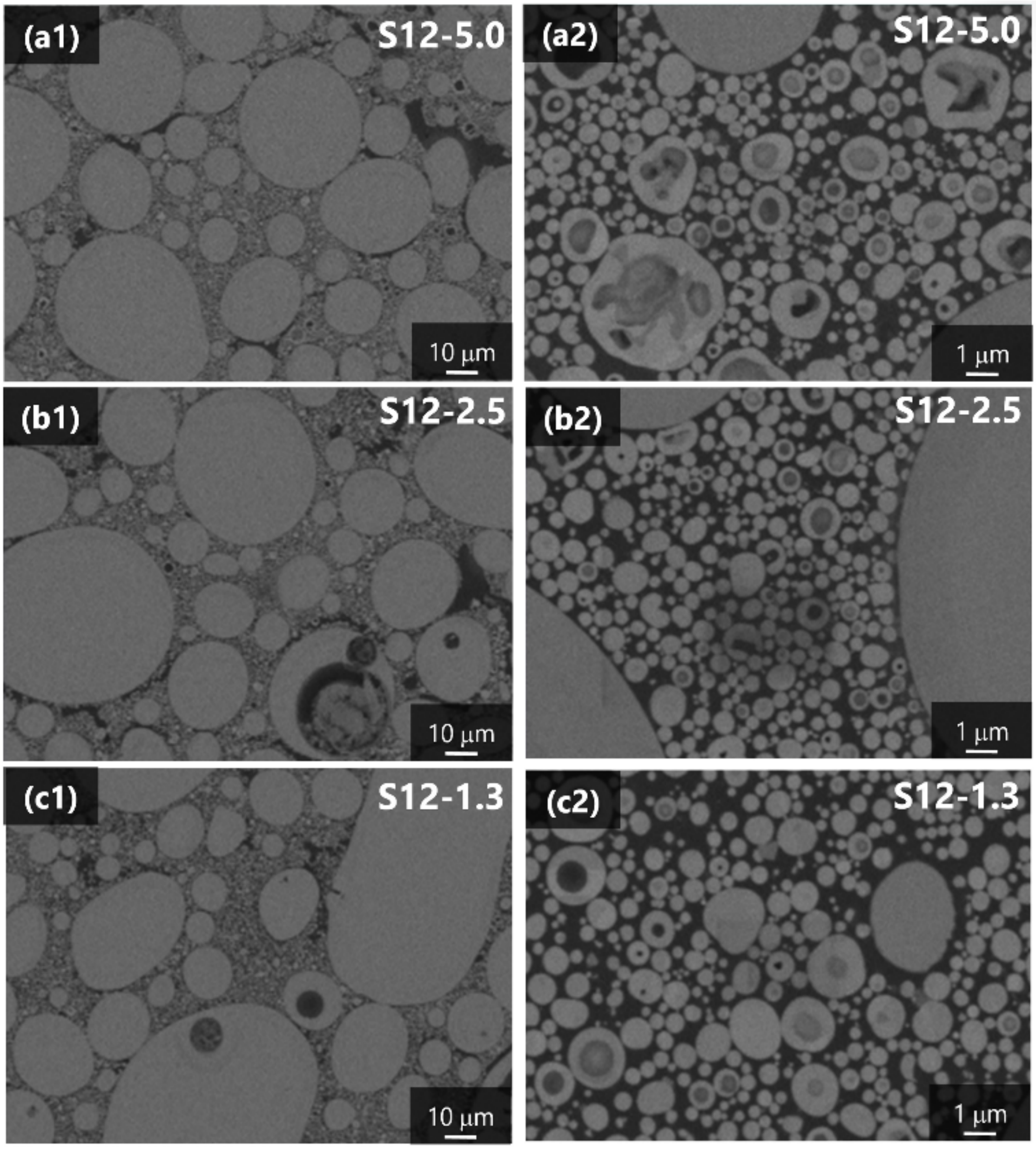

Figure 3.4. Cross-sectional SEM images of the powder core with three types of FeNi particles at different magnifications: (a) S12-5.0; (b) S12-2.5; and (c) S12-1.3 as the secondary particles. Images with different magnification: 1, low magnification image with 1.0k; and 2, high magnification image with 10.0k.

The addition of FeNi particles as the secondary particles affected the powder core characteristic quantitatively. The relative packing density of all specimens shown in **Table 3.2** showed higher packing percentages with the addition of the denser FeNi particles. This was attributed to the smaller size and the higher density of the spherical FeNi particles.

Table 3.2. The effect of the additional secondary particles from different prepared carrier gas flow rate on the physical property of the powder core

Sample	Packing percentage (η) [%]	Saturation magnetic flux density (B_s) [T]	Initial inductance ($L(0A)$) [μH]	Saturation current (I_{sat}) [A]
S12-5.0	78.9	0.908	6.46	10.2
S12-2.5	79.7	0.921	6.96	11.2
S12-1.3	80.1	0.922	6.61	12.1

The powder core performance was examined through the DC bias current characteristic. The powder core was able to gradually become saturated with the increasing applied current, which was indicated by a descending inductance. **Figure 3.5** represents the deteriorating inductance value of the samples by increasing the applied electric current. For this measurement, the deterioration of the inductance value was observed from the specimens with the same level of permeability value. The sample of S12-5.0 showed the fastest decrease of the inductance value from its initial value followed by S12-2.5 and S12-1.3. The powder core properties, summarized in **Table 3.2**, exhibited I_{sat} values of 10.2, 11.2, and 12.1 A for the S12-5.0, S12-2.5, and S12-1.3 samples, respectively.

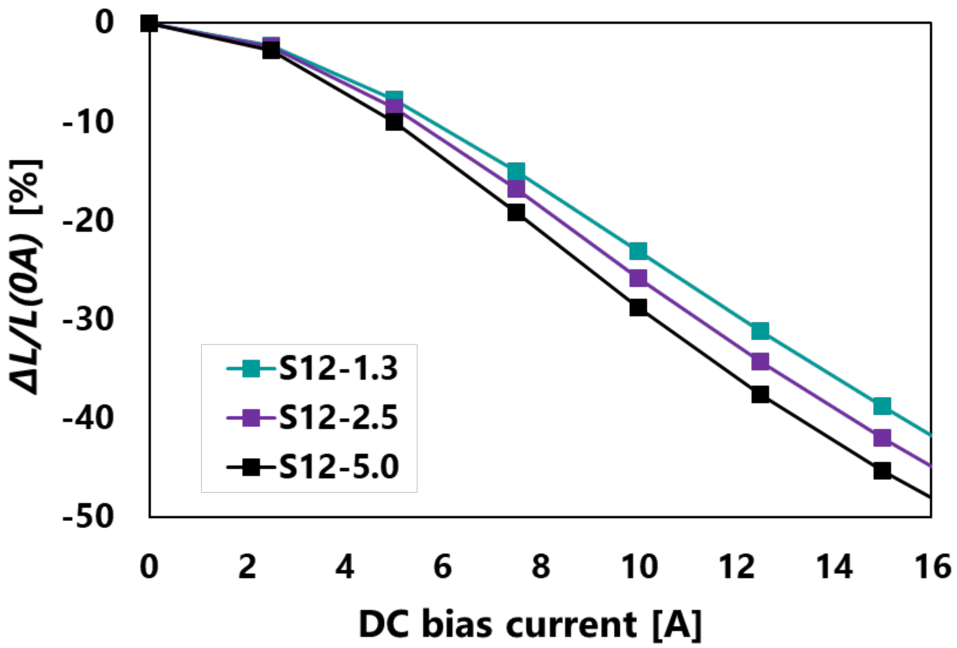

Figure 3.5. Diminishing inductance from its initial value for presenting DC bias performance of the powder core.

The I_{sat} value was taken when the initial inductance had decreased by 30% as the saturation point ($\Delta L/L(0A)$ = -30%). Although the I_{sat} value could be generally related to the B_s value of the powder core, the powder core of all samples exhibited unremarkably different B_s values (see **Table 3.2**). Therefore, the morphology of the secondary particles was proposed to influence this performance the most. The presence of hollow particles allowed a magnetic flux path only in their shell so the particles will become saturated rapidly under high current. Furthermore, from **Figure 3.4**, the smaller diameter of the densified particles provided a more effective distributed adjacent non-magnetic region among the particles. Quantitatively, the average distance between particles from the use of the S12-5.0, S12-2.5, and S12-1.3 samples were 122, 184, and 196 nm, respectively. A closer distance in this range resulted in an easier magnetic domain shift during magnetizing, and thus decreased I_{sat} value[32] as represented in **Figure 3.6**.

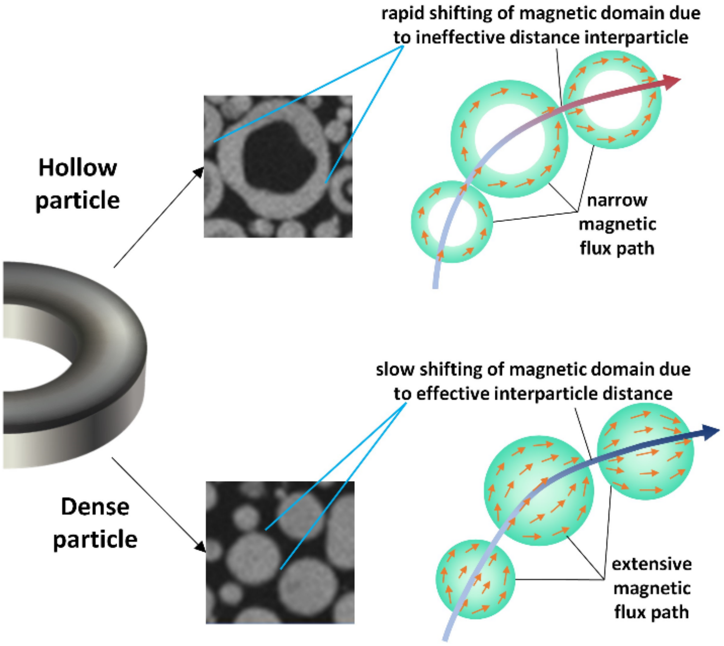

Figure 3.6. Magnetic flux path through submicron sized FeNi particles.

3.4. Conclusion

In summary, a novel approach to control the structure of spherical and submicron sized FeNi particles synthesis is successfully conducted with the high-quality characteristic similar to the theoretical value. This study is the first investigating the spherical and submicron sized FeNi particles as the secondary particle in a powder core. The process parameters, i.e., temperature and carrier gas flow rates, considerably influence the characteristic of the FeNi particles. The higher temperature and lower carrier gas flow rates lead to the densification of the FeNi particles. Consequently, the particle structure is altered from low-density to high-density FeNi particles (hollow to dense particles), although carbon formation on the surface of the particles also occurs. To prevent carbon formation, in this research, we focused on a temperature of 1200 °C. The lower carrier gas flow rate provides a higher percentage of dense particles and a smaller particle size distribution with an increasing crystallite diameter. It is noticeable that the densification is beneficial for the application of FeNi particles as the secondary material of the powder core. The denser and smaller FeNi particles exhibit better performance of the DC bias characteristic for the powder core owing to its characteristic and effectively adjacent non-magnetic region distribution. Having a comparatively high magnetic saturation and prominent DC bias characteristic, the densified FeNi particles promise an enhancement of the powder core performance for industrial purposes.

Acknowledgements

This work was supported by JSPS KAKENHI Grant Number 19H02500. This work was partly supported by the Center for Functional Nano Oxide at Hiroshima University, International Network on Polyoxometalate Science, JSPS Core-to-Core Program, The Information Center of Particle Technology, Japan, and Hosokawa Powder Technology Foundation. We would like to thank the Ministry of Education, Culture, Sports, Science and Technology (MEXT) of Japan for providing a doctoral scholarship to E. L. S. We thank Dr. Makoto Maeda of the Natural Science Center for Basic Research and Development (N-BARD) at Hiroshima University for TEM observations and discussion. We thank Edanz (https://jp.edanz.com/ac) for editing a draft of this manuscript.

Chapter 4

One-step aerosol synthesis of SiO_2 coated FeNi particles by using swirler connector-assisted spray pyrolysis

Abstract

Silica-coated soft-magnetic particles are essential for some powder magnetic cores consisting of primary (coarse particles) and secondary (fine particles) soft-magnetic particles in the advancement of electric devices. Herein, we report the first investigation on the direct synthesis of submicron-sized silica-coated FeNi (FeNi@SiO_2) particles as the secondary particle using connector-assisted spray pyrolysis route. Provided by computational fluid dynamics (CFD) calculation in applying different connector types, i.e. T-shaped and Swirler, we found that the mixing performance between FeNi and HMDSO vapor in the swirler connector played an important role in resulting heterogeneous nucleation, which is crucial for obtaining the higher coating ratio and fewer undesired nanoparticles than that of T-shaped connector. The as-prepared submicron-sized FeNi@SiO_2 particles (353 nm) with the highest coating ratio (95.9%) demonstrated remarkable DC bias characteristic (I_{sat}) and eddy current loss values on a powder magnetic core, promising the practical application in manufacturing soft-magnetic components.

Published in part in Ind. Eng. Chem. Res. 2022, 61, 49, 17885–17893

4.1 Introduction

The rapid revolution of electrical devices in the automotive and digitalization fields for sustainable development goals has urged the advancement of soft-magnetic components, such as powder magnetic core inductors [4]. A powder magnetic core is a vital component that serves as a power converter for a device's components [140]. In some cases, a powder magnetic core consists of primary (coarse particles) and secondary (fine particles) soft-magnetic particles. Based on several reports, selecting secondary particles is critical for achieving a desirable powder magnetic core feature [118,120,141,142]. FeNi is preferred as a secondary material because of its high magnetic saturation and permeability [45]. In addition, submicron-sized particles are highly favored for increasing the packing density of a powder magnetic core due to the difficulties associated with handling nanoparticles [83]. Our group recently succeeded in producing the spherical and submicron-sized FeNi particles with a diameter of approximately 400 nm, as well as high density and saturation magnetic flux density values. However, there is still remaining an issue in the practical use of the powder core owing to the eddy current loss. When the eddy current loss value is high, the inductor's performance becomes less efficient because of the energy loss [143]. Therefore, to reduce the eddy current loss value, FeNi particles must be coated with an insulating material.

Based on its chemical stability, silica can be highly considered as the coating material [144–147]. Some studies revealed the stability improvement in silica-coated $FeNi_3$ particles against oxidation [53] and decreasing permeability at higher frequencies [58]. These studies, however, conducted $FeNi_3$ particle synthesis in the first step and silica coating in the liquid phase method in the second step, which is unfavorable because of the long process in the multiple steps. Alternatively, an aerosol process is desired to achieve the silica coating on the core particles in direct synthesis. Several studies have attempted the aerosol process in producing silica-coated particles so far. By using tetraethyl orthosilicate (TEOS) as the SiO_2 precursor, Post *et al.* successfully demonstrated controllable silica-coated TiO_2 particles with good thermal stability properties via chemical vapor deposition using a dielectric barrier discharge with a plasma filament [148]. Furthermore, Teleki *et al.* used hexamethyldisiloxane (HMDSO) as the SiO_2 precursor in the flame spray pyrolysis technique to exhibit hermetically coating of $Fe_2O_3@SiO_2$ and $TiO_2@SiO_2$ with silica as the shell [70,149]. This gas-phase method resulted in a mostly homogeneous coating thickness of approximately 2–4 nm with good stability through the isopropanol chemisorption and photooxidation of isopropanol to acetone analysis. Although these methods seem promising, they are likely to cause difficulties in the FeNi precursor reduction because they involve oxygen. Another study conducted by Nomoev et al. successfully produced submicron-sized Cu@SiO_2 by using a tubular reactor with an electron beam evaporator in the absence of oxygen [67], but this method requires a pure ingot of Cu, which is less abundant than its metal salt. Furthermore, in a comparison of the metal transition from metal salt to its metal alloy in a gas phase, the spray pyrolysis method has advantages over the aforementioned methods such as low cost, versatility in maintaining a reduced atmosphere [100,104,122,150,151], ease in controlling the particle's size, morphology [87,152,153], and chemical composition [88,128,154,155], as well as prevention of agglomerating particles [156]. Thereby, spray pyrolysis with a closed electric furnace system is highly considered. Until now, the synthesis of the silica-coated FeNi (FeNi@SiO_2) particles in a one-step aerosol process has not been investigated. Since the reduction to obtain FeNi alloy and the coating processes in one step is complicated, the silica coating on the FeNi particles is quite challenging. Moreover, a uniform silica coating on the FeNi particles is highly desired to achieve a characteristic improvement of a powder magnetic core.

To perform the direct synthesis of FeNi@SiO_2 particles with a uniform coating, we proposed a new approach to the closed spray pyrolysis system assisted by a connector, which is called the connector-assisted spray pyrolysis method. This method employs two strategies for controlling coating performance, as elaborated in **Scheme 4.1**. The first strategy is introducing the HMDSO vapor as the SiO_2 precursor on the intermediate product of FeNi aerosol synthesis. To achieve this, a preheating system before the connector-assisted spray pyrolysis reactor is required. Therefore, a connector is needed to join the preheater and spray pyrolysis reactor to introduce the HMDSO vapor. Because the connector geometry can determine the fluid flow and mixing quality between two aerosols, the selection of the connector geometry is important. Subsequently, the second strategy is evaluating various connector geometries, i.e. T-shaped, Swirler-3, and Swirler-6 (see the dashed box in **Scheme 4.1**), to precisely adjust the mixing performance between the FeNi aerosol and HMDSO vapor. A prominent mixing performance must be achieved to perform heterogeneous nucleation, which prevents the generation of nanoparticles and improves coating quality. In these strategies, the carrier gas of the HMDSO vapor (Q_s) and an additional gas (Q_a) were used to control the amount of HMDSO vapor and maintain the homogeneous distribution among the aerosols, respectively.

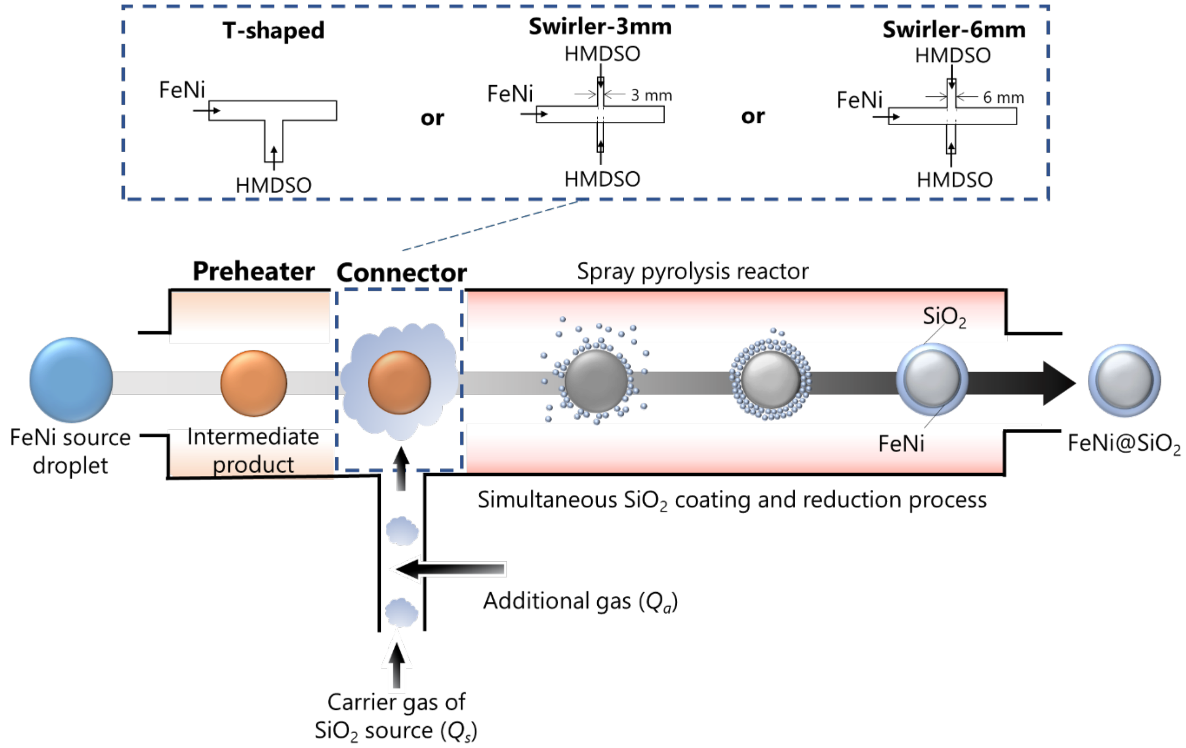

Scheme 4.1. Schematic of the proposed system for synthesizing FeNi@SiO_2 particles in a direct process.

In this study, the SiO_2 coating of FeNi particles was firstly investigated by determining the effect of connector geometry on the coating quality. To support this study, a numerical approach based on computational fluid dynamics (CFD) was conducted to perform the mixing performance of the aerosols and predict the SiO_2 generation. In addition, the gas flow rate of Q_a was tuned to optimize the coating quality in the most prominent connector geometry. The synthesized FeNi@SiO_2 particles were characterized to select the most prominent product for the powder magnetic core application. Eventually, the eddy current loss and DC bias characteristic were examined to stipulate the silica coating effect on the powder magnetic core characteristic improvement.

4.2 Experimental section

4.2.1 Particles synthesis

The FeNi@SiO_2 particles were synthesized via connector-assisted spray pyrolysis route equipped with a preheater and different connector types for introducing the silica source (**Figure 1**). The droplets of FeNi precursor solution with a total concentration of 0.2 mol/L, consisting of $Fe(NO_3)_3{\cdot}9H_2O$ and $Ni(NO_3)_2{\cdot}6H_2O$ in a solvent of 25 vol% ethanol-water, were transported by 5 L/min carrier gas of 5%H_2-Ar into a preheater made of a Pyrex glass, with

395-mm length and 36-mm diameter, before meeting hexamethyldisiloxane (HMDSO)-laden 5%H_2-Ar gases through the connector. HMDSO was used as the silica precursor in a precisely controlled amount. The following three types of connectors were used in this study, described in **Figure 4.1**: i) A 20-mm diameter T-shaped tube (T-shaped), ii) A 20-mm-diameter tube with two 3-mm-diameter tangential inlets (Swirler-3), iii) A 20-mm-diameter tube with two 6-mm-diameter tangential inlets (Swirler-6) (see the dashed-lined box in **Figure 4.1**).

In the connector part, FeNi aerosol and HMDSO vapor were mixed before entering the spray pyrolysis reactor with a tube length of 1300 mm and an inside diameter of 30 mm. The temperature of the preheater was maintained at 300ºC, whereas the temperature of the connector was maintained at 150ºC. The reactor temperature was adjusted by five enclosed furnaces, 1200 mm in length, at 1200ºC or 1400ºC. The HMDSO was kept in the bubbler at a temperature of 2ºC based on the Antoine equation calculation and transported by HMDSO vapor carrier gas (Q_s) of 5%H_2-Ar at 10 mL/min. It corresponds to 0.046 g/h of supplied SiO_2 and 7.5 wt% of SiO_2 in the synthesized particles at a saturated condition. The additional carrier gas flow rate (Q_a) of 5%H_2-Ar was controlled to maintain the mixing performance of FeNi aerosol and generated SiO_2 from HMDSO. The temperature of the Q_a was at room temperature (approximately 25ºC). Finally, the product of the FeNi@SiO_2 particles was collected in a bag filter at a temperature of 100ºC.

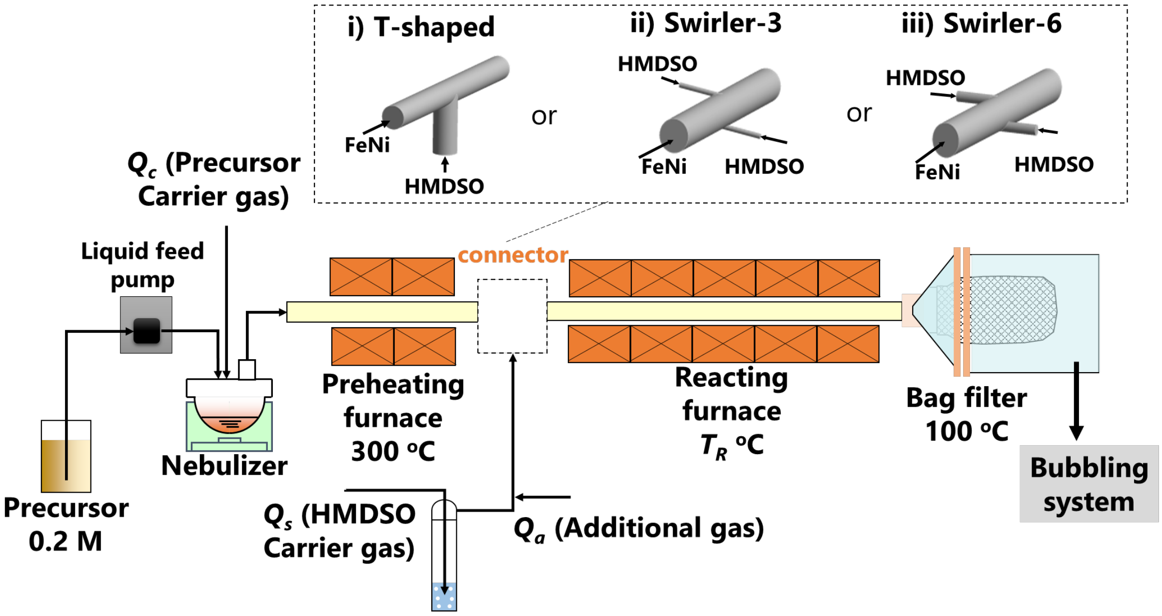

Figure 4.1. Experimental set-up of the synthesis of FeNi@SiO_2 via connector-assisted spray pyrolysis route using different connector types. i) T-shaped, ii) Swirler-3, iii) Swirler-6.

4.2.2 Particles characterization

Field emission scanning electron microscopy (FE-SEM; S-5200, 20 kV, Hitachi High-Tech. Corp., Tokyo, Japan) and transmission electron microscopy (TEM; JEM-2010, 200 kV, JEOL Ltd., Tokyo, Japan) were used to examine the morphology of FeNi@SiO_2 particles. X-ray diffraction was used to determine its crystal structure (XRD; D2 PHASER, Bruker Corp., Billerica, MA, USA). The cross-sectional image of the FeNi@SiO_2 particles was observed by using a high-angle annular dark-field scanning TEM (HAADF-STEM) and energy-dispersive X-ray spectroscopy (EDS) mapping of elemental Fe, Ni, Si, and O. Regarding the powder magnetic core, FeNi@SiO_2 particles were added to micron-sized Fe-Si-B particles to make a powder magnetic core with a ratio of 1:4 for FeNi@SiO_2 to Fe-Si-B particles. A Precision LCR Meter 4284A shape (Keysight Technologies, Inc.) with a maximum-applied field of 20 A, and a maximum magnetic field of 320 Oe was used to investigate the DC bias performance of all powder core specimens in wire wounded toroidal. The core loss was measured by using the B-H analyzer SY-8218 (IWATSU ELECTRIC Co., Ltd., Tokyo, Japan). First, the toroidal core was wound with primary and secondary windings. Then, an alternating current was applied to the primary winding as an excitation current, and the electromotive force induced in the secondary winding was measured. Subsequently, the eddy current loss was calculated based on the phase difference between the exciting current and the induced electromotive force. The smaller the difference phase, the smaller the loss.

Table 4.1. Experimental conditions for various parameters: connector types, temperatures, and additional gas flow rates.

Sample	Connector type	Silica source inlet diameter [mm]	Reactor temperature (T_R) [^{o}C]	Additional gas flow rate (Q_a) [L/min]
Ts-12-3	T-shaped	20	1200	3
Ts-14-3			1400	
Sw3-12-3	Swirler	3	1200	
Sw3-14-3			1400	
Sw6-12-3	Swirler	6	1200	
Sw6-14-3			1400	
Sw6-14-5				5
Sw6-14-7				7

4.2.3 Mixing performance simulation

To better understand the coating quality, the mixing of FeNi aerosol and HMDSO vapor was simulated by using CFD. Ansys Fluent, which is embedded in Ansys Workbench 2021 R1, was used to perform three-dimensional (3D) calculations. The domain was divided into approximately 250,000 meshes of unstructured tetrahedra (**Figure C.S1**). The FeNi aerosol inlet was defined by Lagrangian model as uniform inert droplets with a diameter of 5 mm, while the HMDSO vapor was defined as an inert gas following its physical properties. The inlet velocity of the inlet sources corresponded to the experimental conditions. The velocity of the FeNi aerosol inlet is 0.365 m/s at 573 K, whereas the velocity of the HMDSO vapor is based on the size and geometry of the inlet on the connector part following the Q_a. The species in this simulation were assumed to behave as an ideal gas. The turbulence Shear-Stress Transport (SST) k-w model was used to represent the fluid flow. The walls were set as adiabatic and smooth with no-slip conditions. The temperature distribution and the residence time from the particle tracking in the simulation were used to obtain the analytical value of the HMDSO oxidation following the first-order reaction as written in equation (4.1) [69].

$$\frac{dC}{dt} = -k_g C \qquad (4.1)$$

where C is the vapor number concentration of HMDSO [m^{-3}] and k_g is the gas-phase oxidation rate constant of $4 \times 10^{17} \exp(-3.7 \times 10^5/(8.314 \times T))$ s^{-1}.[111]

4.3 Results and discussion

The coating quality was firstly examined by employing various connector types, i.e. T-shaped, Swirler-3, or Swirler-6, at different reactor temperatures of 1200°C and 1400°C. The temperature effect was initially investigated because it affects the metal salt reduction process[2] and the HMDSO oxidation rate [69]. In the case of 1200°C, the particles morphologies using all connector types were observed in the SEM images (**Figure 4.2(a1-c1)**). The presence of particles with a separated phase between FeNi and its oxidation state (red circle) indicates an incomplete reduction process [122]. These particles were also visible in the TEM image, as shown in **Figure 4.2(a2–c2)**. Several uncoated particles in the TEM images were also noticed. Thus, the temperature at 1200°C was inefficient for the synthesizing FeNi@SiO_2. In contrast, spherical FeNi@SiO_2 particles were observed in the SEM images (**Figure 4.2(d1-f1)**) when the reactor temperature was set to 1400°C in all connector cases. Spherical coated particles with a high amount of nanoparticle generation (red arrows) from the use of T-shaped connector are denoted in **Figure 4.2(d1)**. Meanwhile, in the case of the Swirler-3 connector, spherical coated particles with a significantly lower amount of the aggregation of nanoparticles are shown in **Figure 4.2(e1)**. Furthermore, increasing the inlet diameter of the HMDSO vapor at the Swirler-6 resulted in the generation of spherical coated particles with barely detectable nanoparticles (**Figure 4.2(f1)**). The coating quality at this temperature was determined using TEM analysis. The images of the core-shell structured particles are shown in **Figure 4.2(d2–f2)**. The coating quality was quantified using the percentage value of the coating ratio (CR), which is based on the ratio of the number of perfectly coated particles to the number of total particles from the TEM images (see Supporting Information). Overall, all connector types provided a relatively efficient coating with a high CR value of more than 90%. However, the sample of Ts-14-3 had not only the lowest CR value but also the highest amount of nanoparticle generation (red arrows). Conversely, the use of the Swirler connector, especially the sample of Sw6-14-3, improved the CR value (94.8%) and significantly reduced nanoparticle generation. There are two possibilities to explain the improvement of the coating quality in the Swirler case. First, a heterogeneous nucleation tendency from a proper mixing provided by the swirling flow [70,157,158]. Heterogeneous nucleation is denoted by the initial step in the formation of new aerosol particles that deposit and evolve on the surface of pre-existing (seed) particles [159]. In our case, the seed particles are represented by the FeNi aerosol, while the deposited vapor is represented by HMDSO vapor. Second, the generated silica particles were deposited onto the core particles followed by sintering[61]. According to the smooth surface of the coated particles, we hypothesized that our case might follow the first possibility.

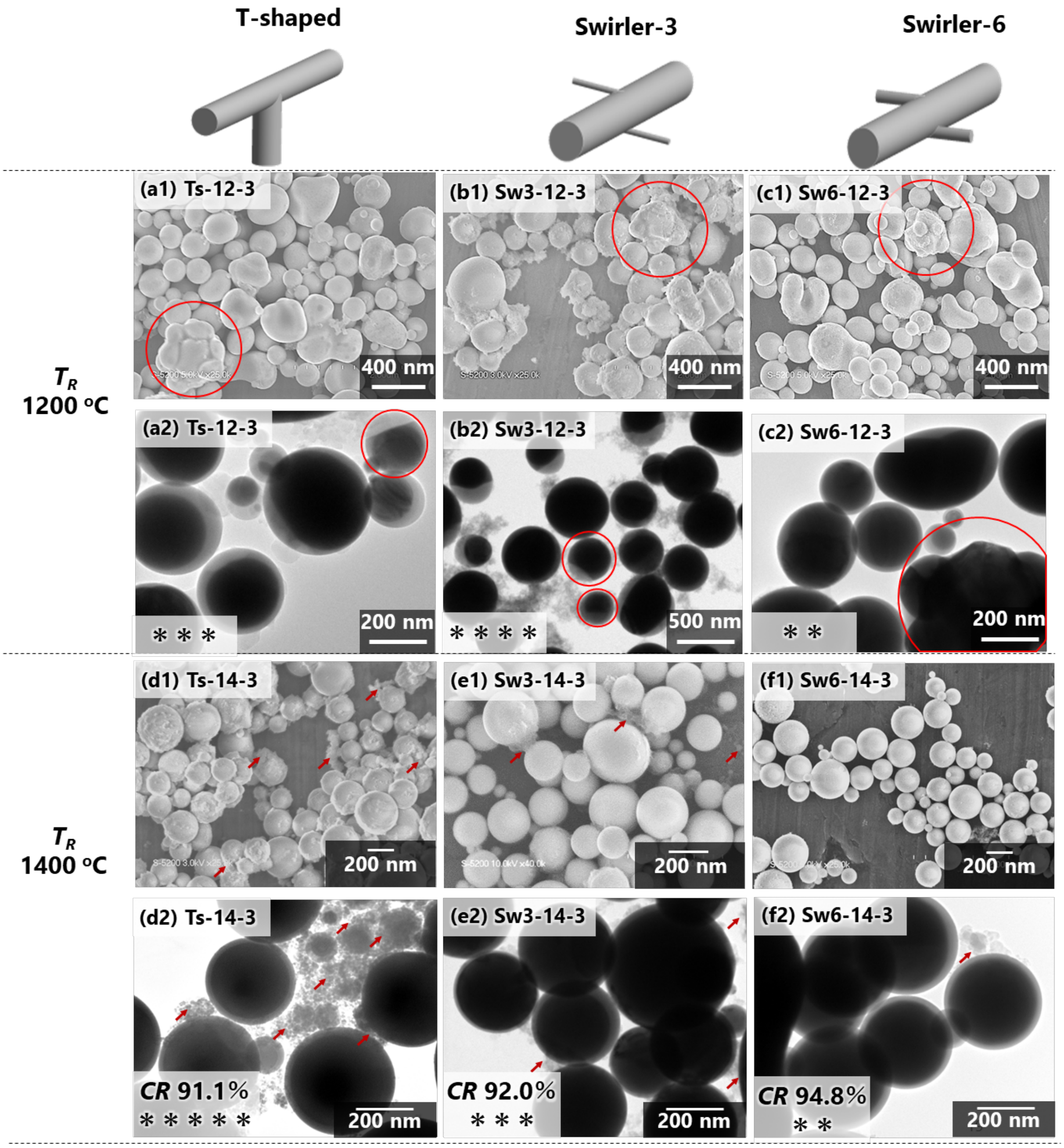

Figure 4.2. FeNi@SiO_2 particle morphology using different types of connectors at reactor temperatures of 1200°C (a–c) and 1400°C (d–f). 1) SEM images; 2) TEM images of particles generated using (a,d) T-shaped, (b,e) Swirler-3, (c,f) Swirler-6. CR is the coating ratio in percentage, we counted at least 150 particles. Number of * indicate the level of nanoparticle generations.

In order to understand the coating process efficiency, CFD analysis was used to examine the temperature distribution, particle residence time, and mixing performance between FeNi aerosol and HMDSO vapor. Overall, a similar temperature distribution of the T-shaped and Swirler-6 cases, in the range of 0 to 0.5 m from the connector inlet, is represented in **Figure 4.3(a1,a2)**. However, the Swirler-6 connector provided a shorter distance to achieve homogeneous temperature than the T-shaped connector (indicated by the yellow color at the center in **Figure 4.3(a1)**). Furthermore, the particle tracking shown in **Figure 4.3(b1,b2)** revealed a remarkable distinction profile. The T-shaped case could not allow the FeNi aerosol (red line) to mix with the HMDSO vapor (blue line) immediately in the connector part. Even though the HMDSO vapor trajectory seemed to be spread fairly surrounding the FeNi aerosol in a few centimeters forward from the reactor inlet, the HMDSO vapor moved to the one-side of the reactor, which is shown by ununiform mixing (separated by the blue and red line at arrow 1, as pointed in **Figures 4.3(b1)** and **Figure 4.3(c1)**). As a result, a region with a relatively high concentration of HMDSO vapor and low concentrations of FeNi aerosol formed, resulting in homogeneous nucleation. In contrast to heterogeneous nucleation, the homogeneous nucleation is defined by the formation of new particles from gaseous compounds in the absence of any surface.[37] Moreover, another region was dominated by FeNi aerosol with a significantly low HMDSO concentration, which could explain the production of uncoated particles. It is supported by the previous work from Teleki et al and Gass et al, the poor mixing between HMDSO vapor and core particles led to the separate SiO_2 particles with the presence of coated and uncoated particles due to homogeneous coating. On the other hand, the Swirler-6 case resulted in uniform mixing instantly at the HMDSO vapor introduction. Even dispersion of FeNi aerosol (red line) and HMDSO vapor (blue line) could be maintained alongside the axial reactor, as denoted by arrow 2 in **Figure 4.3(b2)** and **Figure 4.3(c2)**, suppressing the homogeneous nucleation and allowing heterogeneous nucleation to dominate. Thus, the particles with a higher CR and fewer generated nanoparticles were achieved.

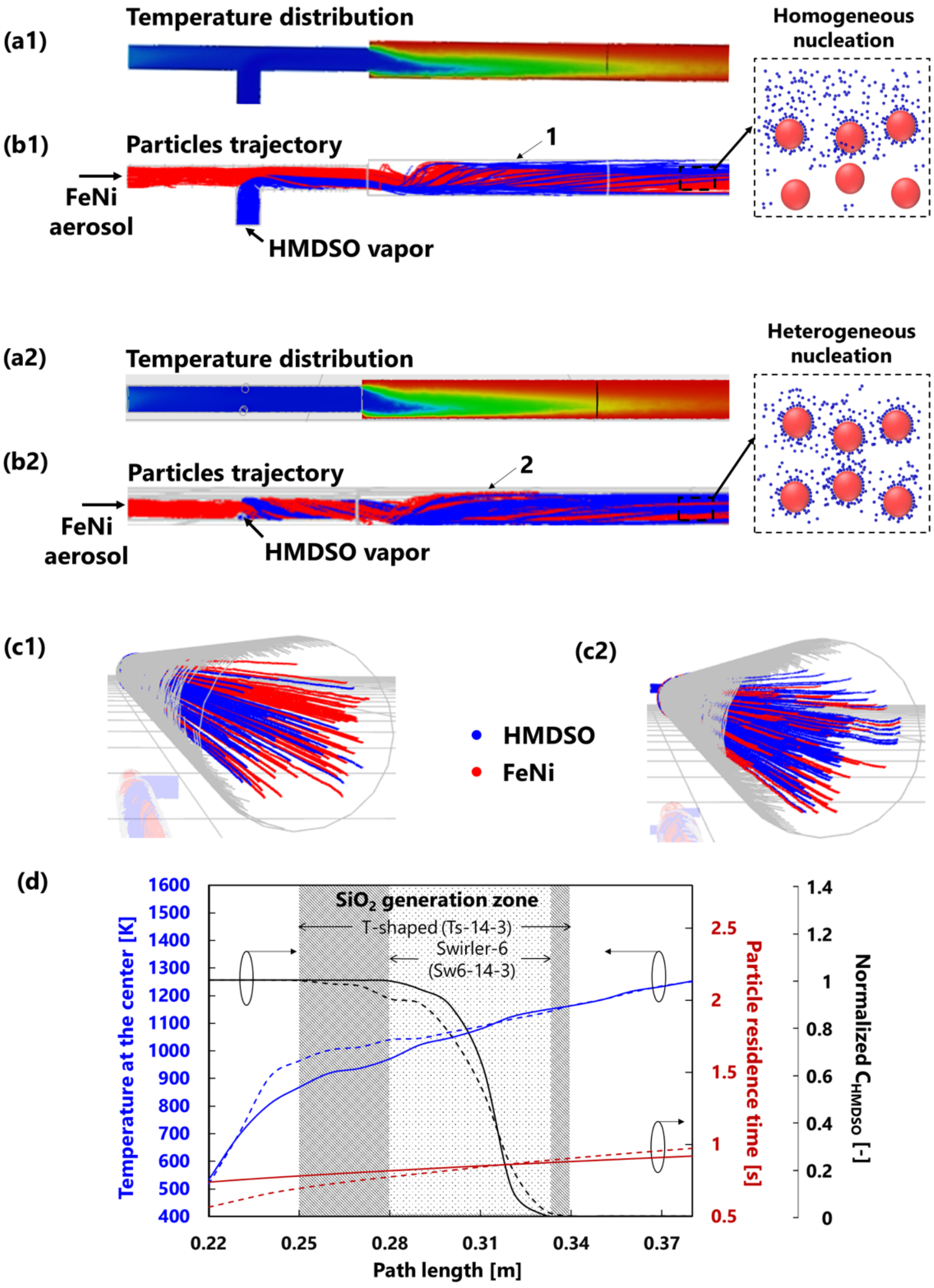

Figure 4.3. The CFD simulation results from different connectors: (a) Temperature distribution on cross-sectional along the axis reactor, blue (bellow 573 K), red (1673 K). Particles trajectory (b) along the axis reactor and (c) near the reactor outlet. 1) T-shaped, 2) Swirler-6. (d) The centerline on the temperature distribution (blue), particle residence time (red), and degradation of the HMDSO concentration due to SiO_2 generation (black) as a function of length. T-shaped (dashed-line), Swirler-6 (solid line).

Furthermore, the HMDSO decomposition was calculated from the integration of the oxidation rate as a function of temperature over time. **Figure 4.3(d)** showed a centerline temperature in connector and reactor sections (blue line) as well as the particle residence time (red line) based on the CFD calculation from two connectors, i.e. T-shaped and Swirler-6. This figure revealed relatively different values in temperature and residence time from those connectors in close-up image despite an overall similar trendline as seen in **Figure C.S2**. It is obvious that the use of T-shape connector provided a sudden increase of the temperature in a short residence time. Consequently, the SiO_2 generation began as soon as the HMDSO entered the reactor with a length between 0.25 and 0.34 m, as described in the plot of HMDSO concentration as a function of length (dashed black line in **Figure 4.3(d)**). Thereby, the rapid increase in temperature may also cause homogeneous nucleation besides the poor mixing between aerosols (**Figure 4.3(b1)**).[35] Meanwhile, the use of Swirler-6 led to gradual temperature and residence time increases, causing the degradation of HMDSO concentration to begin at 0.28 m, within a shorter distance than the T-shaped case. The combination of gentle heat up and effective mixing of FeNi and HMDSO vapor resulted in heterogeneous nucleation.[18,35] Hence, the CR increased, while the nanoparticle amount decreased significantly.

Apart from these two cases, the Swirler-3 case demonstrated a similar phenomenon to the T-shaped case. Although the mixing performance near the connector appeared to be rigorous, ununiform mixing in the subsequent reactor part (**Figure C.S3**) and a rapid increase in centerline temperature (**Figure C.S4**) were insufficient to significantly suppress homogeneous nucleation. As a result, the CR slightly improved and the number of the nanoparticles remained. Based on these observations, it is noticeable that besides the geometry of the Swirler-6 is the best candidate among the applied connectors, the more evenly distributed HMDSO vapor surrounding the FeNi aerosol, as well as the gentler temperature rise, would improve the CR and decrease nanoparticles generation. Therefore, further optimization was performed by controlling the additional gas flow rate (Q_a) with Swirler-6.

Figure 4.4(a1–a3) presented the successful production of FeNi@SiO_2 particles in various Q_a. FeNi@SiO_2 particles with smooth surfaces produced at flow rates of 3 and 5 L/min. The generated nanoparticles were remarkably reduced by using higher Q_a, i.e. 5 L/min, as revealed in the TEM images in **Figure 4.4(b1,b2)**. It was noticed that raising $Q_{a,}$ resulted in a more fairly distributed HMDSO vapor. However, a further increase in Q_a to 7 L/min, resulted in a significant amount of nanoparticle generation (see **Figure 4.4(b3)**). The increase in Q_a was most likely resulted by a lower concentration of the HMDSO in the gas flow, thereby expanding the space between the generated SiO_2 and FeNi aerosols. In addition, a high flow rate provided insufficient residence time, limiting the interaction between generated SiO_2 and FeNi aerosols. Thus, the remaining generated SiO_2 was obtained as generated nanoparticles.

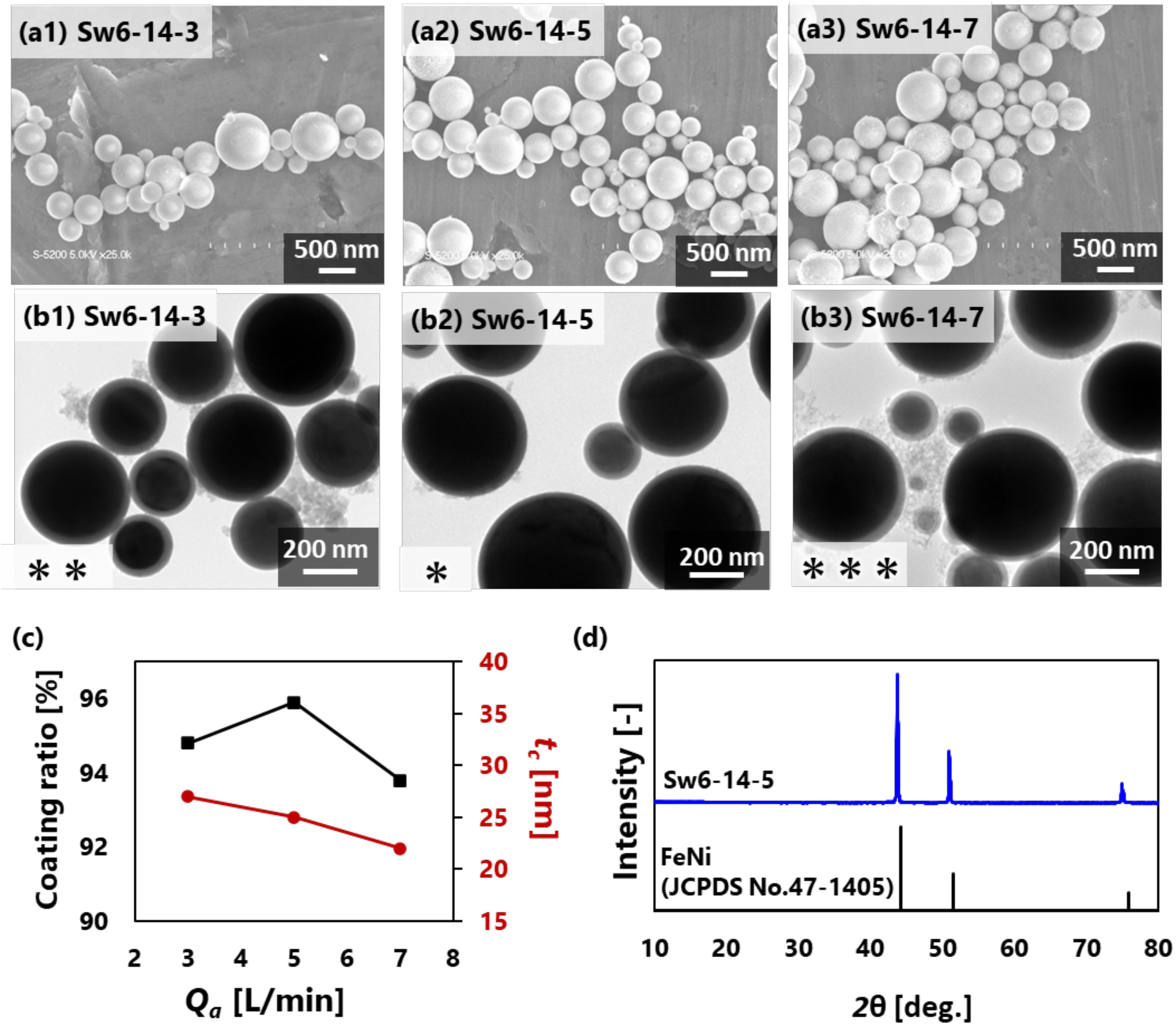

Figure 4.4. Effect of additional gas flow rates on the morphology of FeNi@SiO_2 particles. (a) SEM images and (b) TEM images of the applied Q_a: 1) 3 L/min, 2) 5 L/min, 3) 7 L/min, (Number of * indicate the level amount of nanoparticles). (c) Effect of the additional gas flow rates on the coating ratio (CR) and shell thickness (t_c). (d) XRD pattern of the FeNi@SiO_2 particles (Sw6-14-5).

By measuring the shell thickness and FeNi@SiO_2 particle size distribution from approximately 400 particles in the TEM images, the shell thickness shown in **Figure 4.4(c)** confirms that the higher Q_a allows for a thinner SiO_2 shell due to the lower concentration of HMDSO in the fluid flow and shorter residence time in the reactor. The Q_a variation at 3, 5, and 7 L/min resulted in shell diameters of 27, 25, and 22 nm, respectively. The shell thickness was also considered to proportionally affect the diameter of the FeNi@SiO_2 particles. A slight difference in the geometric mean diameter of the particles and the geometric standard deviation

($d_{av,g}/\sigma_{d,g}$), which were 361 nm/1.54, 353 nm/1.49, and 350 nm/1.60 as Q_a increased from 3 to 7 L/min are described in **Figure C.S5**. Based on the CR calculation, the level amount of the nanoparticle generation was inversed relatively to the percentage of the CR. Hence, the sample of Sw6-14-5 was the best to obtain the highest CR of 95.9% compared with the sample of Sw6-14-3 and Sw6-14-7 with CRs of 94.8% and 93.1%, in turn.

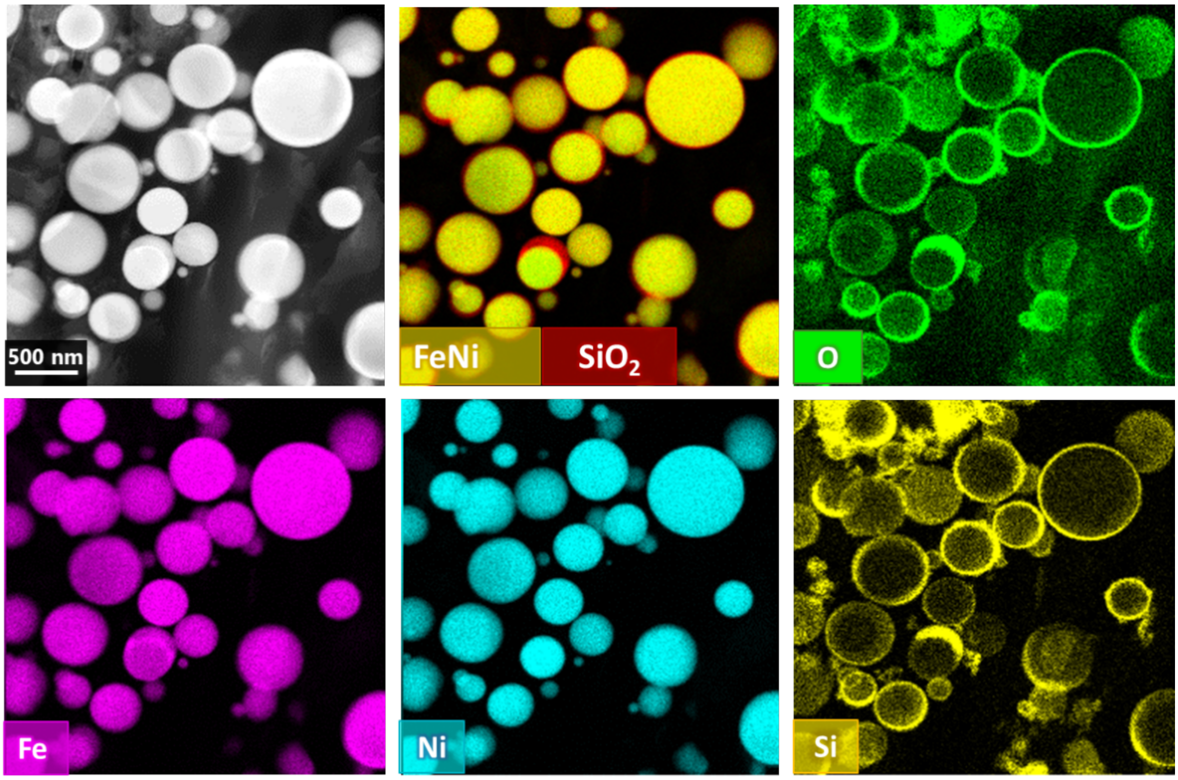

Figure 4.5. HAADF-STEM image and elemental mapping of cross-sectional FeNi@SiO_2 particles (Sw6-14-5).

The crystal structure analysis of the sample Sw6-14-5 also demonstrated the successful synthesis of FeNi as the core of the particle. The XRD pattern in **Figure 4(d)** revealed an FeNi crystal structure without oxidized iron or nickel peaks. It denoted that the reduction process proceeded completely. Cross-sectional HAADF-STEM analysis was used to further verify the structure of the synthesized particle. The core-shell FeNi@SiO_2 particles without the composite FeNi/SiO_2 formation are represented in **Figure 5**. The EDS mapping on the cross-section of the particles revealed the FeNi core without its oxidation state and the shell of SiO_2. The image was also dominated by the presence of FeNi@SiO_2 particles with a few uncoated particles, corresponding to the coating ratio calculation from the TEM images (**Figure 4 (b2)**).

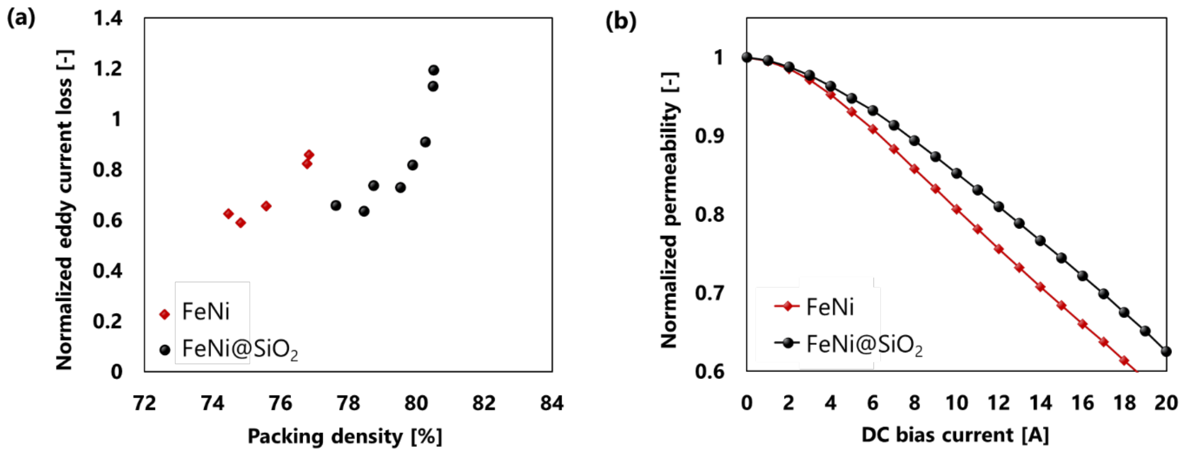

Figure 4.6. (a) Normalized eddy current loss in various packing densities, and (b) deterioration of the normalized permeability value of the applied FeNi and FeNi@SiO_2 particles in a powder core.

The effectiveness of the FeNi@SiO_2 particles was revealed by incorporating the particles into a powder magnetic core. The eddy current loss measurement was conducted by different packing density. Comparing the application of FeNi@SiO_2 and FeNi particles in the powder core, the FeNi@SiO_2 particles resulted in a lower eddy current loss at the same packing density (**Figure 4.6(a)**). It proved that the silica shell may suppress the inter-particle eddy current throughout the powder magnetic core.[9] Critically, at the same level of eddy current loss value, the FeNi@SiO_2 particles provided a higher packing density than that of the FeNi particles. The packing density is a crucial parameter in obtaining prominent DC bias characteristics[6] which is described by the declination in the normalized permeability value in the powder cores along with the electric current improvement (**Figure 4.6(b)**). The DC bias characteristic was represented by the I_{sat} value as the saturation point determined by 30% deteriorating value of the relative permeability. The use of FeNi@SiO_2 particles could maintain the deterioration of relative permeability at higher DC bias currents than the use of FeNi particles. The I_{sat} value obtained using FeNi@SiO_2 particles was 17.0 A, whereas the value obtained using uncoated FeNi was 14.3 A. It can be concluded that FeNi@SiO_2 particles were substantially more effective than FeNi particles, as the secondary particles in a powder magnetic core.

5.1 Conclusion

A single-step production of FeNi@SiO_2 particles was successfully performed using a connector-assisted spray pyrolysis method with different types of connectors. The effect of the connector geometries, i.e. T-shaped, Swirler-3, or Swirler-6 types, was firstly investigated by means of the particle characteristics. The TEM images demonstrated the coating quality of the FeNi@SiO_2 particles by calculating the number of coated particles percentage as the CR and observing the level amount of the undesired nanoparticle generation. Notably, the connector geometry exhibited a crucial role in the coating quality. Swirler-6, a swirler connector, revealed the most prominent type for introducing HMDSO vapor to the FeNi aerosol with the highest CR value of 95.9% and the lowest level of nanoparticle generation. According to the CFD simulation, the uniform dispersion between FeNi aerosol and HMDSO vapor is critical for heterogeneous nucleation, resulting in a high coating ratio percentage and a small number of generated nanoparticles. Furthermore, the effect of additional gas flow rates (Q_a) was investigated by varying the Q_a of 3, 5, and 7 L/min. Although the increase in the Q_a from 3 to 5 L/min resulted in a more evenly distributed HMDSO vapor, which improved the coating quality, further increasing the Q_a to 7 L/min resulted in a lower coating quality due to insufficient residence time and adjacent space among FeNi aerosol and generated SiO_2. The efficiency of the produced FeNi@SiO_2 particles from the most optimum condition in this experiment was then evaluated through magnetic characterization of the powder core. The use of the FeNi@SiO_2 particles as the secondary particles exhibited a remarkable benefit in the DC bias characteristics and eddy current loss value compared with uncoated FeNi particles.

Acknowledgements

This work was supported by JSPS KAKENHI Grant Number 19H02500. This work is partly supported by the International Network on Polyoxometalate Science at Hiroshima University, the JSPS Core-to-Core Program, the Information Center of Particle Technology, Japan, and the Hosokawa Powder Technology Foundation. We would like to thank the Ministry of Education, Culture, Sports, Science and Technology (MEXT) of Japan for providing a doctoral scholarship to E. L. S. We thank Dr. Makoto Maeda of the Natural Science Center for Basic Research and Development (N-BARD) at Hiroshima University for TEM observations and discussion. We also thank to enago (https://my.enago.com/) for editing a draft of this manuscript.

Chapter 5

Conclusions and Future Perspective

5.1 Conclusions

The advanced soft-magnetic material such as FeNi particles has contributed to the development of power converter component for realizing sustainable development goals. The manufacturing spherical submicron-sized iron nickel (FeNi) and silica-coated iron nickel (FeNi@SiO_2) particles in a direct, benign, and an effective process has been successfully conducted via spray pyrolysis method. Various harmless reduction agents, temperatures, and precursor carrier gas flow rates were investigated to obtain the FeNi particles with the spherical shape, dense structure, smooth surface, and absence of its oxide. It was found that these parameters are of importance for controlling the FeNi particles characteristics. In general, the higher reduction atmosphere provided by the reduction agents and the longer particles residence time owing to the lower carrier gas flow rates is favor of the targeted FeNi particles. In terms of FeNi@SiO_2 particles production, it was pointed that the equipment design plays an important role in obtaining the particles with high coating quality because it mainly controls the mixing between FeNi core and SiO_2 shell during coating process. Besides, a numerical approach based on computational fluid dynamics was conducted to propose a plausible particles formation. The highlighted conclusions in this thesis are listed as follows:

1. Submicron-sized FeNi particles were prepared by utilizing ethanol, ethylene glycol, and formic acid as harmless and low-cost reduction agents. The effectiveness of reduction agents was evaluated across a concentration range of 0-30 vol%. It was found that the type and concentration of reduction agents play a crucial role in determining the characteristics of FeNi particles. Ethanol and ethylene glycol, at higher concentrations (25 vol%), yielded smooth and spherical FeNi particles of submicron size. On the other hand, formic acid resulted in irregularly shaped particles with a Janus structure, comprising FeNi and FeO. A plausible mechanism for the reduction of metal salts was proposed, indicating that the type of reduction agent not only affects the extent of reduction but also influences the morphology of the particles during the synthesis process.

2. For the first time, submicron-sized FeNi particles have been applied as the secondary particles of a powder core inductor. The characteristics of FeNi particles are significantly influenced by process parameters in spray pyrolysis method, specifically temperature and carrier gas flow rates. Higher temperatures and lower carrier gas flow rates result in denser FeNi particles, transforming them from low-density to high-density structures. Whereas lower carrier gas flow rates yield a higher proportion of dense particles, a narrower particle size distribution, and an increased crystallite diameter. The densification process proves advantageous for incorporating FeNi particles as secondary materials in powder cores. The denser and smaller FeNi particles demonstrate improved performance in terms of DC bias characteristics and effectively distribute non-magnetic regions adjacent to them.
3. The one-step synthesis of FeNi@SiO_2 particles was carried out by using connector-assisted spray pyrolysis as a new approach. It was revealed that the connector types significantly affected to the coating quality of FeNi@SiO_2 particles. Swirler type connector, i.e., Swirler-6, resulted the highest coating ratio and the lowest free SiO_2 nanoparticles because this connector can maintain intense mixing between FeNi and SiO_2 sources. Computational fluid dynamics (CFD) was performed to understand the plausible coating phenomenon. The resulted FeNi@SiO_2 particles was applied for the secondary particle of a powder core. It showed that the FeNi@SiO_2 particles enhanced the magnetic characteristic of the powder core inductor.

It is noteworthy that the utilization of the FeNi and FeNi@SiO_2 particles enhances the magnetic characteristic of a powder core inductor, which promises a better performance for the advancement digital and electric machines.

5.2 Suggestion for further investigations

1. A numerical approach based on population balance model should be conducted to understand the more plausible mechanism of FeNi@SiO_2 particles formation. Other possibilities of the formation of FeNi@SiO_2 particles such as the scavenging of SiO_2 particles onto FeNi particles during in-flight or the diffusion of SiO_2 source into the FeNi source followed by the particles drying that starts from the formation of SiO_2 shell to the FeNi core.

2. Controlling SiO_2 shell thickness is critical for the wide application of the FeNi@SiO_2 particles. A precise control over the SiO_2 shell thickness allows for optimization of the particle's magnetic and electrical properties. Thicker shells can provide better insulation and protection, minimizing interactions between the FeNi core and the surrounding environment. This is particularly important in applications where the particles are exposed to harsh conditions, such as high temperatures, humidity, or corrosive substances.
3. In order to precisely control the silica shell thickness on the FeNi particles, it is strongly suggested to perform an experiment to get the number of precursor droplet provided by ultrasonic nebulizer since the number of core particles would determine the coating performance. There is a minimum number of droplet that could prevent the homogeneous nucleation.
4. Direct synthesized silica-coated Fe particles (Fe@SiO_2) can be considered by using spray pyrolysis for further powder core inductor development. To the best of my knowledge, there is no study that successfully produced Fe@SiO_2 particles in one-step process and apply it for a power converter component. It is believed that the Fe@SiO_2 particles can provide a better magnetic characteristic on a powder core compared to FeNi@SiO_2 particles owing to the higher magnetic saturation value of Fe over FeNi.

Appendix. A

Supporting Information: Direct synthesis of submicron FeNi particles via spray pyrolysis using various reduction agents

A.1 Effect of the temperature on the crystallite structure of FeNi particles in the absence of reduction agents

The synthesis of FeNi particles by spray pyrolysis was conducted using a controllable electric furnace at a constant temperature. The temperature is monitored using thermocouples inside the tube (see **Figure A.S1**).

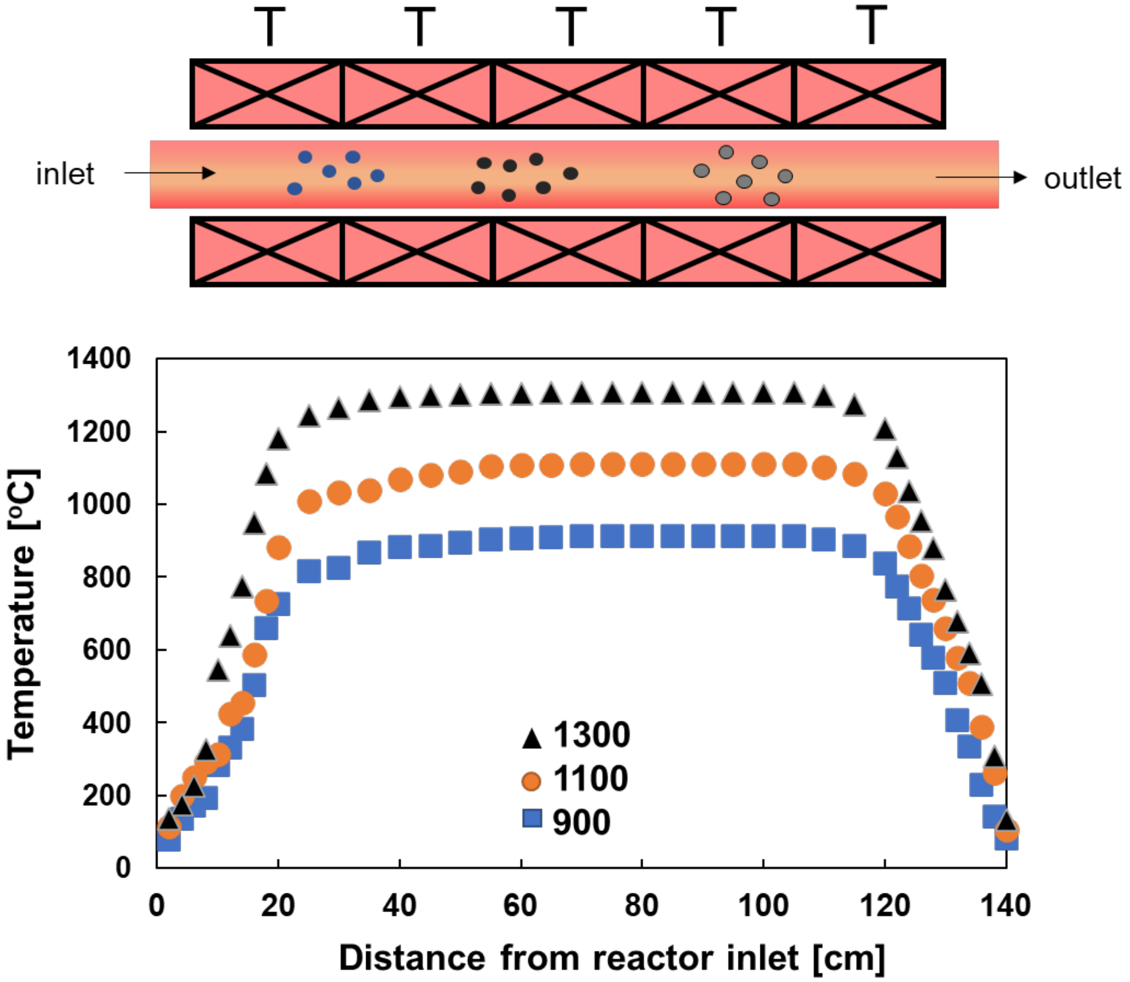

Figure A.S1. Temperature distribution inside spray pyrolysis reactor.

To find the optimum temperature for producing FeNi particles, preliminary experiments were performed in the absence of reduction agents between 900 and 1300°C. The crystal structures of the products were analyzed using XRD, shown in **Figure A.S2**. This figure depicts iron nickel oxide ($Ni_xFe_{3-x}O_4$) and nickel oxide (NiO) as the main product in the samples of W100_9 and W100_10. This indicates that temperatures of 900 and 1000°C are insufficient to reduce the oxidation state of this metal. Slightly increasing the temperature to 1100°C produces three main peaks of face centered cubic (*fcc*) suggesting FeNi crystals appearing in small amounts (sample W100_11). The FeNi crystal structure further increases at the applied temperatures of 1200 and 1300°C. However, it is noticeable that the crystal phases between W100_12 and W100_13 have little difference.

Table A.S1. Experimental conditions of the preliminary experiments.

Sample name	Solvent-Reduction agent	Reduction agent concentration (vol%)	Temperature (°C)
W100_9	Water (W)	0	900
W100_10			1000
W100_11			1100
W100_12			1200
W100_13			1300
ET25_11	Water-Ethanol (ET)	25	1100

The increase of the intensity of FeNi as well as Fe_3O_4 and $Fe_{1-x}O$ crystals correspond to the increase in temperature. Inversely, the peak of the $Ni_xFe_{3-x}O_4$ and NiO decrease with temperature. This phenomenon is in accordance with the following reaction of thermal decomposition and reduction [108–110,160,161].

$$Fe(NO_3)_3.9H_2O \rightarrow Fe(OH)_2.NO_3 + H_2O + HNO_3 \rightarrow Fe_2O_3 + NO_2 + O_2 + H_2O \quad (A.1)$$

$$Ni(NO_3)_2.6H_2O \rightarrow Ni(OH).NO_3 + H_2O + HNO_3 \rightarrow NiO + NO_2 + O_2 + H_2O \quad (A.2)$$

$$Fe_2O_3 + NiO \rightarrow Ni_xFe_{3-x}O_4 \quad (A.3)$$

$$Fe_2O_3 \rightarrow Fe_3O_4 \quad (A.4)$$

$$Ni_xFe_{3-x}O_4 \rightarrow NiO + Fe_3O_4 \rightarrow Ni + Fe_3O_4 \rightarrow Fe_{1-x}O + FeNi \quad (A.5)$$

The XRD pattern between W100_12 and W100_13 proves that the conversion of FeNi cannot be completed because of the water adsorption at the iron oxide and FeNi interface of the particles [116]. Therefore, the FeNi particle synthesis in various reduction agents is conducted at the temperature of 1200°C.

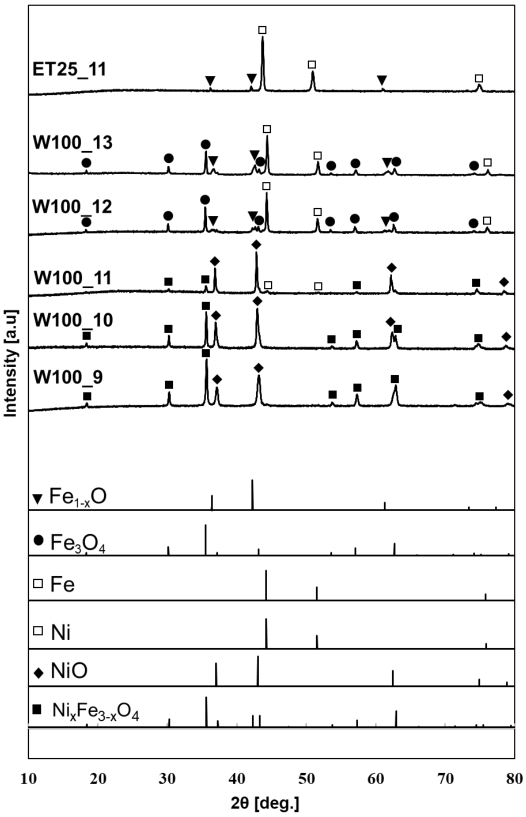

Figure A.S2. XRD pattern of FeNi particles using water as a solvent at various temperatures.

A.2 Effect of the reduction agent concentration on the crystallite structure of FeNi particles

The crystal structure of the fabricated FeNi particles in the different reduction agents was confirmed using XRD (**Figure A.S3**). The crystal structure of FeNi and $Fe_{1-x}O$ were recognized at lower concentrations of ethanol and ethylene glycol (sample ET10, ET15, EG10, EG15). Meanwhile, increasing the concentration of these reduction agents yielded FeNi particles with no oxidation state in the samples of ET25, ET30, EG25, EG30. Conversely, formic acid produced samples of FA10 to FA30 with the presence of FeO (e.g., Fe_3O_4 and $Fe_{1-x}O$) at all tested concentrations.

A.3 Effect of the temperature on the morphology of FeNi particles in the absence of reduction agents

The morphology of the product in 100 vol% of water was confirmed using SEM at various temperatures shown in **Figure A.S4**. This figure reveals that the applied temperature significantly affects the morphology of the particles. At 900°C, rough and spherical particles were obtained. Particle formation becomes more spherical as the temperature is increased

1000°C (**Figure A.S4(a), (b)**). Meanwhile, heterostructure particles with whisker formation (fibrous iron metal growth over the iron oxide) occurred at 1100°C (**Figure A.S4(c)**). These whiskers are generally formed by the nucleation of iron on the iron oxide surface during reduction in a H_2 gas atmosphere [162].

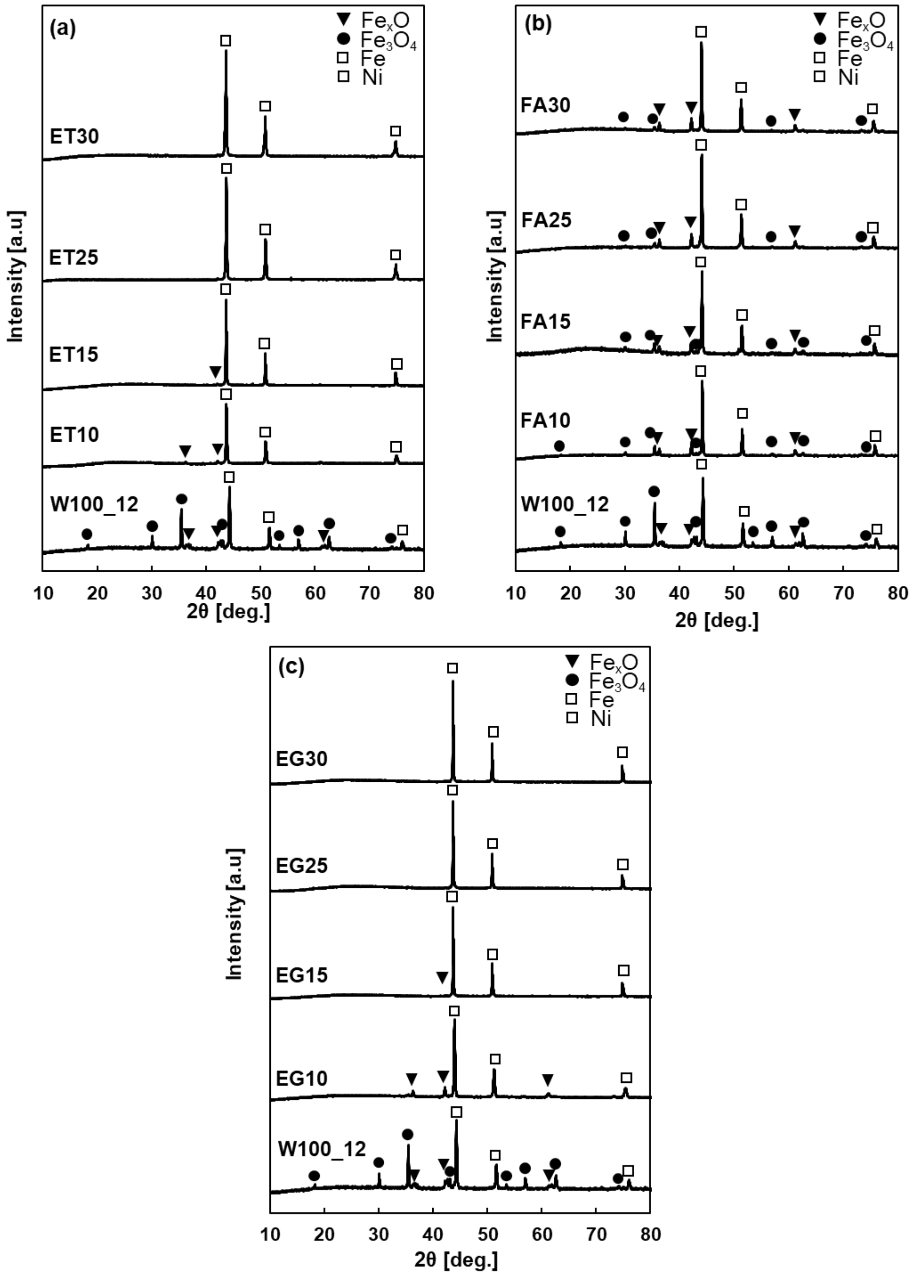

Figure A.S3. Crystal structure of FeNi particles synthesized using (a) Ethanol, (b) Formic acid, (c) Ethylene glycol.

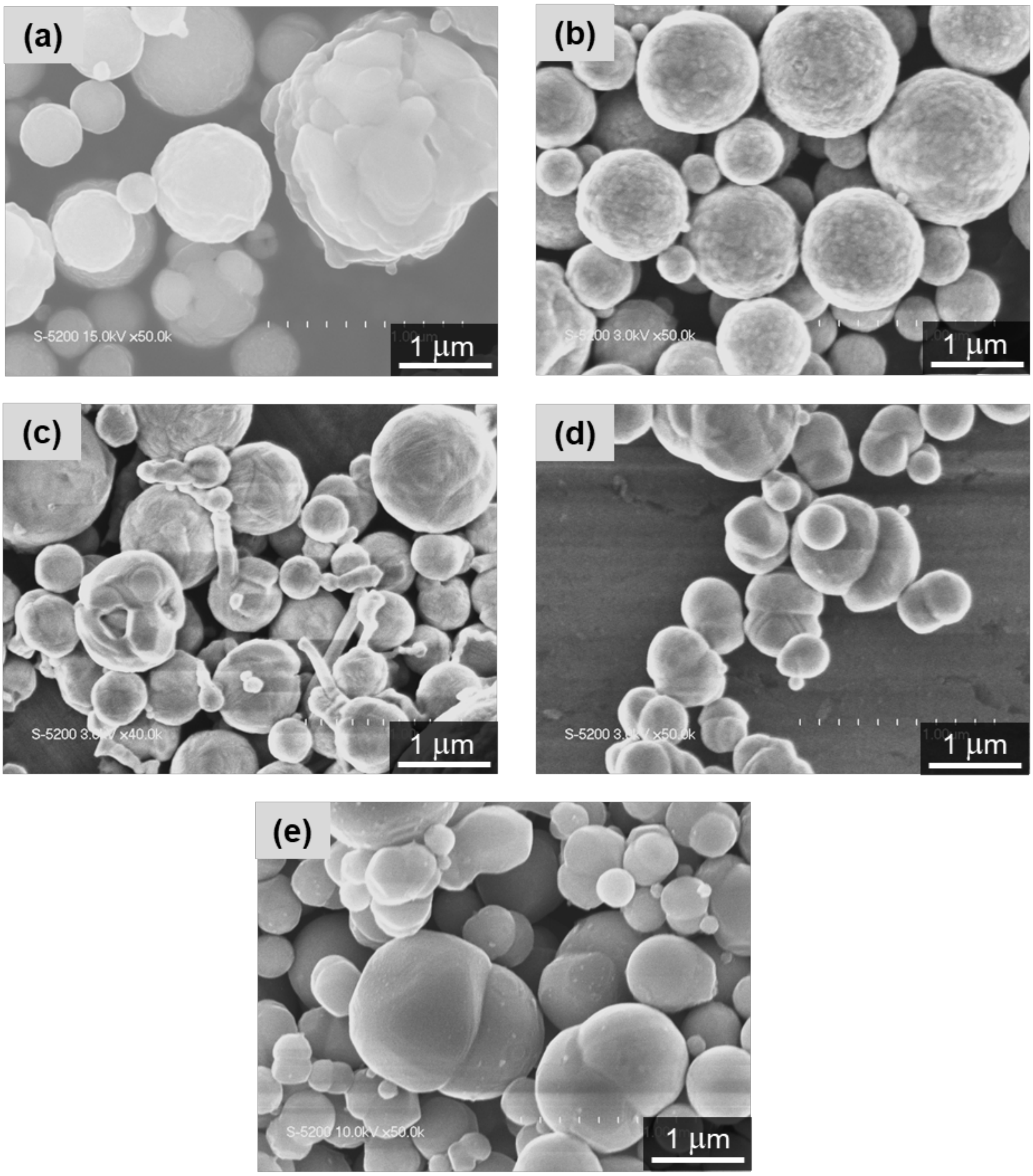

Figure A.S4. SEM images of FeNi particles synthesized using water as a solvent in various temperatures (a) 900 °C, (b) 1000 °C, (c) 1100 °C, (d) 1200 °C, (e) 1300 °C.

A further increase in temperature to 1200°C might encourage particle sintering [163] (**Figure A.S4(d)**) and the driving force of reduction by H_2 gas thermodynamically and kinetically according to the Baur-Glassner diagram. Accordingly, dense formations of the Fe phase on the iron oxide surface were generated. However, increasing the temperature to 1300°C in **Figure A.S4 (e)** showed an insignificant difference to particle morphology and crystal structure (**Figure A.S2**). Although this temperature increases the reduction driving force, the water vapor from the reduction reaction, and causes H_2O partial pressure build up in the gas mixture. Consequently, these water molecules can be absorbed at the free reaction sites of iron and iron oxide, which blocks the further progress of reduction and decelerates the iron nuclei growth rate.

The crystal structure of ET25_11 at 1100°C is shown in **Figure A.S2**, and iron oxide is still generated at this temperature because of insufficient energy. This result supports that the temperature should be 1200°C for this study of the effect of reduction agents on FeNi particle formation.

A.4 Particle size distribution of the case of 25 vol% reduction agents

The reduction agent types lead to the precursor properties such as density, viscosity, and surface tension which affected the particle size distribution as presented in the **Table A.S2** and **Figure A.S5**, respectively.

Table A.S2 Precursor properties in different solvents

Property of $Fe(NO_3)_3$ and $Ni(NO_3)_2$ solution	in water	in 25 vol% ethanol-water	in 25 vol% formic acid-water	in25 vol% ethylene glycol-water
surface tension (mN/m)	74.2	39.3	56.45	63.55
density (kg/m^3)	1134	1109.5	1218.5	1185.4
viscosity (Pa.s)	0.0010	0.0020	0.0012	0.0022

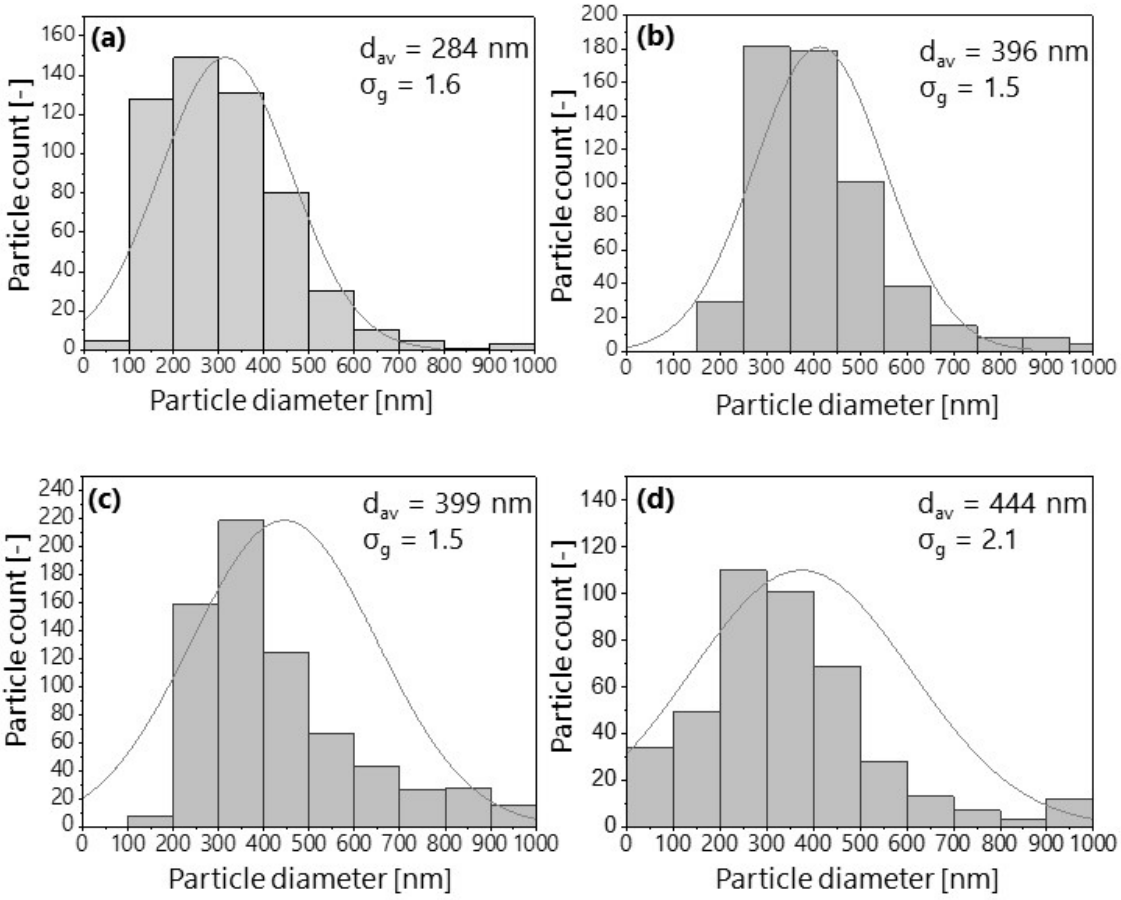

Figure A.S5. Effect of the solvent type on the FeNi particle size distribution: (a) 25 vol% ethanol, (b) 25 vol% formic acid, (c) 25 vol% ethylene glycol, and (d) water. d_{av} is the geometric mean diameter, σ_g is the geometric standard deviation.

A.5 Atomic distribution of the particle with the spherical and Janus structure

To confirm the atomic distribution and chemical composition in the particle, EDS analysis is conducted (**Figure A.S6**). The Janus structure resulted from formic acid showed that the particles comprise different chemical structures that belong to FeNi at position 2 and FeO (Fe_3O_4 and $Fe_{1-x}O$) at position 1. Conversely, the spherical particles generated by ethanol indicate FeNi only (position 3).

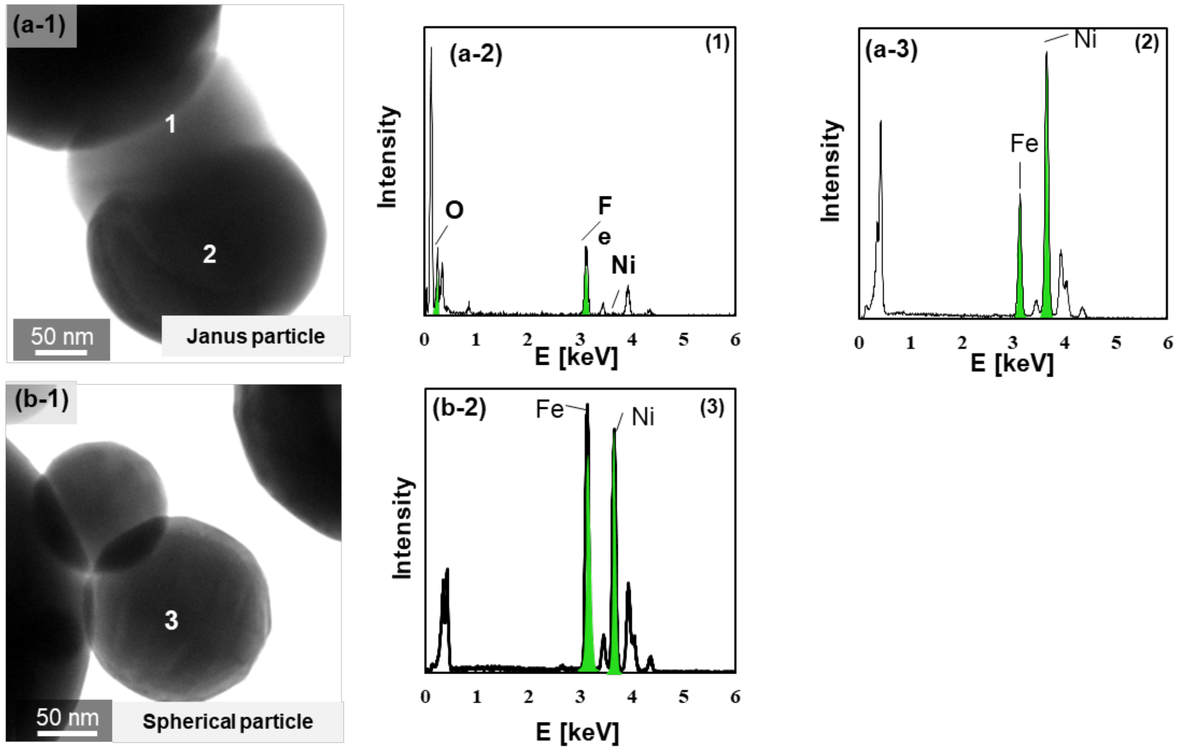

Figure A.S6. EDS analysis of (a) the Janus structure (FA25) and (b) the spherical structure (ET25).

A.6 Thermogravimetric analysis and thermal decomposition of the solid precursor

Figure A.S7 shows thermal decomposition and metal salt reduction using thermogravimetric analysis (TGA) under 5% H_2-N_2 with a heating rate of 10 °C/min. Water evaporation is confirmed by the first mass loss. Then, further increases in temperature represent the precipitation of $Fe(OH)_2.NO_3$ and $Ni(OH).NO_2$. Moreover, the precipitated solids are decomposed into Fe_2O_3 and NiO at 250°C [3]. Furthermore, the reaction between Fe_2O_3 and NiO occurs to generate $Ni_xFe_{3-x}O_4$ following equation (1) – (3). Finally, the $Ni_xFe_{3-x}O_4$ is reduced to FeNi, which is confirmed by 17 wt% of the remaining weight and the silver metallic color of the final product.

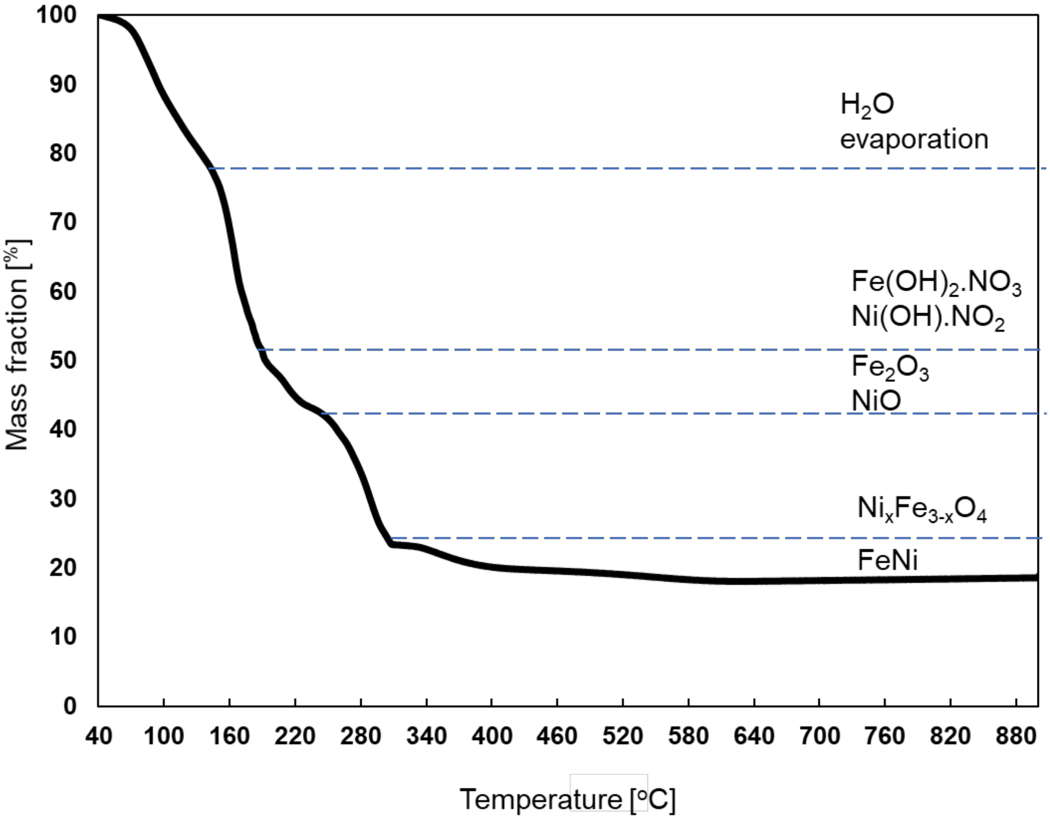

Figure A.S7. Thermogravimetric analysis of the solid precursor**.**

Additionally, to prove the polyol mechanism in the ethylene glycol case, a thermal decomposition test is performed by evaporating the four precursor solutions at 200°C in air. The separated color of the precipitated solid caused by the ethylene glycol is evidence of the different precipitation of $Fe(OH)_2.NO_3$ and $Ni(OH).NO_2$ in comparison to the others (**Figure A.S8**).

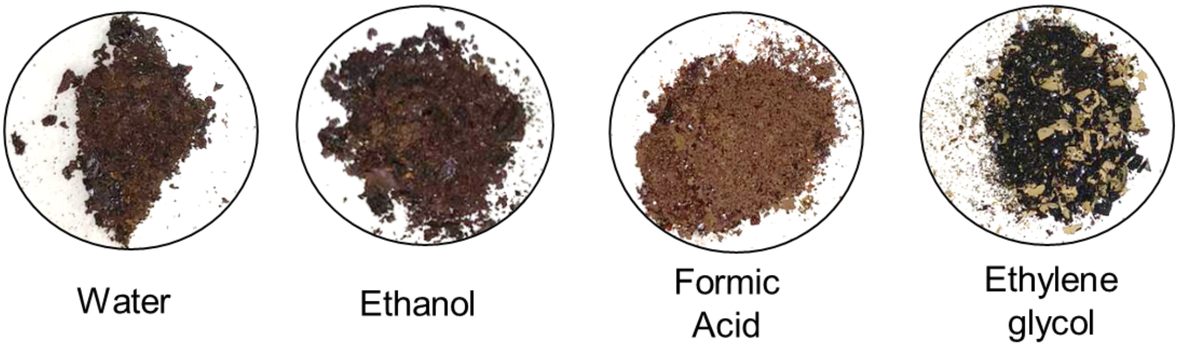

Figure A.S8. The precipitated solid of the precursor solutions at 200°C under the air.

A.7 Reduction agent decomposition by Computational Fluid Dynamics

To better understand FeNi particle formation, a simulation of ethanol decomposition was conducted using a Computational Fluid Dynamics (CFD) approach. The simulation was conducted over the volume of the spray pyrolysis reactor. The domain was divided into 147,000 mesh with an average skewness of 0.14 and the orthogonal quality of 0.98. The momentum transport was modelled by Reynold Average Navier Stokes (RANS), k-ε model (equation (A.6) to (A.8)). Furthermore, the ethanol decomposition was assumed by the main reaction. It was described by the local mass transport model (equation (A.9)) from each species (Y_i).

$$\frac{\partial}{\partial t}(\rho k)+\frac{\partial}{\partial x_i}(\rho k u_i)=\frac{\partial}{\partial x_j}\left[\left(\mu+\frac{\mu_t}{\sigma_k}\right)\frac{\partial k}{\partial x_j}\right]+G_k+G_b-\rho\varepsilon-Y_M+S_k \tag{A.6}$$

$$\frac{\partial}{\partial t}(\rho\varepsilon)+\frac{\partial}{\partial x_i}(\rho\varepsilon u_i)=\frac{\partial}{\partial x_j}\left[\left(\mu+\frac{\mu_t}{\sigma_\varepsilon}\right)\frac{\partial \varepsilon}{\partial x_j}\right]+C_{1\varepsilon}\frac{\varepsilon}{k}(G_k+C_{3\varepsilon}G_b)-C_{2\varepsilon}\rho\frac{\varepsilon^2}{k}+S_\varepsilon \tag{A.7}$$

$$G_k=-\rho\overline{u_i'u_j'}\frac{\partial u_j}{\partial x_i} \tag{A.8}$$

$$\frac{\partial}{\partial t}(\rho Y_i)+\nabla\cdot(\rho\bar{v}Y_i)=-\nabla\cdot\bar{J}_i+R_i+S_i \tag{A.9}$$

Turbulent or eddy viscosity calculated by $\mu_t=\rho C_\mu\frac{k^2}{\varepsilon}\mu_t.C_\mu$ is constant 0.09. $C_{1\varepsilon}, C_{2\varepsilon}$ are 1.44, 1.92; $\sigma_k, \sigma_\varepsilon$ are the Prantdl Numbers 1, 1.3; S_ε, S_k are user defined sources. R_i is the net rate of production of species i by chemical reaction and S_i is the rate of creation by addition from the dispersed phase plus any user-defined sources. An equation of this form will be solved for N−1 species where N is the total number of fluid phase chemical species present in the system. Because the mass fraction of the species must sum to unity, the Nth mass fraction is determined as one minus the sum of the N−1 solved mass fractions. To minimize numerical error, the Nth species should be selected as that species with the overall largest mass fraction, such as N_2 when the oxidizer is air [9]. The activation energy of H_2 gas generation from ethanol, formic acid, and ethylene glycol are 174 kJ/mol [10], 70.7 kJ/mol [11], 100 kJ/mol [12], respectively. The physical properties of all chemical components followed the Ansys Fluent database. Additionally, the density and the heat capacity of the ethylene glycol were defined at constant values of 2.1 kg/m^3 and 156.4 J/mol K [13], in turn. Meanwhile, the density and the heat capacity of the formic acid were 1.6 kg/m^3 and 97.91 J/mol K [14].

The simulation was validated by the temperature distribution at the center of the spray pyrolysis reactor and the characteristic of the ethanol decomposition product. **Figure A.S9(a)** describes that the simulation agrees with H_2, CO_2, and ethanol concentration [15]. Based on the simulation result of the ethanol case, the two stages are possible to be proposed in the FeNi particle formation. The first stage represents the mechanism on the evaporation and thermal decomposition of the precursor solution into Fe_2O_3 and NiO for the first 250°C. It is supported by the relatively low H_2 gas generated from ethanol decomposition at this temperature. Secondly, the reduction is the main mechanism producing FeNi particles during the second stage. It is confirmed by the relatively high concentration of H_2 gas along with the decrease of ethanol concentration throughout the reactor. **Figure A.S9 (b)** and **(c)** represent the simulation of the formic acid and ethylene glycol decomposition, respectively. The temperature and the mol fraction of the chemical components in all cases show so similar characteristic that the particle formation can be generalized into (i) evaporation and chemical reaction as well as (ii) reduction stages.

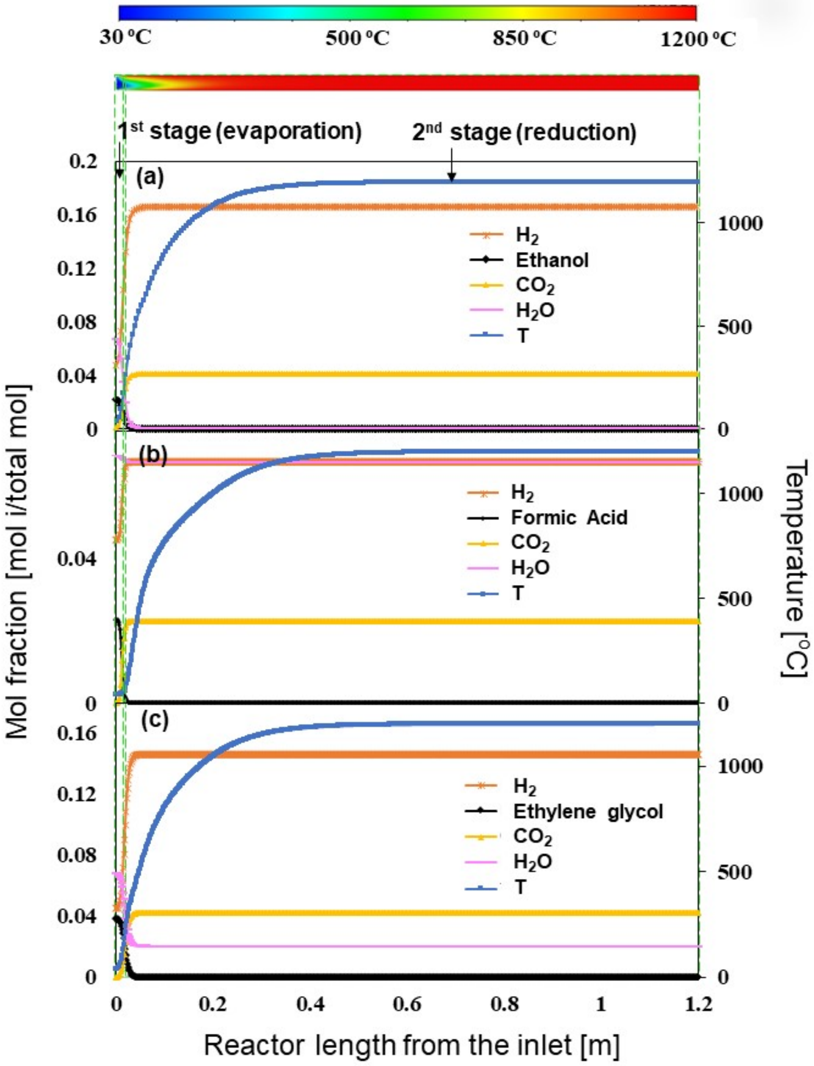

Figure A.S9. The reduction agent decomposition by Computational Fluid Dynamics simulation: (a) ethanol, (b) formic acid, (c) ethylene glycol

Appendix B

Supporting Information: DC bias characteristic enhancement of the powder core by using densified submicron sized FeNi particles through spray pyrolysis

B.1 Characteristics of FeNi particles in various precursor concentrations

In our previous report, the use of 25 vol% ethanol was useful to produce the spherical and submicron sized FeNi particles from its metal salt form. To increase the production rate, a preliminary experiment was conducted by applying various concentrations of the precursor solution, i.e., 0.2, 0.3, 0.4, and 0.6 mol/L. An increase of the solution concentration resulted in an increase of the metal oxide phase owing to an insufficient reduction agent. **Figure B.S1** shows spherical particles with the Fe and Ni atoms distributed uniformly from the precursor concentration of 0.2 mol/L, while Janus particles occurred in the two phases of FeNi and FeO from the precursor concentration of 0.6 mol/L. Consequently, the magnetic saturation flux density (B_s) value plummeted from 1.5 T to 0.9 T for the concentrations of 0.2 mol/L to 0.6 mol/L, as shown in **Figure B.S2**.

B.2 Measurement of the hollow percentage by TEM image

Particle count from TEM images was used to determine the hollow percentage of the resulting particles as presented in **Figure B.S3**. We calculated the number of particles at least 400 particles. The amount of hollow and dense particles are summarized statistically in **Figure B.S4**.

B.3 Gas chromatography analysis

To confirm carbon formation as a side effect of the ethanol decomposition, gas chromatography analysis was conducted by using a Shimadzu GC-14B (Shimadzu, Japan) gas chromatograph equipped with a split/spitless injector. The chromatograms were recorded and calculated by using a Shimadzu C-R8A (Shimadzu, Japan) computing integrator. The gas chromatography analysis shown in **Figure B.S5** depicts the gas composition in the flue gas from the fed solution droplet of 25 vol% ethanol into the spray pyrolysis reactor at 1200 °C.

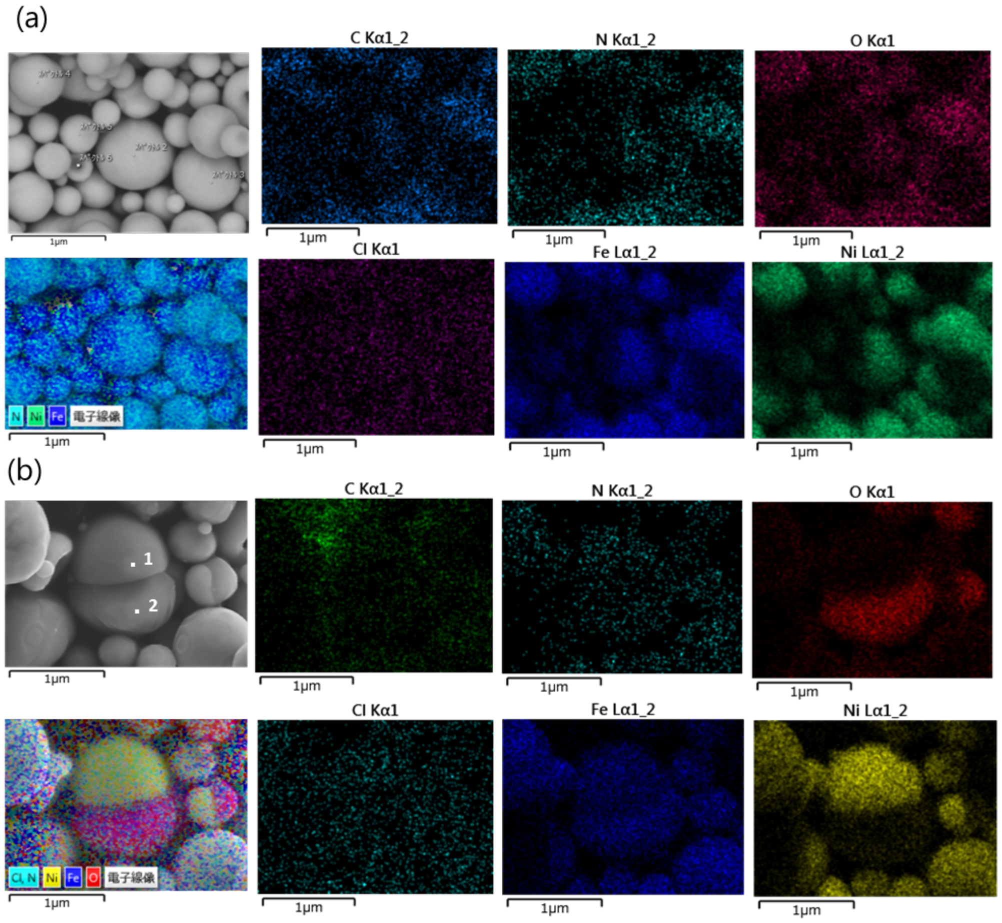

Figure B.S1. Elemental mapping of FeNi particles in different concentrations: (a) 0.2 mol/L; b) 0.6 mol/L.

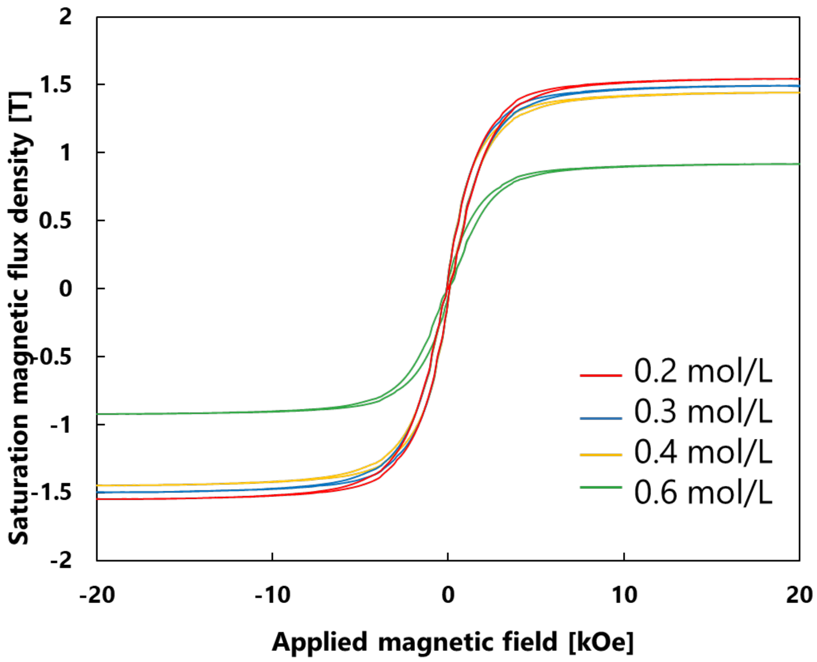

Figure B.S2. Magnetization characteristic of FeNi particles in various precursor concentrations.

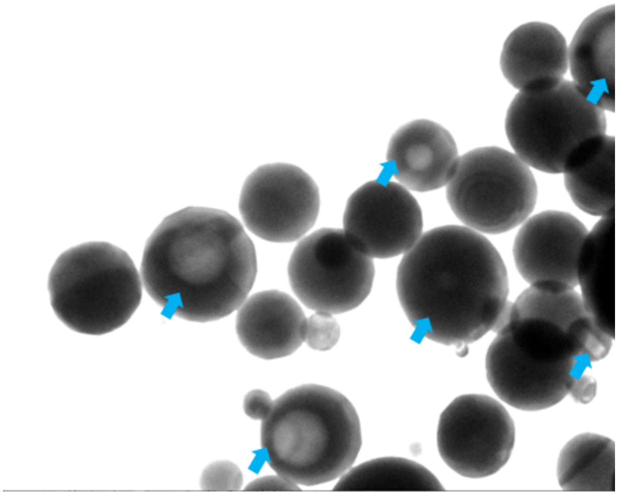

Figure B.S3. Calculating the hollow particle percentage from the TEM images. The blue arrow is indicating the hollow particles.

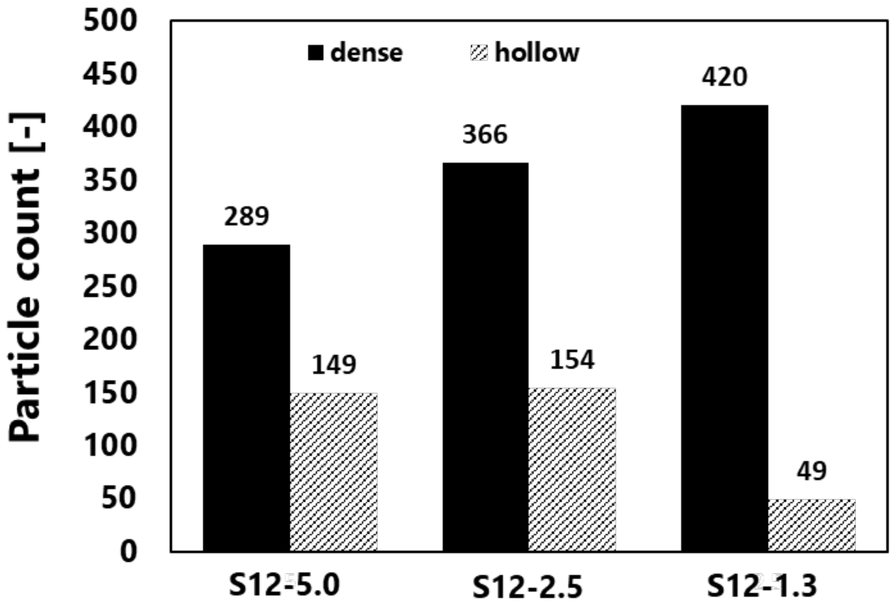

Figure B.S4. The bar chart of the dense and hollow FeNi particles count

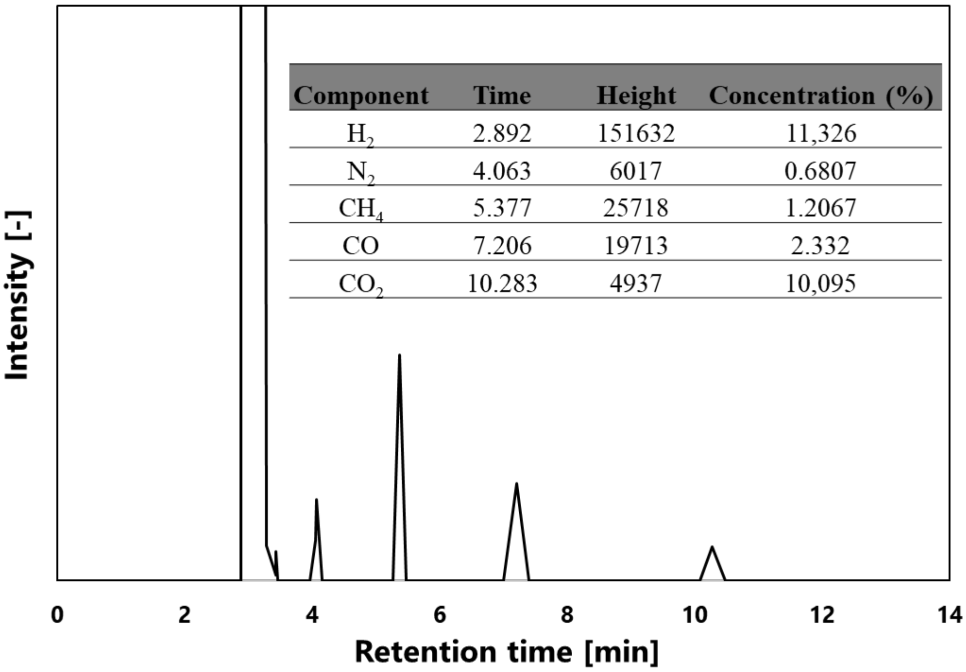

Component	Time	Height	Concentration (%)
H_2	2.892	151632	11,326
N_2	4.063	6017	0.6807
CH_4	5.377	25718	1.2067
CO	7.206	19713	2.332
CO_2	10.283	4937	10,095

Figure B.S5. Gas chromatography analysis of the flue gas from 25 vol% ethanol–water.

B.4 Confirmation of the *L*1$_0$ phase of FeNi particles

An XRD pattern at a low angle was used to validate the presence of the hard magnetic material characteristic, which was most likely present in the FeNi based material. All of our samples were absent of the *L*1$_0$ phase of FeNi particles, as shown in **Figure B.S6**.

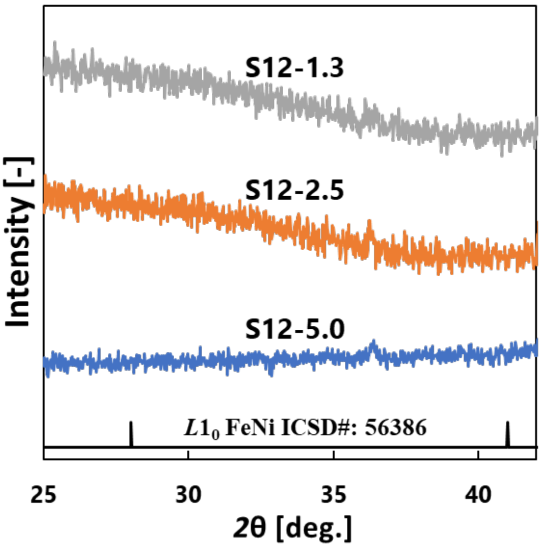

Figure B.S6. XRD pattern at a low angle of the submicron FeNi particles.

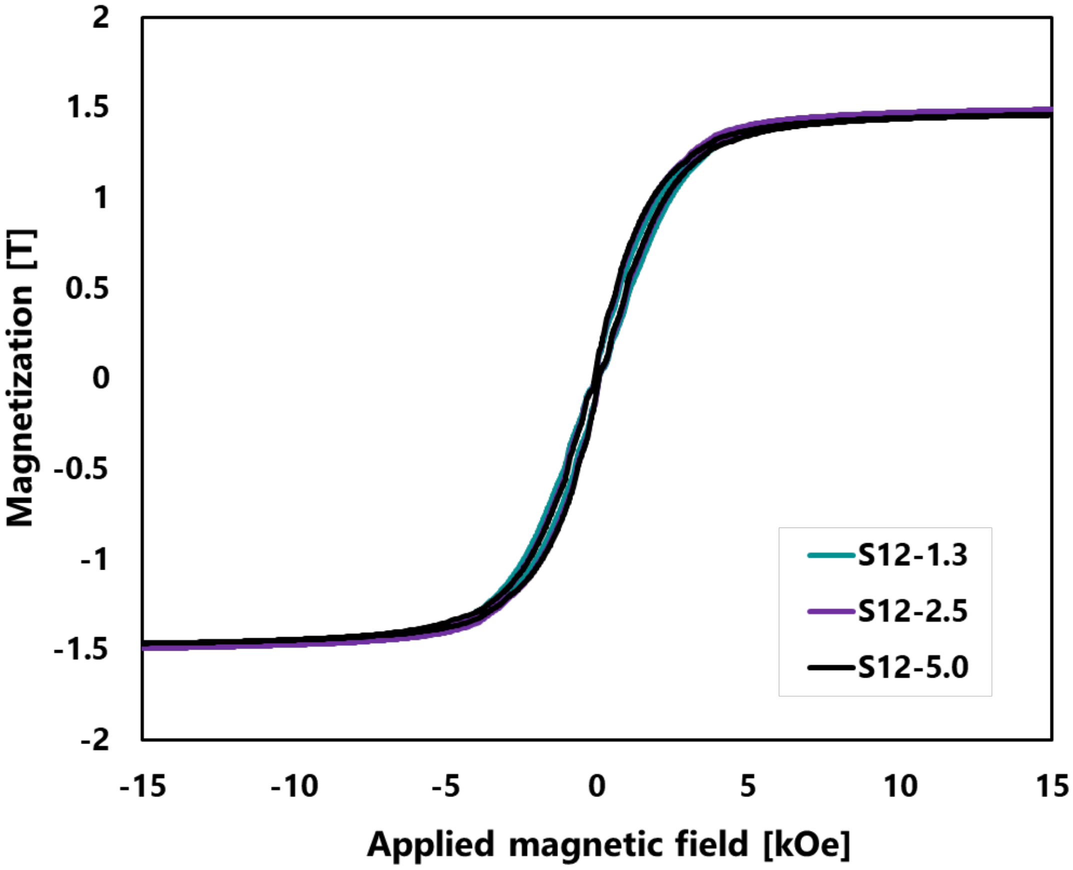

Figure B.S7. Hysteresis loop of FeNi particles in various carrier gas flow rates at 1200 °C.

B.5 Measurement of the adjacent non-magnetic region

The adjacent non-magnetic region was determined by measuring the distance between particles. The distance of each particle was measured in at least 4 directions, as shown in **Figure B.S8**, and then the average distance was calculated as the quantitative particle distance.

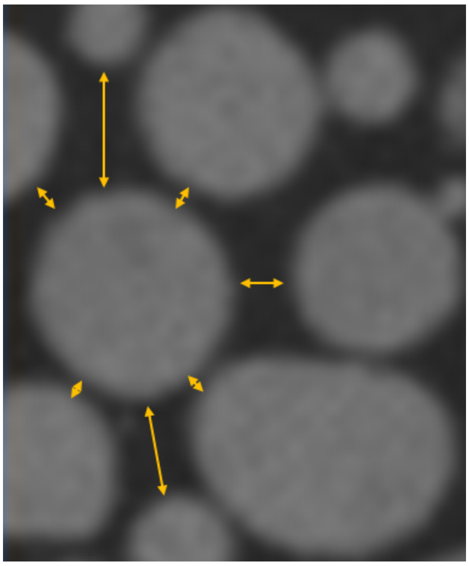

Figure B.S8. Schematic distance measurement for individual particles**.**

Appendix C

Supporting Information: One-step synthesis of SiO$_2$ coated FeNi particles by using swirler connector-assisted spray pyrolysis

C.1 Simulation-based on Computational Fluid Dynamics (CFD)

Because of the limitations in the experimental method, a CFD simulation was performed using Fluent, embedded in Workbench 2021 R1 (Student version). The calculation domain for each system, including the connector and reactor parts was made separately using Space claim and Meshing software. The meshing quality for each domain was maintained at approximately 250,000 mesh with a skewness below 0.25 and an orthogonal quality of 0.98. After considering the range of Reynold number of each system, between 210 and 4776, Shear-Stress Transport (SST) k-ω model was cconsidered to model the momentum transport[1] because it modified additional cross-diffusion terms in the ω equation and blending function to appropriately model the near-wall and far-field zones as follows:[2]

$$\frac{\partial}{\partial t}(\rho k) + \frac{\partial}{\partial x_i}(\rho k u_i) = \frac{\partial}{\partial x_j}\left(\Gamma_k \frac{\partial k}{\partial x_j}\right) + \widetilde{G_k} - Y_k + S_k \qquad \text{(C.1)}$$

$$\frac{\partial}{\partial t}(\rho \omega) + \frac{\partial}{\partial x_i}(\rho \omega u_i) = \frac{\partial}{\partial x_j}\left(\Gamma_\omega \frac{\partial \omega}{\partial x_j}\right) + \widetilde{G_\omega} - Y_\omega + D_\omega + S_\omega \qquad \text{(C.2)}$$

Where, $\widetilde{G_k}$ is the generation of turbulence kinetic energy due to mean velocity gradients, $\widetilde{G_\omega}$represents the ω generation. Γ_k, Γ_ω, Y_k, and Y_ω describe effective diffusivity of k and ω as well as dissipation of k and ω due to turbulence, respectively. D_ω is the cross-diffusion term, while the S_k and S_ω are user-defined source terms. Regarding the particle tracking model, it followed the Euler-Lagrangian approximation according to the low volume fraction of the dispersed second phase. The calculation of mass as well as heat exchange followed inert particle type as written in Eq. (3).

$$m_p c_p \frac{dT_p}{dt} = hA_p\left(T_\infty - T_p\right) \qquad \text{(C.3)}$$

Where m_p is the mass of the particle (kg), c_p is the heat capacity of the particle (J/kg.K), A_p is the surface area of the particles (m^2), T_∞ is the local temperature of the continuous phase (K), and h is the convective heat transfer coefficient (W/m^2.K).

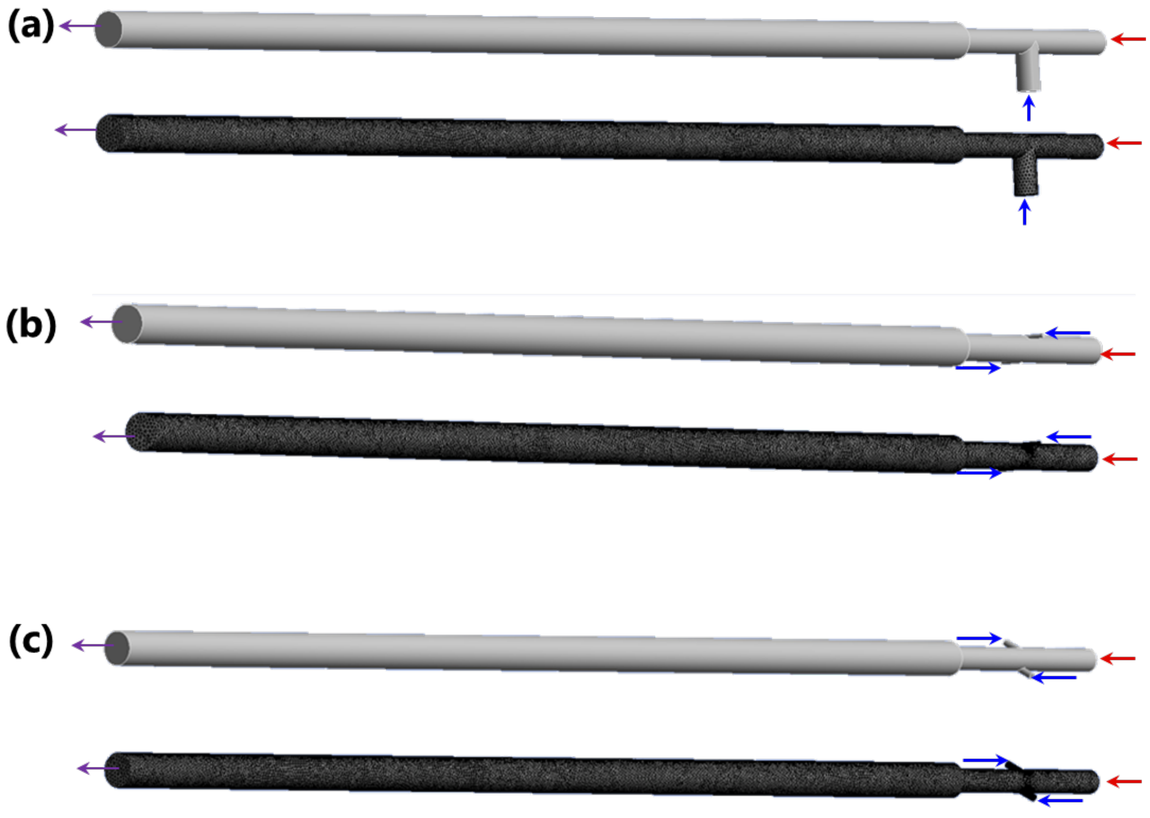

Figure C.S1. Geometry and geometry meshing of the connector and reactor parts in the use of different connector types: (a) T-shaped, (b) Swirler-3, (c) Swirler-6

C.2 CFD simulation results

According to the CFD-calculated temperature and the degradation of the HMDSO concentration as a function of length from the HMDSO vapor inlet, as shown in **Figure** C.**S2(a,b)**, the concentration of the HMDSO remained constant at the connector due to a low level of temperature. In a later, the HMDSO concentration declined as the temperature increased to approximately 900 K, indicating SiO_2 generation (**Figure C.S2)**.

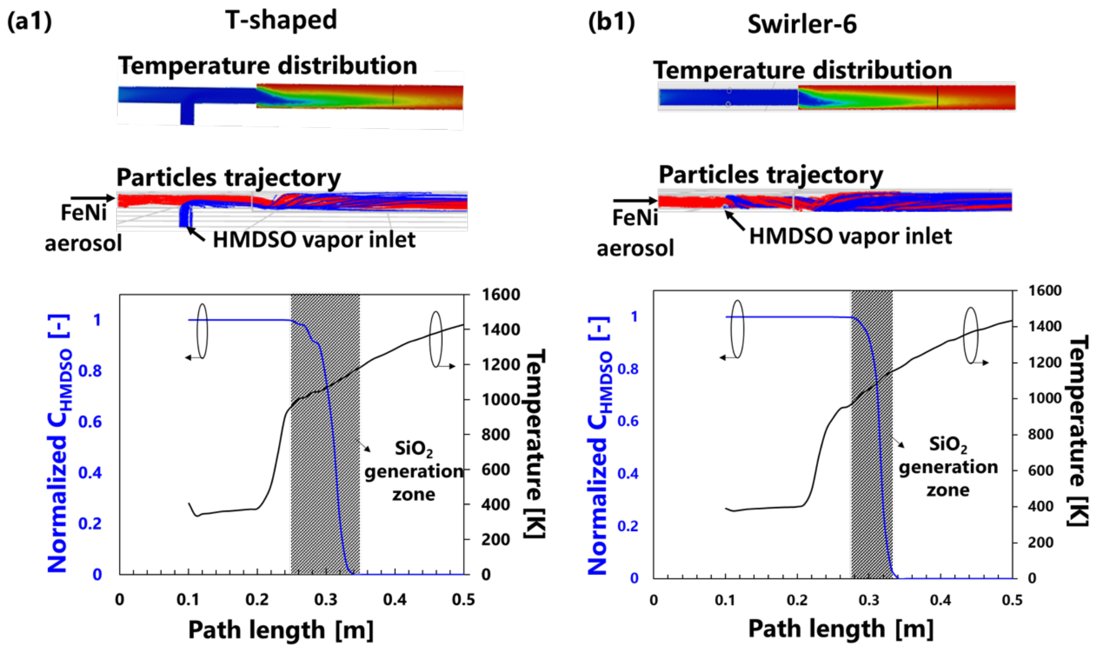

Figure S2. Temperature distribution, FeNi aerosol and HMDSO vapor trajectory, the plot of HMDSO concentration, and the temperature at the center as a function of length: (a) T-shaped (Ts-14-3), (b) Swirler-6 (Sw6-14-3)

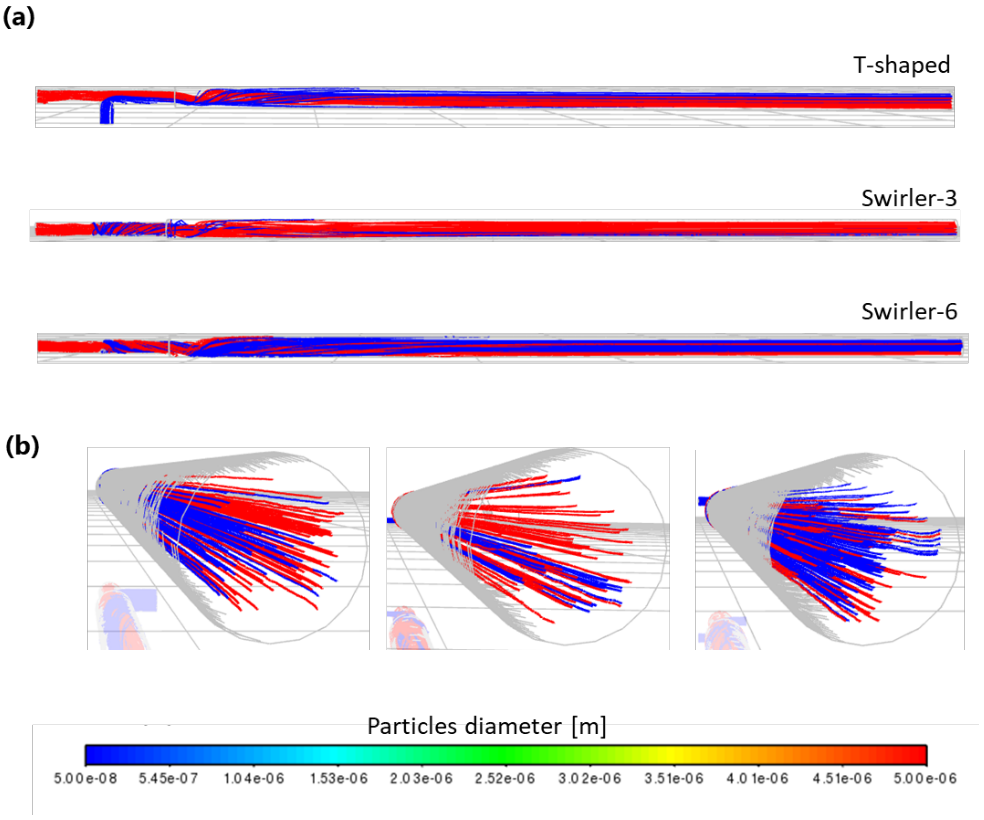

Figure C.S3. FeNi aerosol and HMDSO vapor trajectory along with the connector and reactor in different types of connectors (a) from the horizontal view, and (b) from the axial view at the outlet position.

Figure C.S3(a) describes the trajectory of FeNi aerosol and HMDSO vapor alongside the connector-assisted spray pyrolysis reactor. Swirler-6 exhibited the most uniform distribution between FeNi aerosol (red line) and HMDSO vapor (blue line). The T-shaped and Swirler-3 connectors, on the other hand, showed the movement of the HMDSO vapor on one side of the reactor, which is also significant from the trajectory of the particles near the outlet of the reactor (**Figure C.S3(b)**). A sudden temperature raise that can result in homogeneous nucleation[3] is shown in **Figure C.S4**.

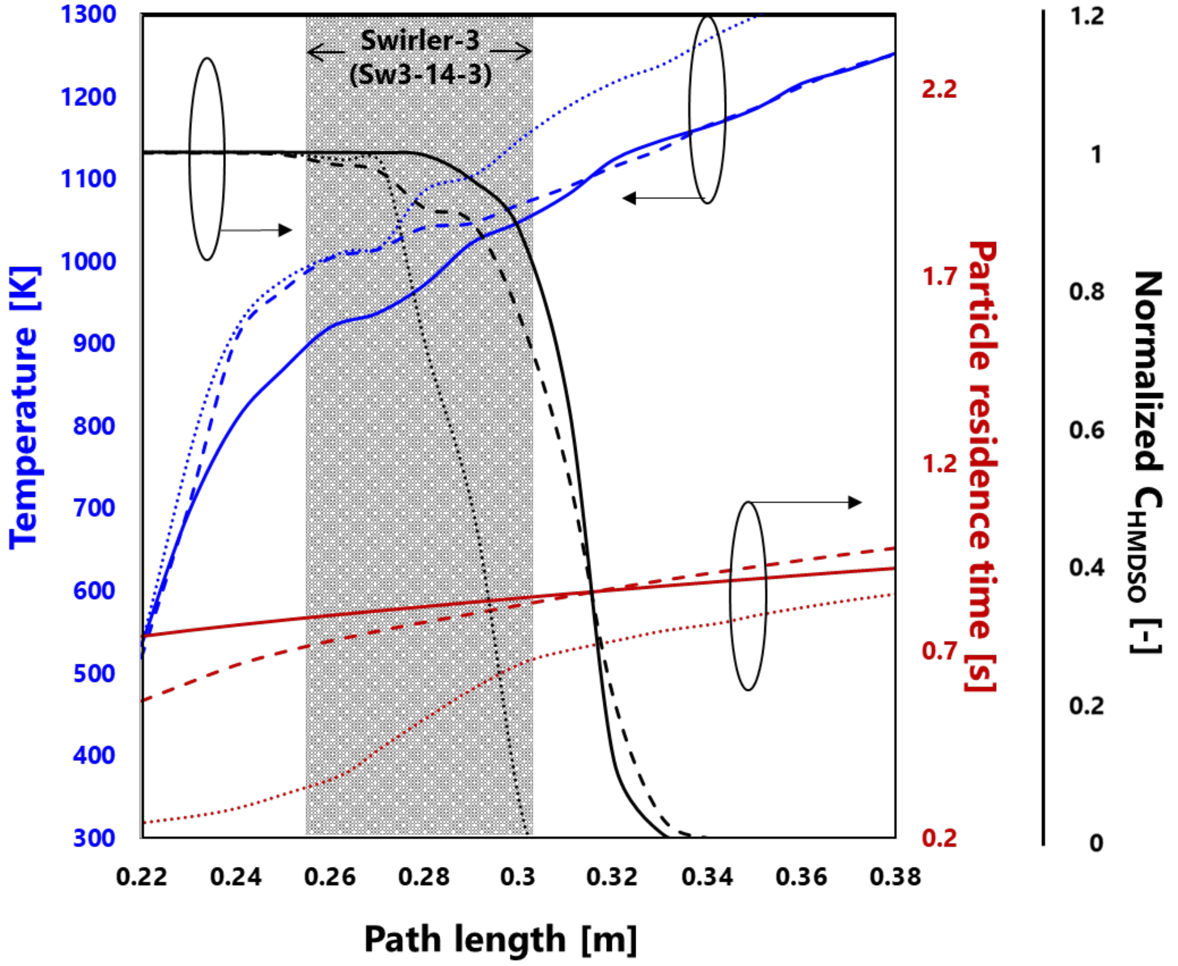

Figure C.S4. The plot of HMDSO concentration (black), residence time (red), and the temperature at the center (blue) as a function of length: T-shaped (dashed-line), Swirler-3 (dotted-line), Swirler-6 (solid-line).

C.3 FeNi@SiO_2 particles size and shell thickness distribution

The FeNi@SiO_2 particle's size and shell thickness distribution were determined by measuring approximately 400 particles from the TEM images using ruler software. An increase in the additional gas flow rates (Q_a) results in a decrease in the average particle diameter, as well as the average shell thickness (**Figure C.S5**). This is because of the low concentration of the HMDSO in the total volume of the gas flow.

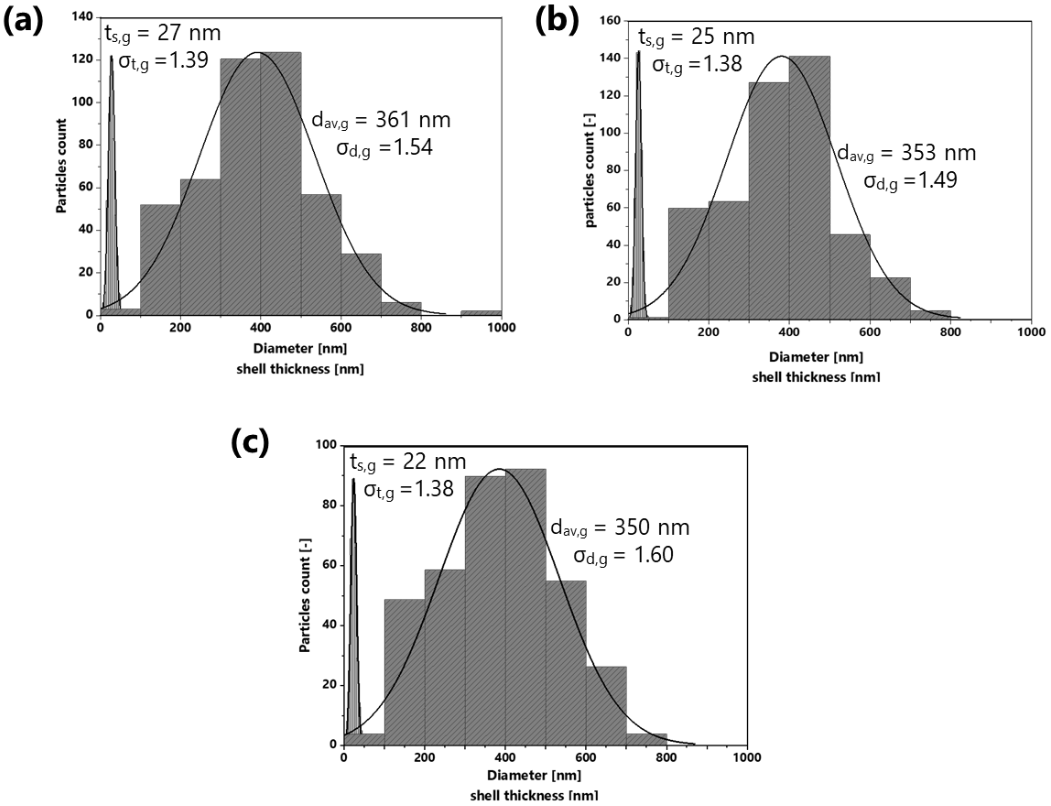

Figure C.S5. Effect of the additional gas flow rates on the particle size distribution of the FeNi@SiO_2: a) 3 L/min, b) 5 L/min, c) 7 L/min. $t_{s,g}$ is the geometric mean of the shell thickness, $\sigma_{t,g}$ is the geometric standard deviation of the shell thickness, $d_{av,g}$ is the geometric mean of the FeNi@SiO_2 particles, and $\sigma_{d,g}$ is the geometric standard deviation of the FeNi@SiO_2 particles.

C.4 Determining the HMDSO vapor inlet location and the additional gas flow rate

The position of the introduction of HMDSO affected to the synthesizing process. Therefore, we investigated two positions in Swirler-6, those with a/b ratios of 3 and 1, as shown in **Figure C.S6(a)**. According to the simulation results, the position with a/b ratio of 3 resulted in a strongly swirling flow inside the reactor. The position with a/b ratio of 1, on the other hand, resulted in an axial flow due to decreasing of the swirling intensity inside the reactor. As a result, the a/b ratio of 3 produced agglomerated particles (red arrow), whereas the a/b ratio of 1 produced individual particles (**Figure C.S6(b)**). Hence, the position of the connector is determined by the a/b ratio of 1 for the investigation of all connectors.

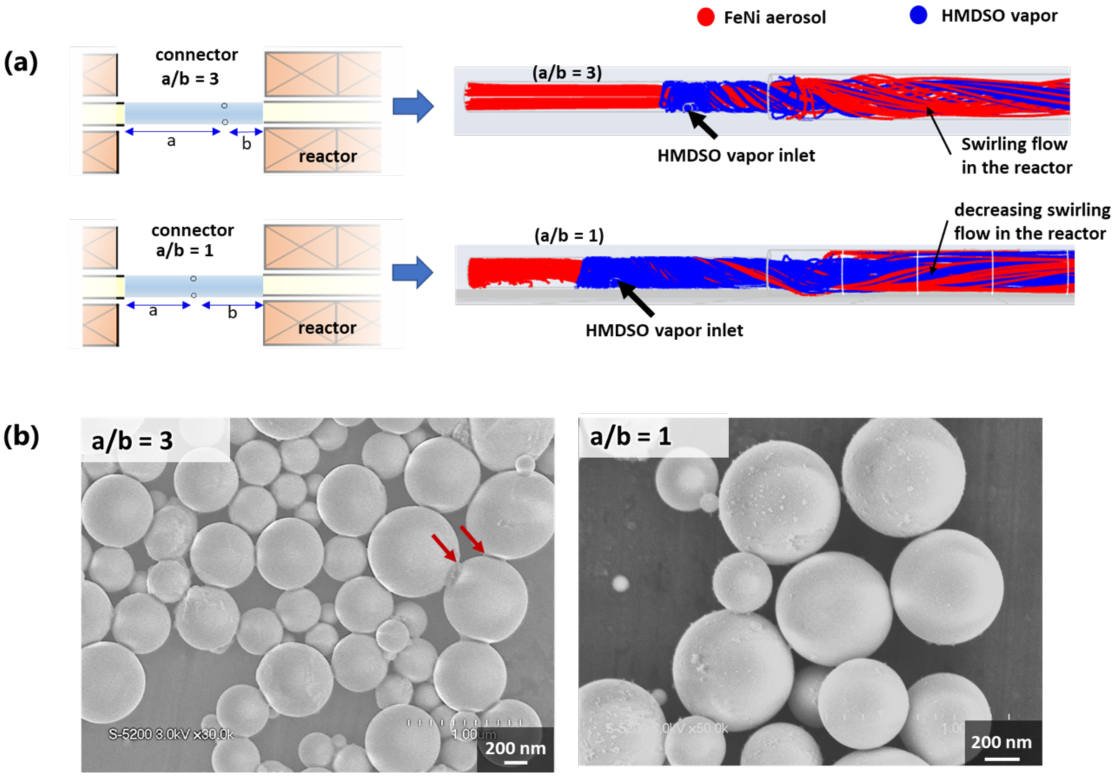

Figure C.S6. Effect of the connector position on the (a) FeNi aerosol and HMDSO vapor flows from the simulation results, (b) morphology of the $FeNi@SiO_2$ particles from SEM analysis.

In terms of additional gas flow rates (Q_a), we considered Q_a of 1, 3, 5, and 7 L/min. However, using Swirler-6 with a Q_a of 1 L/min resulted in inhomogeneous coating, as shown in **Figure C.S7**. It could be caused by insufficient turbulent mixing of the FeNi aerosol and HMDSO vapor flows. Therefore, the Q_a effect was carried out at 3, 5, and 7 L/min.

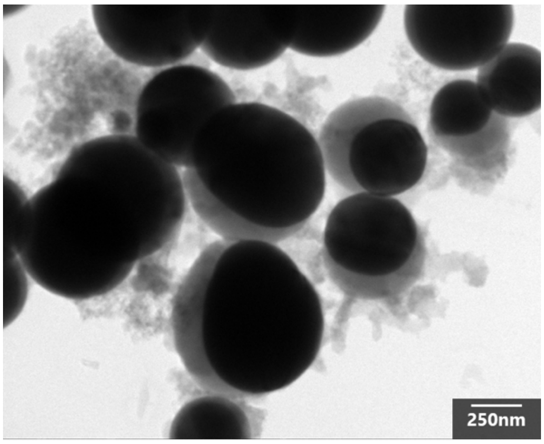

Figure C.S7. The TEM image of the synthesized particles by applying Q_a of 1 L/min.

C.5 Coating ratio calculation based on TEM image

The coating ratio (CR) of the synthesized FeNi@SiO_2 is determined by the TEM images of each sample. The CR is calculated by counting the number of coated particles divided by the total number of particles using a minimum of 150 particles from duple experiments. The coated particles are counted from fully coated particles, whereas the uncoated particles are counted from uncoated and partially coated particles, as depicted in **Figure S8**.

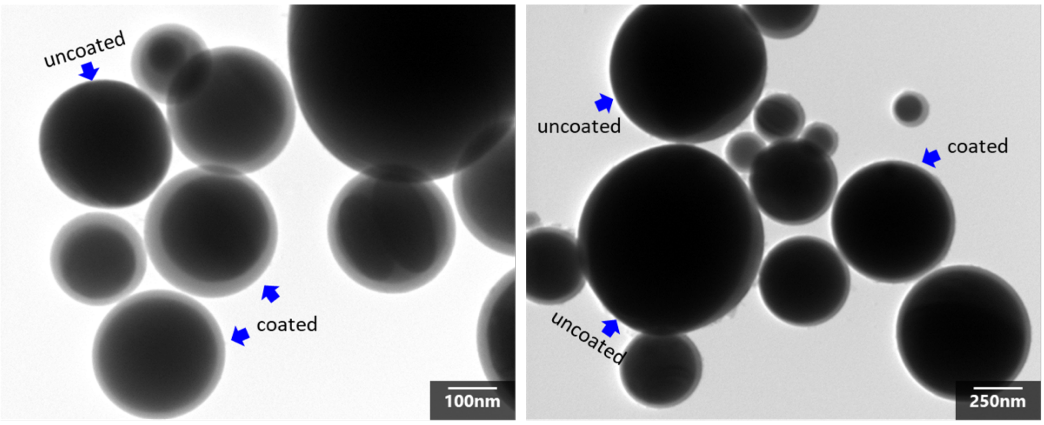

Figure C.S8. TEM image of the coated and uncoated FeNi@SiO_2 particles from the sample of Sw6-14-3.

Figure C.S9(a-c) showed the particles count to obtain the CR value from different samples. The average CR value of Sw6-14-3, Sw6-14-5, and Sw6-14-7 were 94.8%, 95.9%, and 93.1% with the standard deviation values of 0.3%, 0.9%, and 1%, respectively.

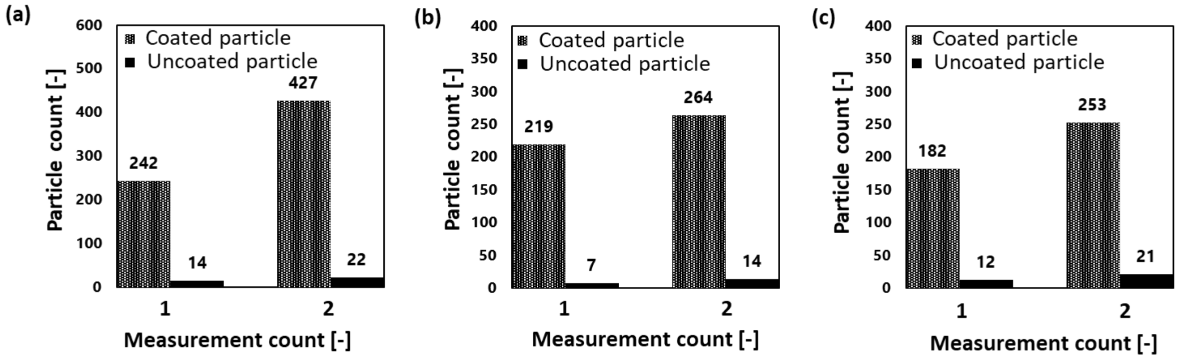

Figure C.S9. The counting of coated and uncoated FeNi@SiO_2 particles from the samples of (a) Sw6-14-3, (b) Sw6-14-5, (c) Sw6-14-7.

C.5 Intermediate product of FeNi aerosol after preheater

To understand the intermediate product state, a paper filter is mounted at the preheater outlet as shown in **Figure C.S10(a)**. During flowing the FeNi aerosol into the preheater, Figure C.**S10(b)** depicted fluid flow movement from a naked-eye view. Before passing through the paper filter, a clear fluid flow is captured, whereas after passing through the paper filter, a cloudy fluid flow is seen. This indicated that the droplet was still maintained, reach its saturation point, and had not yet altered to the precipitated solid. It is supported by the FeNi precursor attached to the paper filter, as shown in **Figure C.S10 (c)**. The FeNi precursor trace was visible even at the tube's outer cross-sectional circumference, which could be attributed to the radial capillary.[4]

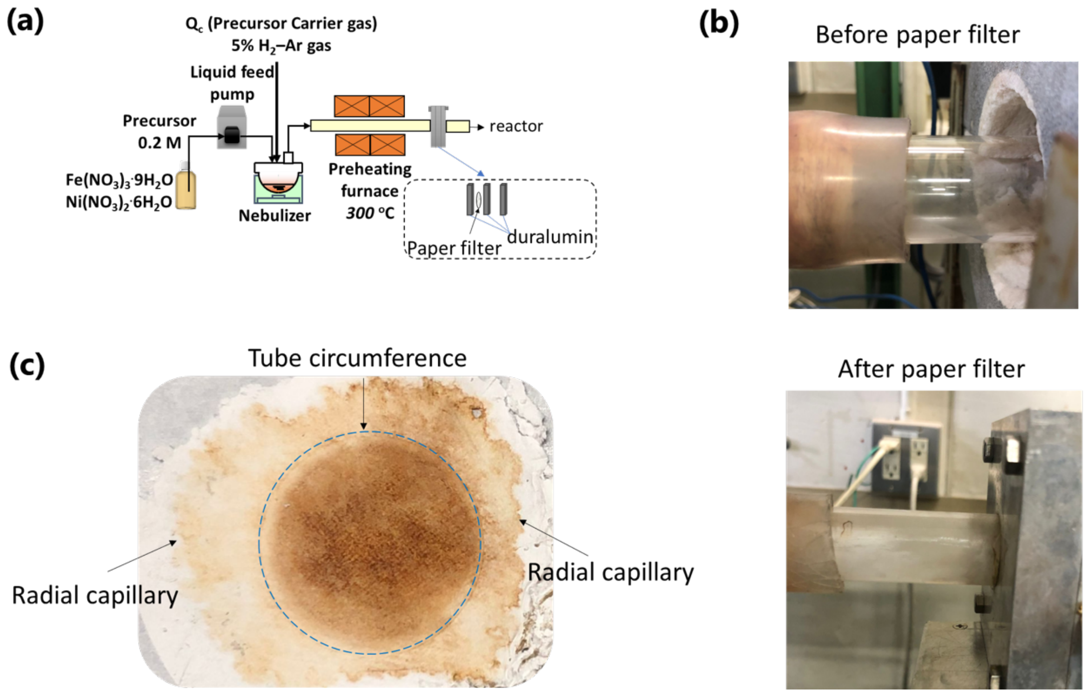

Figure C.S10. (a) Experimental set up to observe the intermediate product, (b) the fluid flow inside the tube before and after the paper filter, and (c) the paper filter condition after flowing FeNi aerosol.

BIBLIOGRAPHY

[1] A. Rehman, M.M. Alam, I. Ozturk, R. Alvarado, M. Murshed, C. Işık, H. Ma, Globalization and renewable energy use: how are they contributing to upsurge the CO_2 emissions? A global perspective, Environmental Science and Pollution Research. 30 (2023) 9699–9712.

[2] K. Nansai, S. Tohno, S. Chatani, K. Kanemoto, S. Kagawa, Y. Kondo, W. Takayanagi, M. Lenzen, Consumption in the G20 nations causes particulate air pollution resulting in two million premature deaths annually, Nat Commun. 12 (2021).

[3] M. Bartoli, A. Reatti, M.K. Kazimierczuk, High-Frequency Models of Ferrite Core Inductors.

[4] J. Imaoka, K. Okamoto, M. Shoyama, Y. Ishikura, M. Noah, M. Yamamoto, Modeling, magnetic design, simulation methods, and experimental evaluation of various powder cores used in power converters considering their dc superimposition characteristics, IEEE Trans Power Electron. 34 (2019) 9033–9051.

[5] A. Nosenko, O. Rudenko, T. Mika, I. Yevlash, O. Semyrga, V. Nosenko, DC bias immune nanocrystalline magnetic cores made of $Fe_{73}Nb_3Cu_1B_7Si_{16}$ ribbon with induced transverse magnetic anisotropy, Nanoscale Res Lett. 11 (2016) 1–7.

[6] F. Cardarelli, Materials Handbook, 3rd Edition, Electrochem Technologies & Materials Inc., Montréal (QC) H1V 2V9, Canada, 2008.

[7] L.E. Murr, Innovations in Magnetic Materials, in: Handbook of Materials Structures, Properties, Processing and Performance, Springer International Publishing, 2015:1011–1048.

[8] www.mag-inc.com, MPP Cores.

[9] V.C. Valchev, Advantages and Applications of Nanocrystalline Magnetic Materials, 51 (2016).

[10] C.W.T. McLyman, Transformer and inductor design handbook., CRC press., 2004.

[11] A. Goldman, Handbook of Modern Ferromagnetic Materials, Springer US, 1999.

[12] T. Ueno, H. Tsuruta, tatsuya Saito, A. Watanabe, T. Ishimine, K. Yamada, Practical and Potential Applications of Soft Magnetic Powder Cores with Superior Magnetic Properties, SEI TECHNICAL REVIEW. (2016).

[13] P. Duwez, S.C.H. Lin, Amorphous ferromagnetic phase in iron-carbon-phosphorus alloys, J Appl Phys. 38 (1967) 4096–4097.

[14] Y. Yoshizawa, S. Oguma, K. Yamauchi, New Fe-based soft magnetic alloys composed of ultrafine grain structure, J Appl Phys. 64 (1988) 6044–6046.

[15] M.A. Willard, D.E. Laughlin, M.E. McHenry, D. Thoma, K. Sickafus, J.O. Cross, V.G. Harris, Structure and magnetic properties of $(Fe_{0.5}Co_{0.5})_{88}Zr_7B_4Cu_1$ nanocrystalline alloys, J Appl Phys. 84 (1998) 6773–6777.

[16] A. Leary, V. Keylin, A. Devaraj, V. Degeorge, P. Ohodnicki, M.E. McHenry, Stress induced anisotropy in Co-rich magnetic nanocomposites for inductive applications, J Mater Res. 31 (2016) 3089–3107.

[17] J.M. Silveyra, E. Ferrara, D.L. Huber, T.C. Monson, Soft magnetic materials for a sustainable and electrified world, Science (1979). 362 (2018). https://doi.org/10.1126/science.aao0195.

[18] I. Otsuka, T. Kadomura, K. Ishiyama, M. Yagi, Magnetic properties of Fe-based amorphous powder cores with high magnetic flux density, IEEE Trans Magn. 45 (2009) 4294–4297.

[19] H. Shokrollahi, K. Janghorban, The effect of compaction parameters and particle size on magnetic properties of iron-based alloys used in soft magnetic composites, Mater Sci Eng B Solid State Mater Adv Technol. 134 (2006) 41–43.

[20] H.J. Woo, J.H. Ahn, C.P. Kim, D.H. Choi, S. Kim, B.W. Lee, Effect of the particle size classification of FeSiCrB amorphous soft magnetic composites to improve magnetic properties of power inductors, J Non Cryst Solids. 577 (2022).

[21] G.H. Kim, T.H. Noh, G.B. Choi, K.Y. Kim, Magnetic properties of FeCuNbSiB nanocrystalline alloy powder cores using ball-milled powder, in: J Appl Phys, 2003: pp. 7211–7213.

[22] N. Yabu, K. Sugimura, M. Sonehara, T. Sato, Fabrication and evaluation of composite magnetic core using iron-based amorphous alloy powder with different particle size distributions, IEEE Trans Magn. 54 (2018).

[23] B. Li, Z.G. Zheng, H.Y. Yu, D.C. Zeng, Improved permeability of Fe based amorphous magnetic powder cores by adding Permalloy, J Magn Magn Mater. 438 (2017) 138–143.

[24] C. Xia, Y. Peng, X. Yi, Z. Yao, Y. Zhu, G. Hu, Improved magnetic properties of FeSiCr amorphous soft magnetic composites by adding carbonyl iron powder, J Non Cryst Solids. 559 (2021).

[25] J. Liu, Y. Dong, P. Wang, Z. Zhu, J. Pang, X. Li, J. Zhang, Improved high-frequency magnetic properties of FeSiBCCr amorphous soft magnetic composites by adding carbonyl iron powders, J Non Cryst Solids. 605 (2023) 122166.

[26] H.J. Kim, S.K. Nam, K.S. Kim, S.C. Yoon, K.Y. Sohn, M.R. Kim, Y.S. Song, W.W. Park, Magnetic properties of amorphous Fe-Si-B powder cores mixed with pure iron powder, Jpn J Appl Phys. 51 (2012).

[27] R. Zhao, J. Huang, Y. Yang, L. Jiao, Y. Dong, X. Liu, Z. Liu, S. Wu, X. Li, A. He, J. Li, The influence of FeNi nanoparticles on the microstructures and soft magnetic properties of FeSi soft magnetic composites, Advanced Powder Technology. 33 (2022).

[28] J. Lai, L. Xiao, Z. Xiong, L. Fang, W. Zhu, F. Kuang, Z. Gao, Enhanced soft magnetic properties and high-frequency stability of FeNiMo powder cores by coating SiO_2 insulation layer, RSC Adv. 13 (2023) 15892–15900.

[29] B. Zhou, Y. Dong, L. Liu, L. Chang, F. Bi, X. Wang, Enhanced soft magnetic properties of the Fe-based amorphous powder cores with novel TiO_2 insulation coating layer, J Magn Magn Mater. 474 (2019) 1–8.

[30] H. Sun, C. Wang, J. Wang, M. Yu, Z. Guo, Fe-based amorphous powder cores with low core loss and high permeability fabricated using the core-shell structured magnetic flaky powders, J Magn Magn Mater. 502 (2020).

[31] S. Wu, Y. Dong, X. Li, M. Gong, R. Zhao, W. Gao, H. Wu, A. He, J. Li, X. Wang, X. Liu, Microstructure and magnetic properties of FeSiCr soft magnetic powder cores with a MgO insulating layer prepared by the sol-gel method, Ceram Int. 48 (2022) 22278–22286.

[32] H.J. Liu, H.L. Su, W.B. Geng, Z.G. Sun, T.T. Song, X.C. Tong, Z.Q. Zou, Y.C. Wu, Y.W. Du, Effect of Particle Size Distribution on the Magnetic Properties of Fe-Si-Al Powder Core, J Supercond Nov Magn. 29 (2016) 463–468.

[33] K. Gheisari, S. Shahriari, S. Javadpour, Structural evolution and magnetic properties of nanocrystalline 50 Permalloy powders prepared by mechanical alloying, J Alloys Compd. 574 (2013) 71–82.

[34] V.A.P. Rodríguez, C. Rojas-Ayala, J.M. Medina, P.P. Cabrera, J. Quispe-Marcatoma, C. V. Landauro, J.R. Tapia, E.M. Baggio-Saitovitch, E.C. Passamani, $Fe_{50}Ni_{50}$ synthesized by high energy ball milling: A systematic study using X-ray diffraction, EXAFS and Mössbauer methods, Mater Charact. 149 (2019) 249–254.

[35] A. Djekoun, A. Otmani, B. Bouzabata, L. Bechiri, N. Randrianantoandro, J.M. Greneche, Synthesis and characterization of high-energy ball milled nanostructured $Fe_{50}Ni_{50}$, Catal Today. 113 (2006) 235–239.

[36] J. Liu, Y. Feng, T. Qiu, Synthesis, characterization, and microwave absorption properties of Fe40 wt%Ni alloy prepared by mechanical alloying and annealing, J Magn Magn Mater. 323 (2011) 3071–3076.

[37] P.H. Zhou, L.J. Deng, J.L. Xie, D.F. Liang, L. Chen, X.Q. Zhao, Nanocrystalline structure and particle size effect on microwave permeability of FeNi powders prepared by mechanical alloying, J Magn Magn Mater. 292 (2005) 325–331.

[38] Z. Xu, C. Jin, A. Xia, J. Zhang, G. Zhu, Structural and magnetic properties of nanocrystalline nickel-rich Fe-Ni alloy powders prepared via hydrazine reduction, J Magn Magn Mater. 336 (2013) 14–19.

[39] S.F. Moustafa, W.M. Daoush, Synthesis of nano-sized Fe-Ni powder by chemical process for magnetic applications, J Mater Process Technol. 181 (2007) 59–63.

[40] V. Solanki, O.I. Lebedev, M.M. Seikh, N.K. Mahato, B. Raveau, A.K. Kundu, Synthesis and characterization of Co–Ni and Fe–Ni alloy nanoparticles, J Magn Magn Mater. 420 (2016) 39–44.

[41] L. Liu, J. Guan, W. Shi, Z. Sun, J. Zhao, Facile synthesis and growth mechanism of flowerlike Ni-Fe alloy nanostructures, Journal of Physical Chemistry C. 114 (2010) 13565–13570.

[42] Q. Liao, R. Tannenbaum, Z.L. Wang, Synthesis of $FeNi_3$ alloyed nanoparticles by hydrothermal reduction, Journal of Physical Chemistry B. 110 (2006) 14262–14265. https://doi.org/10.1021/jp0625154.

[43] J. Jia, J.C. Yu, Y.X.J. Wang, K.M. Chan, Magnetic nanochains of FeNi3 prepared by a template-free microwave-hydrothermal method, ACS Appl Mater Interfaces. 2 (2010) 2579–2584.

[44] G. Viau, F. Fibvet-Vincent, F. Fibvet, Monodisperse iron-based particles: precipitation in liquid polyols, 1996.

[45] Y. Feng, T. Qiu, Preparation, characterization and microwave absorbing properties of FeNi alloy prepared by gas atomization method, J Alloys Compd. 513 (2012) 455–459.

[46] T. Zubar, A. Trukhanov, D. Vinnik, K. Astapovich, D. Tishkevich, E. Kaniukov, A. Kozlovskiy, M. Zdorovets, S. Trukhanov, Features of the Growth Processes and Magnetic Domain Structure of NiFe Nano-objects, Journal of Physical Chemistry C. 123 (2019) 26957–26964.

[47] C. Duhamel, Y. Champion, M. Tencé, M. Walls, Synthesis of controlled-chemistry ultrafine FexNi1-x ferromagnetic powders, J Alloys Compd. 393 (2005) 204–210.

[48] X.G. Li, A. Chiba, S. Takahashi, Preparation and magnetic properties of ultrafine particles of Fe-Ni alloys, J Magn Magn Mater. 170 (1997) 339–345.

[49] S. Eroglu, S.C. Zhang, G.L. Messing, Synthesis of nanocrystalline Ni-Fe alloy powders by spray pyrolysis, J Mater Res. 11 (1996) 2131–2134.

[50] S. Gürmen, S. Stopić, B. Friedrich, Synthesis of nanosized spherical cobalt powder by ultrasonic spray pyrolysis, Mater Res Bull. 41 (2006) 1882–1890.

[51] Y.J. Suh, H.D. Jang, H. Chang, W.B. Kim, H.C. Kim, Size-controlled synthesis of Fe-Ni alloy nanoparticles by hydrogen reduction of metal chlorides, Powder Technol. 161 (2006) 196–201.

[52] S. Gurmen, B. Ebin, S. Stopić, B. Friedrich, Nanocrystalline spherical iron-nickel (Fe-Ni) alloy particles prepared by ultrasonic spray pyrolysis and hydrogen reduction (USP-HR), J Alloys Compd. 480 (2009) 529–533.

[53] M. Ammar, F. Mazaleyrat, J.P. Bonnet, P. Audebert, A. Brosseau, G. Wang, Y. Champion, Synthesis and characterization of core-shell structure silica-coated $Fe_{29.5}Ni_{70.5}$ nanoparticles, Nanotechnology. 18 (2007).

[54] Z. Wang, H. Jiang, Core-shell FeNi@SiO_2 composite with enhanced microwave absorption performance, J Alloys Compd. 923 (2022).

[55] S. Ghiami, M.A. Nasseri, A. Allahresani, M. Kazemnejadi, L. King, $FeNi_3@SiO_2$nanoparticles: an efficient and selectiveheterogeneous catalyst for the epoxidation of olefinsand the oxidation of sulfides in the presence ofmeta-chloroperoxybenzoic acid at room temperature, 126 (2018) 383–398.

[56] S.J. Yan, L. Zhen, C.Y. Xu, J.T. Jiang, W.Z. Shao, Microwave absorption properties of $FeNi_3$ submicrometre spheres and $SiO_2@FeNi_3$ core-shell structures, J Phys D Appl Phys. 43 (2010).

[57] C. Zhang, X. Liu, X. Kan, S. Feng, Y. Zhu, Y. Yang, Z. Zhang, Soft magnetic properties of nano-SiO_2 coated FeNi alloy powder at high frequencies, Journal of Materials Science: Materials in Electronics. 33 (2022) 25383–25391.

[58] H.Y. Jiang, W. Zhong, X.L. Wu, N.J. Tang, W. Liu, Y.W. Du, Direct and alternating current magnetic properties of FeNi particles coated with SiO_2, J Alloys Compd. 384 (2004) 264–267.

[59] N.J. Tang, W. Zhong, H.Y. Jiang, Z.D. Han, W.Q. Zou, Y.W. Du, Complex permeability of $FeNi_3/SiO_2$ core-shell nanoparticles, Solid State Commun. 132 (2004) 71–74.

[60] S. Jain, G.P. Fotou, T.T. Kodas, A theoretical study on gas-phase coating of aerosol particles, J Colloid Interface Sci. 185 (1997) 26–38.

[61] and Y.Guo. Powell, Quint H., George P. Fotou, Toivo T. Kodas, Bruce M. Anderson, Gas-phase coating of TiO_2 with SiO_2 in a continuous flow hot-wall aerosol reactor, Materials Research. 12 (1997) 552-559.

[62] A.M. Boies, J.T. Roberts, S.L. Girshick, B. Zhang, T. Nakamura, A. Mochizuki, SiO_2 coating of silver nanoparticles by photoinduced chemical vapor deposition, Nanotechnology. 20 (2009).

[63] M. Dasgupta, P. Fortugno, H. Wiggers, Plasma-assisted gas-phase synthesis and in-line coating of silicon nanoparticles, Plasma Processes and Polymers. 17 (2020).

[64] P. Post, N. Jidenko, A.P. Weber, J.P. Borra, Post-plasma SiO_x coatings of metal and metal oxide nanoparticles for enhanced thermal stability and tunable photoactivity applications, Nanomaterials. 6 (2016).

[65] A. Teleki, M. Suter, P.R. Kidambi, B.J. Nelson, S.E. Pratsinis, Hermetically Coated Superparamagnetic Fe_2O_3 Particles with SiO_2 Nano lms, Technology (Singap World Sci). (2009) 2094–2100.

[66] A. Teleki, B. Buesser, M.C. Heine, F. Krumeich, M.K. Akhtar, S.E. Pratsinls, Role of gas - Aerosol mixing during in situ coating of flame-made titania particles, Ind Eng Chem Res. 48 (2009) 85–92.

[67] A. V. Nomoev, S.P. Bardakhanov, M. Schreiber, D.G. Bazarova, N.A. Romanov, B.B. Baldanov, B.R. Radnaev, V. V. Syzrantsev, Structure and mechanism of the formation of core-shell nanoparticles obtained through a one-step gas-phase synthesis by electron beam evaporation, Beilstein Journal of Nanotechnology. 6 (2015) 874–880.

[68] S. Basak, V. Tiwari, J. Fan, S. Achilefu, V. Sethi, P. Biswas, Single step aerosol synthesis of nanocomposites by aerosol routes: γ-Fe_2O_3/SiO_2 and their functionalization, J Mater Res. 26 (2011) 1225–1233.

[69] B. Buesser, S.E. Pratsinis, Design of aerosol particle coating: Thickness, texture and efficiency, Chem Eng Sci. 65 (2010) 5471–5481.

[70] A. Teleki, B. Buesser, M.C. Heine, F. Krumeich, M.K. Akhtar, S.E. Pratsinls, Role of gas - Aerosol mixing during in situ coating of flame-made titania particles, Ind Eng Chem Res. 48 (2009) 85–92.

[71] G. Kastrinaki, S. Lorentzou, G. Karagiannakis, M. Rattenbury, J. Woodhead, A.G. Konstandopoulos, Parametric synthesis study of iron based nanoparticles via aerosol spray pyrolysis route, J Aerosol Sci. 115 (2018) 96–107.

[72] B. Buesser, S.E. Pratsinis, Design of aerosol coating reactors: Precursor injection, Ind Eng Chem Res. 50 (2011) 13831–13839.

[73] Anonim, Ansys Fluent Theory Guide, ANSYS Inc., USA. 15317 (2016) 724–746.

[74] K. Akedo, T. Ishizaki, K. Yatsugi, Structural and magnetic properties of size-controlled Fe–Ni nanoparticles synthesized by diffusing Fe atoms into preformed Ni nanoparticles, Journal of Nanoparticle Research. 23 (2021).

[75] D. Li, H. Liu, L. Feng, A Review on Advanced FeNi-Based Catalysts for Water Splitting Reaction, Energy and Fuels. 34 (2020) 13491–13522.

[76] K.L. McNerny, Y. Kim, D.E. Laughlin, M.E. McHenry, Chemical synthesis of monodisperse γ-Fe-Ni magnetic nanoparticles with tunable Curie temperatures for self-regulated hyperthermia, J Appl Phys. 107 (2010) 10–13.

[77] P. Wasilewski, Magnetization of small iron-nickel spheres, Physics of the Earth and Planetary Interiors. 26 (1981) 149–161.

[78] Q. Li, C.W. Kartikowati, S. Horie, T. Ogi, T. Iwaki, K. Okuyama, Correlation between particle size/domain structure and magnetic properties of highly crystalline Fe_3O_4 nanoparticles, Sci Rep. 7 (2017) 1–4.

[79] K.L.A. Cao, A.M. Rahmatika, Y. Kitamoto, M.T.T. Nguyen, T. Ogi, Controllable synthesis of spherical carbon particles transition from dense to hollow structure derived from Kraft lignin, J Colloid Interface Sci. 589 (2021) 252–263.

[80] T. Ogi, A.B.D. Nandiyanto, W.N. Wang, F. Iskandar, K. Okuyama, Direct synthesis of spherical YAG:Ce phosphor from precursor solution containing polymer and urea, Chemical Engineering Journal. 210 (2012) 461–466.

[81] K.L.A. Cao, Y. Kitamoto, F. Iskandar, T. Ogi, Sustainable porous hollow carbon spheres with high specific surface area derived from Kraft lignin, Advanced Powder Technology. (2021).

[82] M. Aliofkhazraei, Handbook of nanoparticles, 2015.

[83] T. Ogi, R. Zulhijah, T. Iwaki, K. Okuyama, Recent progress in nanoparticle dispersion using bead mill, KONA Powder and Particle Journal. 2017 (2017) 3–23.

[84] T. Ogi, A.B.D. Nandiyanto, K. Okuyama, Nanostructuring strategies in functional fine-particle synthesis towards resource and energy saving applications, Advanced Powder Technology. 25 (2014) 3–17.

[85] X.L. Dong, Z.D. Zhang, X.G. Zhao, Y.C. Chuang, S.R. Jin, W.M. Sun, The Preparation and Characterization of Ultrafine Fe-Ni particles, Journal of Material Research. 14 (1999) 389–406.

[86] T. Ogi, D. Hidayat, F. Iskandar, A. Purwanto, K. Okuyama, Direct synthesis of highly crystalline transparent conducting oxide nanoparticles by low pressure spray pyrolysis, Advanced Powder Technology. 20 (2009) 203–209.

[87] S. Nakakura, A.F. Arif, F.G. Rinaldi, T. Hirano, E. Tanabe, R. Balgis, T. Ogi, Direct synthesis of highly crystalline single-phase hexagonal tungsten oxide nanorods by spray pyrolysis, Advanced Powder Technology. 30 (2019) 6–12.

[88] T. Ogi, H. Fukazawa, A.M. Rahmatika, T. Hirano, K.L.A. Cao, F. Iskandar, Improving the Crystallinity and Purity of Monodisperse Ag Fine Particles by Heating Colloidal Sprays In-Flight, Ind Eng Chem Res. 59 (2020) 5745–5751.

[89] A.F. Arif, Y. Chikuchi, R. Balgis, T. Ogi, K. Okuyama, Synthesis of nitrogen-functionalized macroporous carbon particles: Via spray pyrolysis of melamine-resin, RSC Adv. 6 (2016) 83421–83428.

[90] L. Gradon, R. Balgis, T. Hirano, A.M. Rahmatika, T. Ogi, K. Okuyama, Advanced aerosol technologies towards structure and morphologically controlled next-generation catalytic materials, J Aerosol Sci. 149 (2020) 105608.

[91] I.W. Lenggoro, Y.C. Kang, T. Komiya, K. Okuyama, N. Tohge, Formation of submicron copper sulfide particles using spray pyrolysis method, Japanese Journal of Applied Physics, Part 2: Letters. 37 (1998) 288–290.
[92] B. Xia, I.W. Lenggoro, K. Okuyama, Preparation of Nickel Powders by Spray Pyrolysis of Nickel Formate, Journal of the American Ceramic Society. 84 (2001) 1425–1432.
[93] J.H. Kim, V.I. Babushok, T.A. Germer, G.W. Mulholland, S.H. Ehrman, Cosolvent-assisted spray pyrolysis for the generation of metal particles, J Mater Res. 18 (2003) 1614–1622.
[94] K. Zhong, G. Peabody, H. Glicksman, S. Ehrman, Particle generation by cosolvent spray pyrolysis: Effects of ethanol and ethylene glycol, J Mater Res. 27 (2012) 2540–2550.
[95] K. Zhong, G. Peabody, E. Blankenhorn, H. Glicksman, S. Ehrman, Spray pyrolysis of phase pure AgCu particles using organic cosolvents, J Mater Res. 28 (2013) 2753–2761.
[96] J.S.O.E. Robert E. Dinnebier, Andreas Leineweber, Rietveld Refinement, De Gruyter, Berlin, 2019.
[97] M.G. Rosmaninho, F.C.C. Moura, L.R. Souza, R.K. Nogueira, G.M. Gomes, J.S. Nascimento, M.C. Pereira, J.D. Fabris, J.D. Ardisson, M.S. Nazzarro, K. Sapag, M.H. Araújo, R.M. Lago, Investigation of iron oxide reduction by ethanol as a potential route to produce hydrogen, Appl Catal B. 115–116 (2012) 45–52.
[98] J.W. Evangelista, C.T. Avedisian, W. Tsang, Thermal and catalytic decomposition of aqueous ethylene glycol mixtures by film boiling, Int J Heat Mass Transf. 55 (2012) 6425–6434.
[99] Z.L. Wang, J.M. Yan, H.L. Wang, Y. Ping, Q. Jiang, Pd/C synthesized with citric acid: An efficient catalyst for hydrogen generation from formic acid/sodium formate, Sci Rep. 2 (2012) 1–6.
[100] W.N. Wang, Y. Itoh, I.W. Lenggoro, K. Okuyama, Nickel and nickel oxide nanoparticles prepared from nickel nitrate hexahydrate by a low pressure spray pyrolysis, Mater Sci Eng B Solid State Mater Adv Technol. 111 (2004) 69–76.
[101] J.N. Wang, L. Zhang, F. Yu, Z.M. Sheng, Synthesis of carbon encapsulated magnetic nanoparticles with giant coercivity by a spray pyrolysis approach, Journal of Physical Chemistry B. 111 (2007) 2119–2124.
[102] Z. Jiang, P. Qin, T. Fang, Decomposition mechanism of formic acid on Cu (111) surface: A theoretical study, Appl Surf Sci. 396 (2017) 857–864.
[103] W.N. Wang, A. Purwanto, I.W. Lenggoro, K. Okuyama, H. Chang, H.D. Jang, Investigation on the correlations between droplet and particle size distribution in ultrasonic spray pyrolysis, Ind Eng Chem Res. 47 (2008) 1650–1659.
[104] H.C. Jang, S.H. Ju, Y.C. Kang, Characteristics of fine size Fe-Ni alloy powders directly prepared by spray pyrolysis, Metals and Materials International. 16 (2010) 643–647.
[105] R.A. Howald, The thermodynamics of tetrataenite and awaruite: A review of the Fe-Ni phase diagram, Metall Mater Trans A Phys Metall Mater Sci. 34 A (2003) 1759–1769.
[106] M.H. Aghaali, S. Firoozi, Synthesis of nanostructured fcc/hcp hollow Ni particles by ultrasonic spray pyrolysis and its dry reforming catalytic properties, Powder Technol. 356 (2019) 119–128.
[107] B. Xia, I.W. Lenggoro, K. Okuyama, Preparation of Nickel Powders by Spray Pyrolysis of Nickel Formate, Journal of the American Ceramic Society. 84 (2001) 1425–1432.
[108] A.M. Gadalla, H.F. Yu, Thermal Decomposition of Fe(III) Nitrate and Its Aerosol, J Mater Res. 5 (1990) 1233–1236.
[109] G. Schott, N. Davidson, Shock Waves in Chemical Kinetics: The Decomposition of N2O5 at High Temperatures, J Am Chem Soc. 80 (1958) 1841–1853.
[110] Y. Zhang, W. Wei, X. Yang, F. Wei, Reduction of Fe and Ni in Fe-Ni-O systems, Journal of Mining and Metallurgy, Section B: Metallurgy. 49 (2013) 13–20..

[111] S.H. Ehrman, S.K. Friedlander, M.R. Zachariah, Characteristics of SiO22/TiO2 nanocomposite particles formed in a premixed flat flame, J Aerosol Sci. 29 (1998) 687–706.

[112] K.Y. Jung, J.H. Lee, H.Y. Koo, Y.C. Kang, S. Bin Park, Preparation of solid nickel nanoparticles by large-scale spray pyrolysis of $Ni(NO_3)_2·6H_2O$ precursor: Effect of temperature and nickel acetate on the particle morphology, Mater Sci Eng B Solid State Mater Adv Technol. 137 (2007) 10–19.

[113] B. Bieniek, D. Pohl, L. Schultz, B. Rellinghaus, The effect of oxidation on the surface-near lattice relaxation in FeNi nanoparticles, Journal of Nanoparticle Research. 13 (2011) 5935–5946.

[114] H. Han, J. Park, S.Y. Nam, K.J. Kim, G.M. Choi, S.S.P. Parkin, H.M. Jang, J.T.S. Irvine, Lattice strain-enhanced exsolution of nanoparticles in thin films, Nat Commun. 10 (2019) 1–8.

[115] J. Zhang, M.R. Gao, J.L. Luo, In Situ Exsolved Metal Nanoparticles: A Smart Approach for Optimization of Catalysts, Chemistry of Materials. 32 (2020) 5424–5441.

[116] D. Spreitzer, J. Schenk, Reduction of Iron Oxides with Hydrogen—A Review, Steel Res Int. 90 (2019).

[117] D.H. Kim, G.Y. Choe, B.K. Lee, DCM Analysis and inductance design method of interleaved boost converters, IEEE Trans Power Electron. 28 (2013) 4700–4711.

[118] H.R. Kim, M.S. Jang, Y.G. Nam, Y.S. Kim, S.S. Yang, Y.J. Kim, J.W. Jeong, Enhanced permeability of Fe-based amorphous powder cores realized through selective incorporation of carbonyl iron powders at inter-particle voids, Metals (Basel). 11 (2021).

[119] M.S. Perdigão, J.P.F. Trovão, J.M. Alonso, E.S. Saraiva, Large-Signal Characterization of Power Inductors in EV Bidirectional DC-DC Converters Focused on Core Size Optimization, IEEE Transactions on Industrial Electronics. 62 (2015) 3042–3051.

[120] Y. Zhang, Q. Chi, L. Chang, Y. Dong, P. Cai, Y. Pan, M. Gong, J. Huang, J. Li, A. He, X. Wang, Novel Fe-based amorphous compound powder cores with enhanced DC bias performance by adding FeCo alloy powder, J Magn Magn Mater. 507 (2020).

[121] H. Shokrollahi, K. Janghorban, Soft magnetic composite materials (SMCs), J Mater Process Technol. 189 (2007) 1–12.

[122] E.L. Septiani, J. Kikkawa, K.L.A. Cao, T. Hirano, N. Okuda, H. Matsumoto, Y. Enokido, T. Ogi, Direct synthesis of submicron FeNi particles via spray pyrolysis using various reduction agents, Advanced Powder Technology. 32 (2021) 4263–4272.

[123] F. Iskandar, S.G. Kim, A.B.D. Nandiyanto, Y. Kaihatsu, T. Ogi, K. Okuyama, Direct synthesis of hBN/MWCNT composite particles using spray pyrolysis, J Alloys Compd. 471 (2009) 166–171.

[124] F. Lu, L. Wen, Y. Chen, H. Zhong, J. Xu, S. Zhang, Z. Yang, Carbon formation on the surface during the reduction of iron oxide particles by CO and CO/H_2 mixtures, Chem Eng Sci. 205 (2019) 238–247.

[125] J. Tu, J. Wang, S. Li, W.L. Song, M. Wang, H. Zhu, S. Jiao, High-efficiency transformation of amorphous carbon into graphite nanoflakes for stable aluminum-ion battery cathodes, Nanoscale. 11 (2019) 12537–12546.

[126] Z. V. Marinkovi, L. Manči, R. Mari, O. Miloševi, Preparation of nanostructured Zn-Cr-O spinel powders by ultrasonic spray pyrolysis, J Eur Ceram Soc. 21 (2001) 2051–2055.

[127] A. Kovacs, J. Fischbacher, H. Oezelt, T. Schrefl, A. Kaidatzis, R. Salikhov, M. Farle, G. Giannopoulos, D. Niarchos, Micromagnetic Simulations for Coercivity Improvement Through Nano-Structuring of Rare-Earth-Free L_{10}-FeNi Magnets, IEEE Trans Magn. 53 (2017) 1–6.

[128] S. Nakakura, A.F. Arif, K. Machida, K. Adachi, T. Ogi, Cationic Defect Engineering for Controlling the Infrared Absorption of Hexagonal Cesium Tungsten Bronze Nanoparticles, Inorg Chem. 58 (2019) 9101–9107.

[129] S. Goto, H. Kura, E. Watanabe, Y. Hayashi, H. Yanagihara, Y. Shimada, M. Mizuguchi, K. Takanashi, E. Kita, Synthesis of single-phase $L1_0$-FeNi magnet powder by nitrogen insertion and topotactic extraction, Sci Rep. 7 (2017).

[130] D. V. Kurmude, C.M. Kale, P.S. Aghav, D.R. Shengule, K.M. Jadhav, Superparamagnetic behavior of zinc-substituted nickel ferrite nanoparticles and its effect on mossbauer and magnetic parameters, J Supercond Nov Magn. 27 (2014) 1889–1897.

[131] B.Z. Cui, M. Marinescu, J.F. Liu, High magnetization Fe-Co and Fe-Ni submicron and nanosize particles by thermal decomposition and hydrogen reduction, J Appl Phys. 115 (2014) 313–316.

[132] C.M. Dos Santos, A.F.N. Martins, B.C. Costa, T.S. Ribeiro, T.P. Braga, J.M. Soares, J.M. Sasaki, Synthesis of FeNi Alloy Nanomaterials by Proteic Sol-Gel Method: Crystallographic, Morphological, and Magnetic Properties, J Nanomater. 2016 (2016).

[133] H. Tokoro, S. Fujii, S. Muto, S. Nasu, Fe-Co and Fe-Ni magnetic fine particles encapsulated by graphite carbon, J Appl Phys. 99 (2006) 1–4.

[134] A. Azizi, Worthwhile effects of salt-matrix reduction on shape, morphology and magnetic properties of FeNi nanoparticles, Mater Sci Eng B Solid State Mater Adv Technol. 176 (2011) 1517–1520.

[135] L.H. Bac, J.S. Kim, J.C. Kim, Synthesis of Fe-Ni invar alloy nanopowder by the electrical explosion of wire in the liquid, Research on Chemical Intermediates. 36 (2010) 795–800.

[136] S. Fujieda, W. Miyamura, K. Shinoda, S. Suzuki, B. Jeyadevan, Composition-controlled Fe-Ni alloy fine particles synthesized by reduction-annealing of polyol-derived Fe-Ni hydroxide, Mater Trans. 57 (2016) 1645–1651.

[137] S. Vitta, A. Khuntia, G. Ravikumar, D. Bahadur, Electrical and magnetic properties of nanocrystalline $Fe_{100-x}Ni_x$ alloys, J Magn Magn Mater. 320 (2008) 182–189.

[138] G. V. Kurlyandskaya, I. Madinabeitia, I. V. Beketov, A.I. Medvedev, A. Larrañaga, A.P. Safronov, S.M. Bhagat, Structure, magnetic and microwave properties of FeNi nanoparticles obtained by electric explosion of wire, J Alloys Compd. 615 (2015) S231–S235.

[139] N.S. Kanhe, A. Kumar, S.M. Yusuf, A.B. Nawale, S.S. Gaikwad, S.A. Raut, S. V. Bhoraskar, S.Y. Wu, A.K. Das, V.L. Mathe, Investigation of structural and magnetic properties of thermal plasma-synthesized $Fe_{1-x}Ni_x$ alloy nanoparticles, J Alloys Compd. 663 (2016) 30–40. https://doi.org/10.1016/j.jallcom.2015.11.190.

[140] A. Hilal, M.A. Raulet, C. Martin, F. Sixdenier, Power loss prediction and precise modeling of magnetic powder components in DC-DC power converter application, IEEE Trans Power Electron. 30 (2015) 2232–2238.

[141] D. Chen, K. Li, H. Yu, J. Zuo, X. Chen, B. Guo, G. Han, Z. Liu, Effects of secondary particle size distribution on the magnetic properties of carbonyl iron powder cores, J Magn Magn Mater. 497 (2019) 166062.

[142] E.L. Septiani, J. Kikkawa, K.L.A. Cao, T. Hirano, N. Okuda, H. Matsumoto, Y. Enokido, T. Ogi, DC bias characteristic enhancement of the powder core by using densified submicron sized FeNi particles through spray pyrolysis, J Mater Chem C Mater. 10 (2022) 8288–8295.

[143] H. Hojo, T. Kamijo, Y. Taniguchi, N. Akagi, H. Mitani, Dust core with low core-loss for high-frequency applications, R and D: Research and Development Kobe Steel Engineering Reports. 66 (2016) 68–71.

[144] L. Ernawati, T. Ogi, R. Balgis, K. Okuyama, M. Stucki, S.C. Hess, W.J. Stark, Hollow Silica as an Optically Transparent and Thermally Insulating Polymer Additive, Langmuir. 32 (2016) 338–345.

[145] A.B.D. Nandiyanto, Y. Akane, T. Ogi, K. Okuyama, Mesopore-free hollow silica particles with controllable diameter and shell thickness via additive-free synthesis, Langmuir. 28 (2012) 8616–8624.
[146] K.L.A. Cao, S. Taniguchi, T.T. Nguyen, A.F. Arif, F. Iskandar, T. Ogi, Precisely tailored synthesis of hexagonal hollow silica plate particles and their polymer nanocomposite films with low refractive index, J Colloid Interface Sci. 571 (2020) 378–386.
[147] G.A. Sotiriou, A.M. Hirt, P. Lozach, A. Teleki, F. Krumeich, S.E. Pratsinis, Hybrid , Silica-Coated , Janus-Like Plasmonic-Magnetic Nanoparticles, (2011) 1985–1992.
[148] P. Post, L. Wurlitzer, W. Maus-Friedrichs, A.P. Weber, Characterization and applications of nanoparticles modified in-flight with silica or silica-organic coatings, Nanomaterials. 8 (2018) 1–19.
[149] A. Teleki, M. Suter, P.R. Kidambi, B.J. Nelson, S.E. Pratsinis, Hermetically Coated Superparamagnetic Fe_2O_3 Particles with SiO_2 Nano lms, Technology (Singap World Sci). (2009) 2094–2100.
[150] S. Nakakura, T. Ogi, Hexagonal cesium tungsten bronze nanoparticles produced by solvent-free spray pyrolysis and their near infrared absorption properties, J Mater Chem C Mater. 9 (2021) 8037–8042.
[151] Y. Liang, R. Felix, H. Glicksman, S. Ehrman, Cu-Sn binary metal particle generation by spray pyrolysis, Aerosol Science and Technology. 51 (2017) 430–442.
[152] T. Ogi, Y. Kaihatsu, F. Iskandar, E. Tanabe, K. Okuyama, Synthesis of nanocrystalline GaN from Ga_2O_3 nanoparticles derived from salt-assisted spray pyrolysis, Advanced Powder Technology. 20 (2009) 29–34.
[153] K.L.A. Cao, F. Iskandar, E. Tanabe, T. Ogi, Recent Advances in the Fabrication and Functionalization of Nanostructured Carbon Spheres for Energy Storage Applications, KONA Powder and Particle Journal. (2022) 1–22.
[154] P.H. Le, Y. Kitamoto, K.L.A. Cao, T. Hirano, E. Tanabe, T. Ogi, Synthesis of macroporous three-way catalysts via template-assisted spray process for enhancing mass transfer in gas adsorption, Advanced Powder Technology. 33 (2022) 103581.
[155] H.L. Wang, C.Y. Hsu, K.C.W. Wu, Y.F. Lin, D.H. Tsai, Functional nanostructured materials: Aerosol, aerogel, and de novo synthesis to emerging energy and environmental applications, Advanced Powder Technology. 31 (2020) 104–120.
[156] Y. Okada, S. Matsumoto, R. Sawai, T. Kinoshita, Formation of non-aggregated nickel nanoparticles for catalysts by gas-phase reaction, Journal of Chemical Engineering of Japan. 50 (2017) 511–515.
[157] K. Okuyama, R. Ushio, Y. Kousaka, R.C. Flagan, J.H. Seinfeld, Particle generation in a chemical vapor deposition process with seed particles, AIChE Journal. 36 (1990) 409–419.
[158] G.A. Sotiriou, S. Gass, J. Cohen, G. Pyrgiotakis, S.E. Pratsinis, P. Demokritou, Safer formulation concept for flame-generated engineered nanomaterials, Sustainable Engineering Forum 2013 - Core Programming Area at the 2013 AIChE Annual Meeting: Global Challenges for Engineering a Sustainable Future. (2013) 262–263.
[159] P.M. Winkler, P.E. Wagner, Characterization techniques for heterogeneous nucleation from the gas phase, J Aerosol Sci. 159 (2022) 105875.
[160] M.A.A. Elmasry, A. Gaber, E.M.H. Khater, Thermal decomposition of Ni(II) and Fe(III) nitrates and their mixture, J Therm Anal Calorim. 52 (1998) 489–495.
[161] N. Karthigayan, P. Manimuthu, M. Priya, S. Sagadevan, Synthesis and characterization of $NiFe_2O_4$, $CoFe_2O_4$ and $CuFe_2O_4$ thin films for anode material in Li-ion batteries, 7 (2017) 1–5.
[162] D. Spreitzer, J. Schenk, Iron Ore Reduction by Hydrogen Using a Laboratory Scale Fluidized Bed Reactor: Kinetic Investigation—Experimental Setup and Method for

Determination, Metallurgical and Materials Transactions B: Process Metallurgy and Materials Processing Science. 50 (2019) 2471–2484.
[163] O. Kwon, S. Joo, S. Choi, S. Sengodan, G. Kim, Review on exsolution and its driving forces in perovskites, Journal of Physics : Energy. (2020).

List of Publications

1. **Eka Lutfi Septiani**, Jun Kikkawa Kiet Le Anh Cao, Tomoyuki Hirano, Nobuhiro Okuda, Hiroyuki Matsumoto, Yasushi Enokido, Takashi Ogi. Direct synthesis of submicron FeNi particles via spray pyrolysis using various reduction agents. Advanced Powder Technology, 32(11), 4263-4272, 2021.
2. **Eka Lutfi Septiani**, Jun Kikkawa Kiet Le Anh Cao, Tomoyuki Hirano, Nobuhiro Okuda, Hiroyuki Matsumoto, Yasushi Enokido, Takashi Ogi. DC bias characteristic enhancement of the powder core by using densified submicron sized FeNi particles through spray pyrolysis. Journal of Materials Chemistry C, 10(21), 8288-8295, 2022.
3. **Eka Lutfi Septiani**, Shunki Yamashita, Kiet Le Anh Cao, Tomoyuki Hirano, Nobuhiro Okuda, Hiroyuki Matsumoto, Yasushi Enokido, Takashi Ogi. One-Step Aerosol Synthesis of SiO_2-Coated FeNi Particles by Using Swirler Connector-Assisted Spray Pyrolysis. Industrial & Engineering Chemistry Research, 61(49), 17885-17893, 2022.

Presentation in International/National Conferences

1. **Eka Lutfi Septiani**, Kiet Le Anh Cao, Tomoyuki Hirano, Nobuhiro Okuda, Hiroyuki Matsumoto, Yasushi Enokido, Takashi Ogi. Spherical and submicron-sized FeNi particles with controllable density for performance enhancement of the powder core inductor, International Chemical Engineering Symposia 2022, Online, March 16 – 18, 2022 (Oral presentation).
2. **Eka Lutfi Septiani**, Kiet Le Anh Cao, Tomoyuki Hirano, Nobuhiro Okuda, Hiroyuki Matsumoto, Yasushi Enokido, Takashi Ogi. Aerosol synthesis of dense spherical FeNi particles and their magnetic characterization, 2022 年度春期研究発表会, Society powder Technology Japan, May 17 – 18, 2022 (Oral presentation).
3. **Eka Lutfi Septiani**, Kiet Le Anh Cao, Tomoyuki Hirano, Nobuhiro Okuda, Hiroyuki Matsumoto, Yasushi Enokido, Takashi Ogi. Investigation of densified spherical and submicron-sized FeNi particles on their magnetic characteristics, 19th Asian Pacific Confederation of Chemical Engineering (APCChE), Hybrid, August 9 - 12, 2022 (Oral presentation).